

Axion optical induction of antiferromagnetic order

Jian-Xiang Qiu,¹ Christian Tzschaschel,¹ Junyeong Ahn,² Anyuan Gao,¹ Houchen Li,¹ Xin-Yue Zhang,³ Barun Ghosh,⁴ Chaowei Hu,⁵ Yu-Xuan Wang,³ Yu-Fei Liu,^{1,2} Damien Bérubé,¹ Thao Dinh,^{2,1} Zhenhao Gong,^{6,7,8,9} Shang-Wei Lien,^{10,11,12} Sheng-Chin Ho,¹ Bahadur Singh,¹³ Kenji Watanabe,¹⁴ Takashi Taniguchi,¹⁵ David C. Bell,^{16,17} Hai-Zhou Lu,^{6,7,8,9} Arun Bansil,⁴ Hsin Lin,¹⁸ Tay-Rong Chang,^{10,11,12} Brian B. Zhou,³ Qiong Ma,^{3,19} Ashvin Vishwanath,² Ni Ni*,⁵ and Su-Yang Xu*¹

¹*Department of Chemistry and Chemical Biology, Harvard University, MA, USA*

²*Department of Physics, Harvard University, Cambridge, MA, USA*

³*Department of Physics, Boston College, Chestnut Hill, MA, USA*

⁴*Department of Physics, Northeastern University, Boston, MA, USA*

⁵*Department of Physics and Astronomy and California NanoSystems Institute, University of California, Los Angeles, Los Angeles, CA, USA*

⁶*Shenzhen Institute for Quantum Science and Engineering and Department of Physics, Southern University of Science and Technology (SUSTech), Shenzhen, China*

⁷*Quantum Science Center of Guangdong-Hong Kong-Macao Greater Bay Area (Guangdong), Shenzhen, China*

⁸*Shenzhen Key Laboratory of Quantum Science and Engineering, Shenzhen, China*

⁹*International Quantum Academy, Shenzhen, China*

¹⁰*Department of Physics, National Cheng Kung University, Tainan, Taiwan*

¹¹*Center for Quantum Frontiers of Research and Technology (QFort), Tainan, Taiwan*

¹²*Physics Division, National Center for Theoretical Sciences, Taipei, Taiwan*

¹³*Department of Condensed Matter Physics and Materials Science, Tata Institute of Fundamental Research, Colaba, Mumbai, India*

¹⁴*Research Center for Functional Materials, National Institute for Materials Science, 1-1 Namiki, Tsukuba, Japan*

¹⁵*International Center for Materials Nanoarchitectonics,*

National Institute for Materials Science, 1-1 Namiki, Tsukuba, Japan

¹⁶*Harvard John A. Paulson School of Engineering and Applied Sciences, Harvard University, Cambridge, MA, USA*

¹⁷*Center for Nanoscale Systems, Harvard University, Cambridge, MA, USA*

¹⁸*Institute of Physics, Academia Sinica, Taipei, Taiwan*

* Corresponding authors (emails): suyangxu@fas.harvard.edu and nini@physics.ucla.edu

¹⁹*Canadian Institute for Advanced Research, Toronto, Canada*

(Dated: March 10, 2023)

Using circularly-polarized light to control quantum matter is a highly intriguing topic in physics, chemistry and biology. Previous studies have demonstrated helicity-dependent optical control of spatial chirality and magnetization M . The former is central for asymmetric synthesis in chemistry and homochirality in bio-molecules, while the latter is of great interest for ferromagnetic spintronics. In this paper, we report the surprising observation of helicity-dependent optical control of fully-compensated antiferromagnetic (AFM) order in 2D even-layered MnBi_2Te_4 , a topological Axion insulator with neither chirality nor M . We further demonstrate helicity-dependent optical creation of AFM domain walls by double induction beams and the direct reversal of AFM domains by ultrafast pulses. The control and reversal of AFM domains and domain walls by light helicity have never been achieved in any fully-compensated AFM. To understand this optical control, we study a novel type of circular dichroism (CD) proportional to the AFM order, which only appears in reflection but is absent in transmission. We show that the optical control and CD both arise from the optical Axion electrodynamics, which can be visualized as a Berry curvature real space dipole. Our Axion induction provides the possibility to optically control a family of \mathcal{PT} -symmetric AFMs such as Cr_2O_3 , CrI_3 and possibly novel states in cuprates. In MnBi_2Te_4 , this further opens the door for optical writing of dissipationless circuit formed by topological edge states.

Main

There is tremendous interest in finding innovative ways to control and manipulate complex quantum materials [1]. Antiferromagnets (AFMs) have zero net M , so AFM domains are immune to perturbing magnetic field. This leads to the prospect of robust magnetic storage [2, 3]. However, this robustness also means that manipulating fully-compensated AFM order is extremely difficult [3, 4, 31, 38] (discussion in SI.V.2). As such, controlling AFM order has been recognized a key challenge toward the AFM spintronics [2, 3]. One known approach is to use the parallel E and B fields [7, 8, 23]. Compared to such electrical approach, optical control is non-contact, flexible, has good spatial resolution and further allows for ultrafast manipulation. It also enables fundamental understanding of the interaction of photons with charges, spins, lattice, and quantum geometry.

In this paper, we explore the novel possibility of controlling fully-compensated AFM order by circularly-polarized light, which has never been achieved. We got inspirations from (1) discoveries of helicity-dependent optical control of chiral materials and magnetization M [4, 10, 11] and (2)

previous experiments reporting novel circular dichroism (CD) proportional to the AFM order in Cr_2O_3 [5, 13] and the pseudo-gap state of cuprates [14]. We report helicity-dependent optical control of fully-compensated AFM order induced by the optical Axion electrodynamics in even-layered MnBi_2Te_4 .

MnBi_2Te_4 , the first intrinsic magnetic topological insulator recently synthesized in 2019, has attracted great interest as it bridges three primary fields in quantum condensed matter: topology, magnetism and 2D van der Waals (vdW) materials [15–17, 20–23, 25, 26, 26, 41–45]. MnBi_2Te_4 's lattice consists of septuple layers (SL) separated by vdW gaps. Its magnetic ground state is layered AFM, which can be further tuned into a ferromagnetic state by a large B field (Fig. 1e). Previous theoretical works have comprehensively studied the electronic, magnetic and topological properties of MnBi_2Te_4 bulk and thin films (SI.V.3) [15, 41–45]. The 2D magnetic and topological ground states can be classified into two kinds. The first kind has an obvious, nonzero static M hosting the Chern insulator state [16, 17, 20–23, 25, 26]. It includes odd-layered MnBi_2Te_4 near $B = 0$ as well as odd-layered and even-layered MnBi_2Te_4 under large B fields. By contrast, the second, more special kind is the even-layered AFM MnBi_2Te_4 , which will be our focus. It is expected to host fully-compensated AFM with an Axion insulator state [16, 17, 41–43] near $B = 0$.

Our magneto-optical setup (Fig. 1f) allows us to investigate the interaction between circularly-polarized light and quantum materials by probing CD, the difference between σ^+ and σ^- light. Importantly, our setup can measure CD both in the reflection and transmission channels and has a supercontinuum light source with tunable wavelength (500 nm to 1000 nm). These capabilities are crucial for our findings, including unique helicity-dependence, wavelength-dependence, and reflection and transmission properties. The measurement temperature is 2 K unless noted otherwise.

Optical induction in a 2D topological antiferromagnet

In this section, we show the observation of optical induction at specific wavelengths. Systematic wavelength dependences will be presented later. As shown in Fig. 2a, starting from $T = 30$ K, we shine σ^+ circularly-polarized light ($\lambda_{\text{induction}} = 840$ nm, $P_{\text{induction}} \simeq 1$ mW) onto a spot on a 8SL MnBi_2Te_4 flake (sample-S1, see Fig. 2e) while lowering its temperature. Upon reaching 2 K, we turn off the induction light and measure the reflection CD (RCD) with the detection light ($\lambda_{\text{detection}} = 946$ nm and $P_{\text{detection}} \simeq 30$ μW). We observe significant anomalous RCD at $B = 0$ (Fig. 2c). We then measure the anomalous RCD while warming up. The RCD vanishes above T_N . From $T = 30$ K, we repeat the same induction process (Fig. 2b) only changing the induction helicity to σ^- . We turn off the induction light at 2 K and repeat the measurements. Remarkably,

the global sign of RCD data is reversed (Fig. 2d). We repeated the induction nine consecutive times (Figs. 2e-g and Extended Data Fig. 4). We find that the RCD at 2 K is consistently controlled by the induction light helicity. On the other hand, when cooling down without induction light, we still observe the anomalous RCD. Only the sign is random (SI.Fig. S17).

Understanding the optical induction by investigating the anomalous CD

Because the anomalous RCD correlates with the AFM order, the data above hint an exciting possibility that induction helicity can control the AFM order in 8SL MnBi₂Te₄. To understand this optical induction, we first investigate the anomalous CD, because it serves as the experimental indicator of the AFM order. Here, we focus on sample-S2 on a diamond substrate, which consists of four connected flakes of 5 – 8 SLs (Extended Data Fig. 5a). We performed systematic RCD measurements (Extended Data Figs. 5c-p). In 5SL and 7SL, we observed the conventional magnetic CD proportional to M . In 6SL and 8SL, we observed the anomalous RCD. We have further confirmed the reproducibility of the anomalous CD in more than 10 samples.

There are two possibilities for the anomalous RCD. (1) It can be the magnetic CD proportional to M (we will explain the origin of M below); (2) Actually, in the absence of any M , there can be an AFM CD unrelated to M but proportional to the AFM order L in \mathcal{PT} symmetric AFMs as reported in Cr₂O₃ [5, 13] (this is symmetry allowed see SI.III), which is also likely the origin of the CD observed in the pseudogap of cuprates [14, 29, 30]. One may think that (1) and (2) can be easily discerned because they are proportional to different order parameters. But in reality this is often not feasible, because the M in an AFM is typically coupled with the AFM order L . For example, suppose our sample is subject to a fixed vertical, static electric field E_z due to substrate, which in turn generates an M due to the static ME coupling α , i.e., $M = \alpha E_z$. Because the two AFM states have opposite α , if one flips the AFM order L , M will also flip. In fact, the induced M turned out to be the dominant mechanism for RCD in even-layered CrI₃ [8, 31]. Therefore, new measurements beyond the RCD are crucial to distinguish the above two possibilities.

We now proceed to show that CD in transmission, i.e., TCD, provides the decisive new measurement, as proposed in Ref. [32, 33]. Magnetic CD is known to also occur in transmission channel (just like the Faraday effect). By contrast, the AFM CD has TCD = 0 because of \mathcal{PT} symmetry. Extended Data Fig. 6a describes a conceptual experiment with σ^- light transmitting through sample. Upon \mathcal{PT} inversion, the even-layered MnBi₂Te₄ remains invariant and light path also stays the same, but light helicity is reversed. As such, \mathcal{PT} enforces the transmission coefficients for σ^\pm light to be identical, which means TCD = 0 (similar analysis can show that RCD is allowed,

Extended Data Fig. 6b). Therefore, what truly distinguishes the AFM CD from the magnetic CD is $\text{TCD} = 0$.

As such, we study TCD and RCD simultaneously in sample-S3, which consists of 5SL and 6SL on diamond (Fig. 3). In 5SL, the magnetic CD indeed shows up prominently in both reflection and transmission. We now turn to 6SL. At 946 nm where significant anomalous RCD was observed at $B = 0$ (Fig. 3b), the TCD, by contrast, is zero. Continuous wavelength dependence (Fig. 3c) shows that, strikingly, TCD is negligibly small over the entire spectrum. Also, we have repeated the RCD *vs.* TCD experiments in sample-S1 (Extended Data Fig. 7), on which the induction experiments were performed. In SI.II.1, we show additional data to further substantiate this. Therefore, we showed that the anomalous RCD in even-layered MnBi_2Te_4 only appears in reflection but is absent in transmission. Such unique reflection and transmission characters, although has been long proposed in theory [32], have never been observed before, allowing us to rule out the magnetic CD due to uncompensated M . As such, the anomalous RCD in even-layered MnBi_2Te_4 is the AFM CD. Below, we show that the AFM CD can be further categorized by the microscopic mechanisms and our results provide the first demonstration of the optical Axion mechanism.

CD arising from the optical Axion electrodynamics

The AFM CD arises from the diagonal optical ME coupling $\alpha(\omega)_{ii}$ [5, 32], but the optical ME coupling has different components corresponding to different microscopic mechanisms. Specifically, the traceless part of $\alpha(\omega)_{ii}$ is known as the gyrotropic birefringence (GB) [$\text{GB} = \frac{1}{3}(\alpha(\omega)_{xx} - \alpha(\omega)_{zz})$] [34, 35]; while the trace part is the Axion contribution $\theta(\omega) = \frac{1}{3} \sum_i \alpha(\omega)_{ii} = \frac{1}{3}[2\alpha(\omega)_{xx} + \alpha(\omega)_{zz}]$ (we have applied $\alpha(\omega)_{xx} = \alpha(\omega)_{yy}$ because of MnBi_2Te_4 's C_{3z} symmetry). However, for a long time, only the GB (traceless part) was theoretically derived [34]. Only very recently, the theory of Axion electrodynamics at optical frequencies was developed [33], which allows us to compute the Axion optical ME coupling in quasi-2D periodic systems (see Methods for expressions). Importantly, in MnBi_2Te_4 , because its bulk respects inversion symmetry, the GB contribution is expected to be negligible, whereas the Axion contribution dominates. As such, MnBi_2Te_4 is an ideal system to isolate the Axion optical ME contribution. Figure 3f shows the calculated GB and $\theta(\omega)$ of 6SL MnBi_2Te_4 , from which we indeed see that Axion $\theta(\omega)$ strongly dominates. Interestingly, as shown in Fig. 3e, the physics of Axion ME coupling can be visualized by a Berry curvature real space dipole (see derivation in the Methods): Because the top and bottom surfaces have opposite Berry curvature, by applying E field, they feature opposite Hall currents. In fact, if one considers the Hall currents on all four facets parallel to E field, one naturally obtains a circulating current, which

leads to an M . This physical picture works for both static and optical Axion ME effects. We only need the following correspondence: the static $E \leftrightarrow$ optical E^ω and Berry curvature \leftrightarrow inter-band Berry curvature. We note that, in contrast to the static limit, for our photon energy (500 – 1000 nm), the optical transition involves many bands, not just the topological surface states; and the contributions from the higher bands are more significant (SI.IV.2).

Using the calculated $\theta(\omega)$, we can theoretically compute RCD (see expressions in SI.IV.1), and thus compare it with the experimental RCD data. We note that the reflection from a surface with a nonlocal ME contribution is a difficult problem with extensive previous discussions [9, 28, 37], and we have carefully considered this (see SI.IV.3). As shown in Figs. 3c,g, we observe good agreement between experimental data and theoretical calculation in terms of the magnitude and the spectral shape. Therefore, by comparing data with calculations, we demonstrated the Axion CD in even-layered MnBi_2Te_4 , i.e., AFM CD arising from the optical Axion electrostatics.

Optical induction arising from the optical Axion electrostatics

Our simultaneous RCD and TCD measurements demonstrated that the M in even-layered MnBi_2Te_4 is negligibly small. Instead, circularly-polarized light with opposite helicity couples differently to the opposite AFM domains. To further confirm that this is also the origin of the optical induction, we now investigate its wavelength dependence. In particular, we notice that the RCD data has distinct spectral dependence (Fig. 3c): E.g. RCD at 840 nm and 540 nm have opposite signs. Therefore, if the induction has the same physical origin as the CD, i.e., the optical Axion electrostatics, then the induction effects using $\lambda_{\text{induction}} = 840$ nm and $\lambda_{\text{induction}} = 540$ nm should be opposite. Specifically, with the same light helicity, the induction using $\lambda_{\text{induction}} = 840$ nm and $\lambda_{\text{induction}} = 540$ nm should lead to opposite AFM domains. As such, we carry out the induction with $\lambda_{\text{induction}} = 540$ nm and 840 nm (note that $\lambda_{\text{detection}}$ is fixed to achieve consistent comparison). By directly comparing Fig. 4a,c ($\lambda_{\text{induction}} = 540$ nm) and Fig. 4b,d ($\lambda_{\text{induction}} = 840$ nm), we indeed find that the results are entirely opposite (see free energy analysis in Fig. 4f). We further study the induction at other wavelengths. As shown in Fig. 4e, our data show that the effect of induction at 540 nm and 580 nm is opposite to that of 740 nm, 840 nm and 946 nm. These results are consistent with the sign of the RCD spectra for even-layered MnBi_2Te_4 , which provide strong evidence that the induction and CD share the same physical origin, i.e., the optical Axion electrostatics. Therefore, we conclude on the observation of the Axion induction, i.e., helicity-dependent control of fully-compensated AFM order based on the optical Axion electrostatics.

Optical creation of AFM domain wall by double induction

The control of AFM order with light helicity makes it possible to spatially modulate the AFM domain structure. For instance, one can think of creating AFM domain wall using two close-by light beams of opposite helicity. Here, we demonstrate this possibility in a 8SL flake (sample-S5). As shown in Fig. 5a, the two light beams are spatially separated and their polarizations can be controlled separately. When both beams are σ^+ polarized (Fig. 5c), the double induction yields one AFM domain, similar to the single induction before. We then change the two beams to σ^+ and σ^- (Fig. 5d). Indeed, the double induction yields opposite AFM domains separated by a domain wall. If we further change the two beams to σ^- and σ^+ , then both AFM domains are flipped and again an AFM domain wall is created. In SI.II.3, we show more systematic data. By double Axion induction, we achieve helicity-dependent optical creation of AFM domain wall for the first time.

Direct optical switching of AFM domain by ultrafast pulse

The optical induction requires warming up the entire sample and then cooling down across T_N with light. To achieve optical writing of complex AFM structures at will, direct optical switching would be highly desirable. We have achieved such direct optical switching of the AFM domain using ultrafast pulsed light with circular polarization. We start from the entire 8SL sample in a single AFM domain (Fig. 6), while the sample is kept at $T = 18$ K (below T_N). We shone ultrafast laser pulses with circular polarization, turned off the ultrafast laser, then checked the AFM order by RCD. As shown in Fig. 6, we indeed directly switch the AFM domain at the ultrafast laser spot with clear helicity dependence. In SI.II.4, we show more systematic data. Direct helicity-dependent optical switching of AFM has never been achieved before. This new result opens a pathway to photolithography for AFM structures.

Discussions

Our results have demonstrated a new type of helicity-dependent optical control (Extended Data Fig. 2): It has been previously known that the rotating electric field of circularly-polarized (CP) light serves as an effective \mathbf{B} field [$(\mathbf{E}^* \times \mathbf{E})$ has the same symmetry as \mathbf{B}], while the rotating electric field multiplies the light propagation vector leads to an effective chiral force [$(\mathbf{E}^* \times \mathbf{E}) \cdot \hat{q}$ has the same symmetry as chirality]. Therefore, CP light can control magnetization M and chirality [4, 11]. In our work, we discovered that CP light can control the AFM order. Such new control can be visualized by the picture that CP light provides an effective Axion $\mathbf{E} \cdot \mathbf{B}$ field [$(\mathbf{E}^* \times \mathbf{E}) \cdot \hat{z}$ has the same symmetry as $\mathbf{E} \cdot \mathbf{B}$], where the rotating electric field of CP light serves as an effective B_z

field and the sample surface normal as an effective E_z . Looking forward, we highlight the following future directions: First, our simultaneous RCD and TCD measurements realize a novel symmetry probe for both \mathcal{T} and \mathcal{PT} , which is valuable to investigate novel \mathcal{T} -breaking phases in unconventional superconductors and charge orders. For instance, optical nonreciprocity (Kerr rotation) with nominally zero magnetization was also observed in unconventional superconductors such as UPt_3 [39–41]. A finite Kerr signal means \mathcal{T} -breaking. Whether this state preserves/breaks \mathcal{PT} symmetry is unknown, which can be learnt by simultaneous transmission experiments. Interestingly, theory predicts exotic \mathcal{PT} -symmetric topological superconductivity [42]. Second, we note that the optical Axion $\theta(\omega)$ electrodynamics is quantum geometrical (i.e., it depends on the geometrical properties of Bloch wavefunction such as Berry curvature) but not topological. This is in contrast to the static θ [43, 44], which can lead to topological quantized effects with exciting experimental progress [17, 45–48]. This means that the optical $\theta(\omega)$ cannot be used to discern topology at photon energies larger than the band gap. On the flip side, it also makes this novel physics more widely applicable in other \mathcal{PT} -symmetric AFMs without mirror planes, including Cr_2O_3 and CrI_3 and even the pseudo-gap state of cuprates [14]. Third, the direct switching by ultrafast pulses (Fig. 6) is potentially on the ultrafast timescale. So future pump probe experiments to directly demonstrate ultrafast AFM reversal would be highly desirable. Finally, for MnBi_2Te_4 , because the AFM order is directly coupled to the sign of static θ angle (a topological invariant) as well as the half-quantized surface Hall conductivity [41–43], our definitive, versatile optical control of AFM domains and domain walls also leads to an optical writing of ballistic circuits of topological chiral edge states.

-
- [1] Basov, D., Averitt, R. & Hsieh, D. Towards properties on demand in quantum materials. *Nature Mater.* **16**, 1077–1088 (2017).
 - [2] Jungwirth, T., Marti, X., Wadley, P. & Wunderlich, J. Antiferromagnetic spintronics. *Nature Nanotech.* **11**, 231–241 (2016).
 - [3] Němec, P., Fiebig, M., Kampfrath, T. & Kimel, A. V. Antiferromagnetic opto-spintronics. *Nature Phys.* **14**, 229–241 (2018).
 - [4] Kirilyuk, A., Kimel, A. V. & Rasing, T. Ultrafast optical manipulation of magnetic order. *Rev. Mod. Phys.* **82**, 2731–2784 (2010).
 - [5] Manz, S. *et al.* Reversible optical switching of antiferromagnetism in TbMnO_3 . *Nature Photon.* **10**,

- 653–656 (2016).
- [6] Higuchi, T. & Kuwata-Gonokami, M. Control of antiferromagnetic domain distribution via polarization-dependent optical annealing. *Nature Commun.* **7**, 10720 (2016).
- [7] Fiebig, M. Revival of the magnetoelectric effect. *Journal of Physics D: Applied Physics* **38**, R123–R152 (2005).
- [8] Jiang, S., Shan, J. & Mak, K. F. Electric-field switching of two-dimensional van der Waals magnets. *Nature Mater.* **17**, 406–410 (2018).
- [9] Gao, A. *et al.* Layer Hall effect in a 2D topological axion antiferromagnet. *Nature* **595**, 521–525 (2021).
- [10] Huck, N. P., Jager, W. F., De Lange, B. & Feringa, B. L. Dynamic control and amplification of molecular chirality by circular polarized light. *Science* **273**, 1686–1688 (1996).
- [11] Xu, S.-Y. *et al.* Spontaneous gyrotropic electronic order in a transition-metal dichalcogenide. *Nature* **578**, 545–549 (2020).
- [12] Krichevtsov, B., Pavlov, V., Pisarev, R. & Gridnev, V. Spontaneous non-reciprocal reflection of light from antiferromagnetic Cr_2O_3 . *J. Phys. Condens. Matter* **5**, 8233–8244 (1993).
- [13] Krichevtsov, B., Pavlov, V., Pisarev, R. & Gridnev, V. Magnetoelectric spectroscopy of electronic transitions in antiferromagnetic Cr_2O_3 . *Phys. Rev. Lett.* **76**, 4628–4631 (1996).
- [14] Xia, J. *et al.* Polar Kerr-effect measurements of the high-temperature $\text{YBa}_2\text{Cu}_3\text{O}_{6+x}$ superconductor: evidence for broken symmetry near the pseudogap temperature. *Phys. Rev. Lett.* **100**, 127002 (2008).
- [15] Otrokov, M. M. *et al.* Prediction and observation of an antiferromagnetic topological insulator. *Nature* **576**, 416–422 (2019).
- [16] Otrokov, M. M. *et al.* Unique thickness-dependent properties of the van der waals interlayer antiferromagnet MnBi_2Te_4 films. *Phys. Rev. Lett.* **122**, 107202 (2019).
- [17] Li, J. *et al.* Intrinsic magnetic topological insulators in van der Waals layered MnBi_2Te_4 -family materials. *Science Advances* **5**, eaaw5685 (2019).
- [18] Zhang, D. *et al.* Topological axion states in the magnetic insulator MnBi_2Te_4 with the quantized magnetoelectric effect. *Phys. Rev. Lett.* **122**, 206401 (2019).
- [19] Zhang, R.-X., Wu, F. & Das Sarma, S. Möbius insulator and higher-order topology in $\text{MnBi}_{2n}\text{Te}_{3n+1}$. *Phys. Rev. Lett.* **124**, 136407 (2020).
- [20] Liu, Z. & Wang, J. Anisotropic topological magnetoelectric effect in axion insulators. *Phys. Rev. B* **101**, 205130 (2020).
- [21] Deng, Y. *et al.* Quantum anomalous Hall effect in intrinsic magnetic topological insulator MnBi_2Te_4 .

- Science* **367**, 895–900 (2020).
- [22] Liu, C. *et al.* Robust axion insulator and Chern insulator phases in a two-dimensional antiferromagnetic topological insulator. *Nature Mater.* **19**, 522–527 (2020).
- [23] Deng, H. *et al.* High-temperature quantum anomalous hall regime in a $\text{MnBi}_2\text{Te}_4/\text{Bi}_2\text{Te}_3$ superlattice. *Nature Phys.* **17**, 36–42 (2021).
- [24] Yang, S. *et al.* Odd-even layer-number effect and layer-dependent magnetic phase diagrams in MnBi_2Te_4 . *Phys. Rev. X* **11**, 011003 (2021).
- [25] Ovchinnikov, D. *et al.* Intertwined topological and magnetic orders in atomically thin Chern insulator MnBi_2Te_4 . *Nano Lett.* **21**, 2544–2550 (2021).
- [26] Cai, J. *et al.* Electric control of a canted-antiferromagnetic Chern insulator. *Nature Commun.* **13**, 1668 (2022).
- [27] Li, Y. *et al.* Nonlocal transport and one-dimensional conduction in the Axion insulator state of MnBi_2Te_4 . Preprint at <https://arxiv.org/abs/2105.10390> (2021).
- [28] Tai, L. *et al.* Distinguishing two-component anomalous Hall effect from topological Hall effect in magnetic topological insulator MnBi_2Te_4 . Preprint at <https://arxiv.org/abs/2103.09878> (2021).
- [29] Orenstein, J. Optical nonreciprocity in magnetic structures related to high- T_c superconductors. *Phys. Rev. Lett.* **107**, 067002 (2011).
- [30] Varma, C. Gyrotropic birefringence in the underdoped cuprates. *Europhys. Lett.* **106**, 27001 (2014).
- [31] Huang, B. *et al.* Electrical control of 2D magnetism in bilayer CrI_3 . *Nature Nanotech.* **13**, 544–548 (2018).
- [32] Canright, G. & Rojo, A. Ellipsometry and broken time-reversal symmetry in the high-temperature superconductors. *Phys. Rev. B* **46**, 14078 (1992).
- [33] Ahn, J., Xu, S.-Y. & Vishwanath, A. Theory of optical axion electrodynamics. Preprint at <https://arxiv.org/abs/2205.06843> (2022) (Please note the same magnetoelectric coefficient is denoted as α in our paper but $G^{(z)}$ in Ref. [9]).
- [34] Malashevich, A. & Souza, I. Band theory of spatial dispersion in magnetoelectrics. *Phys. Rev. B* **82**, 245118 (2010).
- [35] Graham, E. & Raab, R. Macroscopic theory of reflection from antiferromagnetic. *J. Phys.: Condens. Matter* **9**, 1863–1869 (1997).
- [36] Agranovich, V. & Yudson, V. On phenomenological electrodynamics of gyrotropic media. *Opt. Commun.* **9**, 58–60 (1973).
- [37] Halperin, B. I. *The Physics and Chemistry of Oxide Superconductors* (Springer Berlin Heidelberg,

1992).

- [38] Hosur, P., Kapitulnik, A., Kivelson, S., Orenstein, J. & Raghu, S. Kerr effect as evidence of gyrotropic order in the cuprates - revisited. *Phys. Rev. B* **91**, 039908 (2015).
- [39] Xia, J., Maeno, Y., Beyersdorf, P. T., Fejer, M. & Kapitulnik, A. High resolution polar Kerr effect measurements of Sr₂RuO₄: Evidence for broken time-reversal symmetry in the superconducting state. *Phys. Rev. Lett.* **97**, 167002 (2006).
- [40] Schemm, E., Gannon, W., Wishne, C., Halperin, W. & Kapitulnik, A. Observation of broken time-reversal symmetry in the heavy-fermion superconductor UPt₃. *Science* **345**, 190–193 (2014).
- [41] Hayes, I. *et al.* Multicomponent superconducting order parameter in UTe₂. *Science* **373**, 797–801 (2021).
- [42] Kawabata, K., Ashida, Y., Katsura, H. & Ueda, M. Parity-time-symmetric topological superconductor. *Phys. Rev. B* **98**, 085116 (2018).
- [43] Qi, X.-L., Hughes, T. L. & Zhang, S.-C. Topological field theory of time-reversal invariant insulators. *Phys. Rev. B* **78**, 195424 (2008).
- [44] Essin, A. M., Moore, J. E. & Vanderbilt, D. Magnetoelectric polarizability and axion electrodynamics in crystalline insulators. *Phys. Rev. Lett.* **102**, 146805 (2009).
- [45] Wu, L. *et al.* Quantized Faraday and Kerr rotation and axion electrodynamics of a 3D topological insulator. *Science* **354**, 1124–1127 (2016).
- [46] Xiao, D. *et al.* Realization of the axion insulator state in quantum anomalous Hall sandwich heterostructures. *Phys. Rev. Lett.* **120**, 056801 (2018).
- [47] Nenno, D. M., Garcia, C. A., Gooth, J., Felser, C. & Narang, P. Axion physics in condensed-matter systems. *Nature Rev. Phys.* **2**, 682–696 (2020).
- [48] Mogi, M. *et al.* Experimental signature of the parity anomaly in a semi-magnetic topological insulator. *Nature Phys.* **18**, 390–394 (2022).
- [49] Kimura, K., Katsuyoshi, T., Sawada, Y., Kimura, S. & Kimura, T. Imaging switchable magnetoelectric quadrupole domains via nonreciprocal linear dichroism. *Commun. Mater.* **1**, 39 ((2020)).
- [50] Xu, B. *et al.* Infrared study of the multiband low-energy excitations of the topological antiferromagnet MnBi₂Te₄. *Phys. Rev. B* **103**, L121103 (2021).
- [51] Dzyaloshinskii, I. & Papamichail, E. Nonreciprocal optical rotation in antiferromagnets. *Phys. Rev. Lett.* **75**, 3004 (1995).
- [52] Landau, L. D. *et al.* *Electrodynamics of continuous media*, vol. 8 (elsevier, 2013).
- [53] Ahn, J., Xu, S.-Y. & Vishwanath, A. Theory of optical axion electrodynamics. *arXiv preprint*

arXiv:2205.06843 (2022).

- [54] Fried, A. D. Relationship of time-reversal symmetry breaking to optical Kerr rotation. *Phys. Rev. B* **90**, 121112 (2014).
- [55] Armitage, N. Constraints on jones transmission matrices from time-reversal invariance and discrete spatial symmetries. *Phys. Rev. B* **90**, 035135 (2014).
- [56] Huang, B. *et al.* Layer-dependent ferromagnetism in a van der Waals crystal down to the monolayer limit. *Nature* **546**, 270–273 (2017).
- [57] Gong, C. *et al.* Discovery of intrinsic ferromagnetism in two-dimensional van der Waals crystals. *Nature* **546**, 265–269 (2017).
- [58] Ge, J. *et al.* High-Chern-number and high-temperature quantum Hall effect without Landau levels. *Natl. Sci. Rev.* **7**, 1280–1287 (2020).
- [59] Liu, C. *et al.* Helical Chern insulator phase with broken time-reversal symmetry in MnBi_2Te_4 . *Nature Commun.* **12**, 4647 (2021).
- [60] Kharchenko, N., Miloslavskaya, O. & Milner, A. Odd magnetic dichroism of linearly polarized light in the antiferromagnet MnF_2 . *Low temp. Phys.* **31**, 825–830 (2005).

Methods

Crystal growth: Bulk crystals were grown by the flux method [61]. Elemental Mn, Bi and Te were mixed at a molar ratio of 15 : 170 : 270, and sealed in a quartz tube with argon environment. The ampule was first heated to 900°C for 5 hours. It was then moved to another furnace where it slowly cooled from 597°C to 587°C and stayed for one day at 587°C. Finally, MnBi_2Te_4 were obtained by centrifuging the ampule to separate the crystals from the Bi_2Te_3 flux.

Sample fabrication: To preserve the intrinsic properties of 2D MnBi_2Te_4 flakes, the entire device fabrication process was performed without exposure to air, chemicals, or heat in an Ar-filled glovebox with O_2 and water levels below 0.01 ppm. First, thin flakes were mechanically exfoliated on a 300-nm SiO_2/Si wafer. The number of layers was determined based on the optical contrast shown in Ref. [23]. Second, we picked up a desired MnBi_2Te_4 flake and transferred it onto a diamond, sapphire, or hBN substrate by the cryogenic pickup method developed in Ref. [62], where a thin piece of PDMS (polydimethylsiloxane) was cooled to -110° by liquid nitrogen to achieve the pickup. Third, a 20 – 50 nm hBN flake was transferred onto the MnBi_2Te_4 flake. A 200 nm layer of PMMA (poly(methyl methacrylate)) was spin-coated onto the sample to further protect it before transferring it from the glovebox to a cryostat.

Circular dichroism and optical induction: Optical CD measurements were performed in the closed-loop magneto-optical cryostat OptiCool by Quantum Design (base temperature ~ 2 K and B field ± 7 T) using a supercontinuum laser SuperK-EXR20 by NKT photonics (wavelength 500 nm to 2500 nm, pulse width ~ 12 ps at 1064 nm). We focused on 500 – 1000 nm due to constraints of the photodetector, lens, objective and beam splitter. A spectrometer SpectraPro-300i by Acton Research was used to select the wavelength. The beam went through a photoelastic modulator (PEM200, Hinds instruments) operating at $\frac{\lambda}{4}$ retardation with a frequency of 50 kHz. After an optical chopper (1000 Hz) and a broadband plate beam-splitter (near normal, Thorlabs BSW26), the beam was focused onto the sample by a 50X Mitutoyo Plan Apochromat Objective (MY50X-825). The reflected beam went through the cryostat’s top window, was collimated by the same objective, and was collected by a Si Avalanche Photodetector (APD410A, Thorlabs). The transmitted beam was collimated by a parabolic mirror (37-282 Edmund Optics) inside the cryostat and passed through a side window to reach the APD. The corresponding reflection and transmission APD signals were analyzed by two lock-in amplifiers at 50 kHz (the PEM frequency) and 1000 Hz (the chopper frequency), respectively. The RCD and TCD were the ratio of the 50 kHz and 1000 Hz signals. Spatial imaging were achieved using a galvo scanning mirror system. The background CD were obtained by performing the same measurement at a location immediately next to MnBi_2Te_4 flake (SI.II.1). In order to reduce the background CD, the beam splitter (BSW26, Thorlabs) was intentionally used at near normal incidence (Fig. 1f)

Induction experiments were performed using the same supercontinuum laser. The induction light shared the same beam path. When conducting induction experiments, the PEM was turned off. An achromatic $\frac{\lambda}{4}$ waveplate (AQWP10M-580, Thorlabs) was installed before the objective, which generates σ^\pm polarization. After the induction was completed, the induction light was then turned off, and the $\lambda/4$ waveplate was removed from the beam path, allowing us to measure the CD using the PEM. In order to check if the phase of the signal was definitive and consistent, we deliberately turned off and on the PEM multiple times and took the identical measurements. Every time, the phase (sign) of the signal was consistent. We show the data and explain this based on the PEM instrumentation in SI.II.1.

The direct switching was achieved with the sample kept at $T = 18$ K (below $T_N = 25$ K). The pulsed light was generated by an amplified Yb:KGW laser (Pharos, LightConversion) with pulse duration 168 fs, wavelength 1030 nm, repetition rate 100 kHz. The power applied on the sample was 0.04 mW (= 0.4 nJ per pulse). We shone the ultrafast light for 1min, turned it off, and then checked the AFM by RCD.

NV center magnetometry: NV center magnetic imaging was performed using a diamond sample containing a near-surface ensemble of NV centers. A green laser (515 nm, 100 μ W power, beam spot FWHM 400 nm) was used to probe the optically-detected magnetic resonance across the NV ensemble [63]. A pulsed electron spin resonance measurement (500 ns pulse length) was performed on the $|0\rangle$ to $|1\rangle$ NV ground-state transition at a background field of 141 mT along the NV axis (~ 1.08 GHz). To determine the stray field dB due to the flake, a linear plane-fit background is subtracted from the raw field image. The NV detection limit was about $2\mu_B/\text{nm}^2$.

Optical Axion Electrodynamics:

- θ and $\mathbf{E} \cdot \mathbf{B}$ have identical symmetry properties. They require the breaking of \mathcal{P} , \mathcal{T} and all mirrors. Note that there are \mathcal{PT} -symmetric phases with mirror symmetry [49]. They do not support the Axion optical ME coupling because mirror forces $\theta = 0$ but they can support other novel optical effect such as the nonreciprocal directional dichroism.
- By adding $\theta(\omega)\frac{e^2}{2\pi\hbar c}\mathbf{E}^\omega \cdot \mathbf{B}^\omega$ into the Lagrangian, the modified Maxwell's equations read

$$\nabla \cdot \mathbf{E}^\omega = \rho - \frac{e^2}{2\pi\hbar c}\nabla\theta(\omega) \cdot \mathbf{B}^\omega \quad (1)$$

$$\nabla \times \mathbf{B}^\omega = \partial_t \mathbf{E}^\omega + \mathbf{j}^\omega + \frac{e^2}{2\pi\hbar c}(\nabla\theta(\omega) \times \mathbf{E}^\omega + \partial_t\theta(\omega)\mathbf{B}^\omega) \quad (2)$$

The other equations (the Gauss's law for magnetism and the Faraday's law) are unchanged.

- The low frequency limit is defined as frequencies below the magnetic gap at the surface Dirac point, which is typically ~ 10 meV in magnetic topological insulators. Therefore, according to this definition, terahertz light is in the low frequency limit.
- According to Ref. [33], $\theta(\omega)$ is given by

$$\theta(\omega) = \pi \frac{2\hbar}{e^2} \frac{1}{3}(2\alpha(\omega)_{xx} + \alpha(\omega)_{zz}), \quad (3)$$

$$\alpha_{xx}(\omega) = \frac{e^2}{\hbar L} \sum_{\text{o,u}} \int d^2\mathbf{k} \frac{\varepsilon_{\text{uo}}}{\varepsilon_{\text{uo}} - \hbar\omega} \text{Im} \left[\frac{\hbar^2 \langle \text{o} | \hat{v}^x | \text{u} \rangle \langle \text{u} | -\frac{1}{2}(\hat{v}^y \hat{r}^z + \hat{r}^z \hat{v}^y) + \hat{m}_x^s | \text{o} \rangle}{\varepsilon_{\text{uo}}^2} \right], \quad (4)$$

$$\alpha_{zz}(\omega) = \frac{e^2}{\hbar L} \sum_{\text{o,u}} \int d^2\mathbf{k} \frac{\varepsilon_{\text{uo}}}{\varepsilon_{\text{uo}} - \hbar\omega} \text{Im} \left[\frac{\frac{\hbar^2}{2} (\langle \text{o} | \hat{r}^z | \text{u} \rangle \langle \text{u} | \hat{v}^x \hat{v}^y | \text{o} \rangle - \langle \text{o} | \hat{r}^z \hat{v}^x | \text{u} \rangle \langle \text{u} | \hat{v}^y | \text{o} \rangle - (x \leftrightarrow y)) + \hbar^2 \langle \text{o} | \hat{v}^z | \text{u} \rangle \langle \text{u} | \hat{m}_z^s | \text{o} \rangle}{\varepsilon_{\text{uo}}^2} \right] \quad (5)$$

where L is the sample thickness, $\varepsilon_{\text{uo}}(\mathbf{k})$ is the energy difference between occupied (o) and unoccupied (u) states, \hat{v}_x and \hat{v}_y are velocity operators, \hat{r}_z is the position operator along z , and \hat{m}^s is the spin operator.

- To get the Berry curvature real space dipole, we start from $\alpha(\omega)_{xx}$ (because the traceless part is small, $\theta(\omega) \simeq \pi \frac{2\hbar}{e^2} \alpha(\omega)_{xx}$).

$$\begin{aligned}
\alpha(\omega)_{xx} &= \frac{e^2}{\hbar L} \sum_{o,u} \int d^2\mathbf{k} \frac{\varepsilon_{uo}}{\varepsilon_{uo} - \hbar\omega} \text{Im} \left[\frac{\hbar^2 \langle o|\hat{v}^x|u\rangle \langle u|\hat{v}^y\hat{r}^z|o\rangle}{\varepsilon_{uo}^2} \right] \\
&= \frac{e^2}{\hbar L} \sum_{o,u} \int d^2\mathbf{k} \frac{\varepsilon_{uo}}{\varepsilon_{uo} - \hbar\omega} \text{Im} \left[\frac{\hbar^2 \langle o|\hat{v}^x|u\rangle \sum_{\mathbf{p}} \langle u|\hat{v}^y|\mathbf{p}(\mathbf{k})\rangle \langle \mathbf{p}(\mathbf{k})|\hat{r}^z|o\rangle}{\varepsilon_{uo}^2} \right] \\
&\simeq \frac{e^2}{\hbar L} \sum_{o,u} \int d^2\mathbf{k} \frac{\varepsilon_{uo}}{\varepsilon_{uo} - \hbar\omega} \langle \hat{r}^z \rangle_o \text{Im} \left[\frac{\hbar^2 \langle o|\hat{v}^x|u\rangle \sum_{\mathbf{p}} \langle u|\hat{v}^y|\mathbf{p}(\mathbf{k})\rangle \delta_{\mathbf{p}o}}{\varepsilon_{uo}^2} \right] \\
&= \frac{e^2}{\hbar L} \sum_{o,u} \int d^2\mathbf{k} \frac{\varepsilon_{uo}}{\varepsilon_{uo} - \hbar\omega} \langle \hat{r}^z \rangle_o \text{Im} \left[\frac{\hbar^2 \langle o|\hat{v}^x|u\rangle \langle u|\hat{v}^y|o\rangle}{\varepsilon_{uo}^2} \right] \\
&= \frac{e^2}{2\hbar L} \sum_{o,u} \int d^2\mathbf{k} \frac{\varepsilon_{uo}(\mathbf{k})}{\varepsilon_{uo}(\mathbf{k}) - \hbar\omega} \langle \hat{r}^z \rangle_o \Omega_{uo}
\end{aligned} \tag{6}$$

Therefore, the Berry curvature real space dipole is a good approximation when the wavefunction of the electronic states is concentrated in a particular layer ($\langle \mathbf{p}(\mathbf{k})|\hat{r}^z|o\rangle \simeq \delta_{\mathbf{p}o} \langle \hat{r}^z \rangle_o$). In MnBi_2Te_4 , because it is a vdW layered material, the interlayer coupling is expected to be relatively weak. Hence, the wavefunction of the electronics states is relatively localized.

Free energy analysis: Similar to previous works [4, 11], we expand the system's free energy in the presence of light. Here we assume the light propagates along $\hat{\mathbf{z}}$.

$$\delta F = \beta \mathbf{M} \cdot [\mathbf{E}^* \times \mathbf{E}] + \gamma \Phi_{\text{chiral}} [\mathbf{E}^* \times \mathbf{E}] \cdot \hat{\mathbf{q}} + \xi L_z [\mathbf{E}^* \times \mathbf{E}] \cdot \hat{\mathbf{z}}, \tag{7}$$

where \mathbf{E} and $\hat{\mathbf{q}}$ are the electric field and unit wavevector of light; \mathbf{M} , Φ_{chiral} and \mathbf{L} are the order parameters for FM, chiral crystals and AFM, respectively; β , γ and ξ are the corresponding coupling tensors. First, we explain how each term is constructed. The guiding principle [65] is that a valid free energy term must be invariant under all symmetries. For instance, \mathbf{M} is odd under \mathcal{T} but even under \mathcal{P} ; one can check that the same is true for $[\mathbf{E}^* \times \mathbf{E}]$, so that $\mathbf{M} \cdot [\mathbf{E}^* \times \mathbf{E}]$ is invariant under both \mathcal{T} and \mathcal{P} . Similarly, the spatially-chiral order Φ_{chiral} is odd under \mathcal{P} but even under \mathcal{T} , and the same is true for $[\mathbf{E}^* \times \mathbf{E}] \cdot \hat{\mathbf{q}}$. The AFM order L_z (as in even-layered MnBi_2Te_4) is odd under both \mathcal{P} and \mathcal{T} , and the same is true for $[\mathbf{E}^* \times \mathbf{E}] \cdot \hat{\mathbf{z}}$.

Next, we explain the physical meaning of each term. Importantly, one can check that $\mathbf{E}^* \times \mathbf{E}$, $[\mathbf{E}^* \times \mathbf{E}] \cdot \hat{\mathbf{q}}$, and $[\mathbf{E}^* \times \mathbf{E}] \cdot \hat{\mathbf{z}}$ all flip sign upon reversing light helicity (while keeping the propagation direction invariant). The first term is the energy coupling between M and circularly-polarized light, which is responsible for the helicity-dependent optical control of magnetization observed in FMs [4]. The second term is the energy coupling between spatial chirality and circularly-polarized

light, which is responsible for the helicity-dependent optical control of spatial chirality observed in asymmetrical chemical reactions [10] and gyrotropic electronic order [11]. The last term is the energy coupling between the fully-compensated AFM order and circularly-polarized light, which is responsible for the helicity-dependent optical control of the fully-compensated AFM order, achieved for the first time in even-layered MnBi_2Te_4 here. The coupling constant ξ directly arises from the optical Axion electrodynamics, as we demonstrated from the data above.

First-principles calculations: First-principles band structure calculations were performed using the projector augmented wave method as implemented in the VASP package within the generalized gradient approximation (GGA) schemes. $9 \times 9 \times 1$ Monkhorst-Pack k -point meshes with an energy cutoff of 400 eV were adapted for the Brillouin zone integration. Experimentally determined lattice parameters were used. In order to treat the localized Mn $3d$ orbitals, we follow previous first-principles works [15, 64] on MnBi_2Te_4 and used an onsite $U = 5.0$ eV. The Wannier model for the few-layered MnBi_2Te_4 was built using the Bi p , Te p and Mn d orbitals. All optical response functions were calculated based on the Wannier model.

-
- [61] Yan, J.-Q. *et al.* Crystal growth and magnetic structure of MnBi_2Te_4 . *Phys. Rev. Mater.* **3**, 064202 (2019).
- [62] Zhao, S. Y. F. *et al.* Emergent Interfacial Superconductivity between Twisted Cuprate Superconductors. Preprint at arXiv:2108.13455 (2021).
- [63] Thiel, L. *et al.* Probing magnetism in 2D materials at the nanoscale with single-spin microscopy. *Science* **364**, 973–976 (2019).
- [64] Otrokov, M. M. *et al.* Unique thickness-dependent properties of the van der Waals interlayer antiferromagnet MnBi_2Te_4 films. *Phys. Rev. Lett.* **122**, 107202 (2019).
- [65] Toledano, J.-C. & Toledano, P. *The Landau theory of phase transitions: application to structural, incommensurate, magnetic and liquid crystal systems* (World Scientific, 1987).
- [66] Ahn, J., Guo, G.-Y., Nagaosa, N. & Vishwanath, A. Riemannian geometry of resonant optical responses. *Nature Phys.* **18**, 290-295 (2022).

Data availability: The data that support the plots within this paper and other findings of this study are available from the corresponding author upon reasonable request.

Acknowledgement: We gratefully thank Xiaodong Xu and Tiancheng Song for sharing expe-

rience on CD setup and Manfred Fiebig for providing the Cr_2O_3 bulk crystals. We also thank Yang Gao, Bertrand I. Halperin, Pavon Hosur, and Philip Kim for helpful discussions. Work in the SYX group was supported through NSF Career (Harvard fund 129522) DMR-2143177. SYX acknowledge the Corning Fund for Faculty Development. SYX, JA, QM, AV acknowledge support from the Center for the Advancement of Topological Semimetals, an Energy Frontier Research Center funded by the U.S. Department of Energy (DOE) Office of Science, through the Ames Laboratory under contract DE-AC0207CH11358. QM was also supported through the CIFAR Azrieli Global Scholars programme. CT acknowledges support from the Swiss National Science Foundation under project P2EZP2_191801. YFL, SYX, and DCB were supported by the STC Center for Integrated Quantum Materials (CIQM), NSF Grant No. DMR-1231319. This work was performed in part at the Center for Nanoscale Systems (CNS) Harvard University, a member of the National Nanotechnology Coordinated Infrastructure Network (NNCI), which is supported by the National Science Foundation under NSF award no.1541959. Work at UCLA was supported by the U.S. Department of Energy (DOE), office of Science, office of Basic Energy Sciences under Award Number DE-SC0021117. The work at TIFR Mumbai is supported by the Department of Atomic Energy of the government of India under Project No. 12-R&D-TFR-5.10-0100. The work at Northeastern University was supported by the Air Force Office of Scientific Research under award number FA9550-20-1-0322, and it benefited from the computational resources of Northeastern University's Advanced Scientific Computation Center (ASCC) and the Discovery Cluster. H.L. acknowledges the support by the National Science and Technology Council (NSTC) in Taiwan under grant number MOST 111-2112-M-001-057-MY3. T.-R.C. was supported by the 2030 Cross-Generation Young Scholars Program from the National Science and Technology Council (NSTC) in Taiwan (Program No. MOST111-2628-M-006-003-MY3), National Cheng Kung University (NCKU), Taiwan, and National Center for Theoretical Sciences, Taiwan. This research was supported, in part, by Higher Education Sprout Project, Ministry of Education to the Headquarters of University Advancement at NCKU. HZL was supported by the National Key R&D Program of China (2022YFA1403700), the National Natural Science Foundation of China (11925402), Guangdong province (2016ZT06D348, 2020KCXTD001), the Science, Technology and Innovation Commission of Shenzhen Municipality (ZDSYS20170303165926217, JCYJ20170412152620376, KYTDPT20181011104202253), and Center for Computational Science and Engineering of SUSTech. K.W. and T.T. acknowledge support from JSPS KAKENHI (Grant Numbers 19H05790, 20H00354 and 21H05233). X-YZ, Y-XW, and BBZ acknowledge support from the NSF award No. ECCS-2041779.

Author contributions: JXQ performed the optical measurements and analyzed data with

help from CT and HCL. JXQ performed the transport measurements with help from AG. AG fabricated the 2D MnBi_2Te_4 samples with help from JXQ, HCL, YFL, DB, TD, SCH, and QM. CH and NN grew the bulk MnBi_2Te_4 single crystals. JA and AV developed the theory of optical Axion electrodynamics with discussions with SYX. BG and JA made first-principles calculations with helps BS from under supervisions of HS, TRC, AB, and AV. ZHG and HZL did model simulations. DCB performed transmission electron microscope measurements. X-YZ, Y-XW, and BBZ performed nitrogen-vacancy center magnetometry experiments. KW and TT grew the bulk hBN single crystals. SYX, JXQ and QM wrote the manuscript with input from all authors. JXQ came up with the idea of optical induction of AFM. SYX supervised the project and was responsible for the overall direction, planning and integration among different research units.

Competing financial interests: The authors declare no competing financial interests.

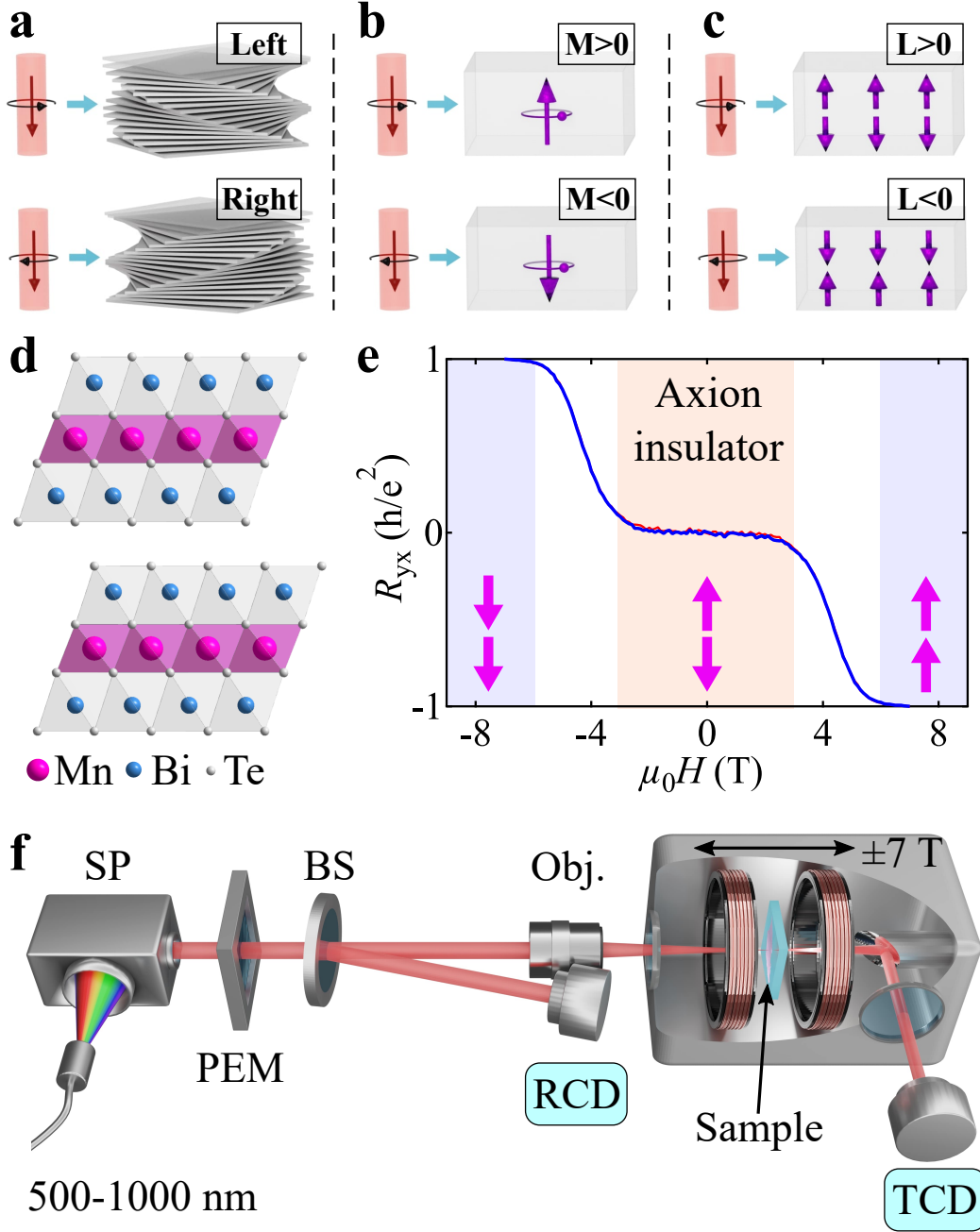


FIG. 1: **Helicity-dependent optical control of quantum matter and introduction to MnBi_2Te_4 .** **a,b**, Previous studies have demonstrated helicity-dependent optical control of spatial chirality and magnetization [4, 10, 11]. **c**, We report the surprising observation of helicity-dependent optical control of fully-compensated antiferromagnetic (AFM) order. **d**, Lattice structure of MnBi_2Te_4 . **e**, Hall resistivity of our 6SL MnBi_2Te_4 with the layered magnetic state shown by the pink arrows. For each state, two out of six layers are pictured for simplicity. The Axion insulator state is realized by the fully-compensated AFM near $B = 0$. **f**, Our circular dichroism set up. SP, PEM, BS, Obj. are spectrometer, photoelastic modulator, beam-splitter, and objective, respectively.

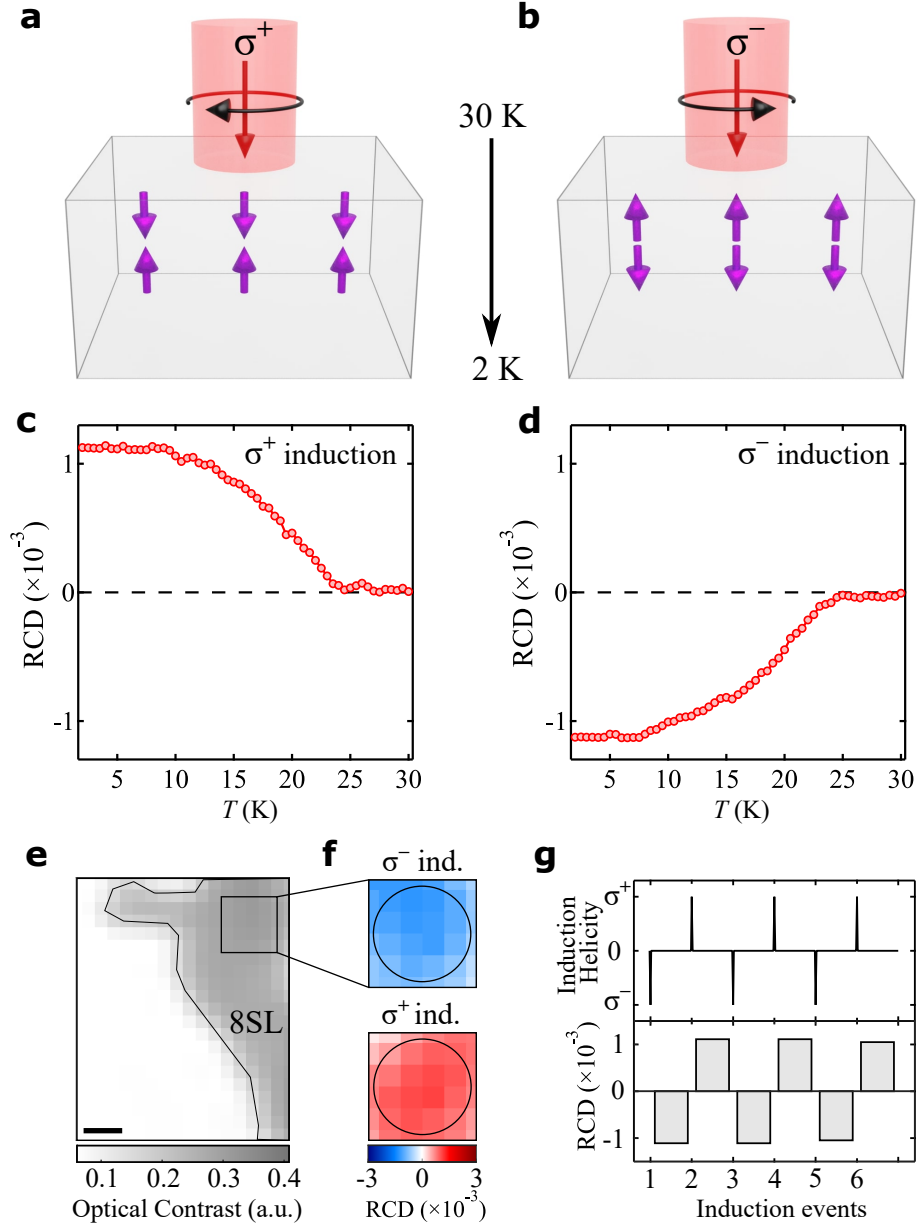


FIG. 2: **Optical induction in a 2D topological antiferromagnet.** **a**, We shine σ^+ circularly-polarized induction light ($\lambda_{\text{induction}} = 840$ nm, $P_{\text{induction}} \simeq 1$ mW) on the sample S1 (8SL MnBi_2Te_4 flake on a sapphire substrate) while lowering its temperature from $T = 30$ K to 2 K. **c**, Upon reaching 2 K, we turn off the induction light and measure the reflection CD (RCD) with the detection light at $\lambda_{\text{detection}} = 946$ nm and $P_{\text{detection}} \simeq 30$ μW . Surprisingly, we observe a significant RCD at $B = 0$. Upon warming up, the RCD vanishes above T_N . **b,d**, Same as panels (a,c) except that we shine σ^- circularly-polarized induction light on the sample while lowering its temperature from $T = 30$ K to 2 K. **e**, Spatial mapping of the optical contrast near the 8SL flake. Scale bar: 2 μm . **f**, RCD signal after induction with opposite helicity. The circle marks the spot subject to the induction light while cooling. **g**, RCD signal at the center of the circle in panel (f) after consecutive induction processes with opposite helicity.

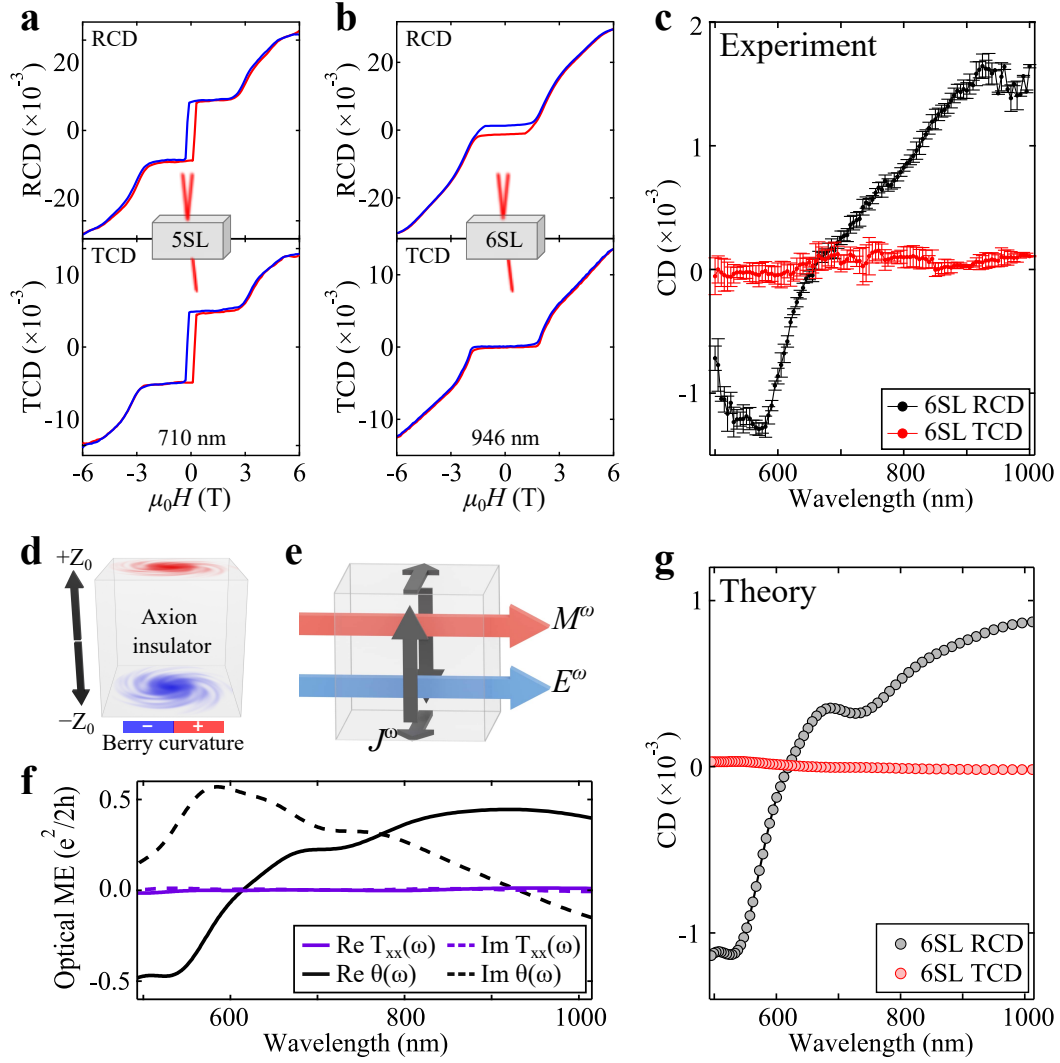


FIG. 3: **Unique reflection and transmission properties and observation of the Axion CD.** **a,b,** Simultaneous RCD and TCD measurements of the 5SL (panel **a**) and 6SL (panel **b**) in sample-S3. **c,** Wavelength dependence of RCD and TCD at $B = 0$ for 6SL. **d,** Schematic illustration of the Berry curvature real-space dipole. Electrons at opposite positions ($\pm Z$) in even-layered MnBi_2Te_4 have opposite Berry curvature. **e,** the Axion optical ME coupling can be visualized as an itinerant electron circulation in response to electric field as a consequence of the Berry curvature real-space dipole. **f,** Optical Axion $\theta(\omega)$ and gyrotropic birefringence (T_{xx}) of 6SL MnBi_2Te_4 calculated from first-principles band structures. **g,** Theoretically computed RCD and TCD, which are obtained directly from the calculated $\alpha(\omega)$ (see expressions in SI.IV.1). The TCD is strictly zero with perfect \mathcal{PT} symmetry. The calculated TCD here takes account into the weak \mathcal{PT} breaking due to asymmetric dielectric environment (hBN and diamond, see details in SI.IV.1.(5)).

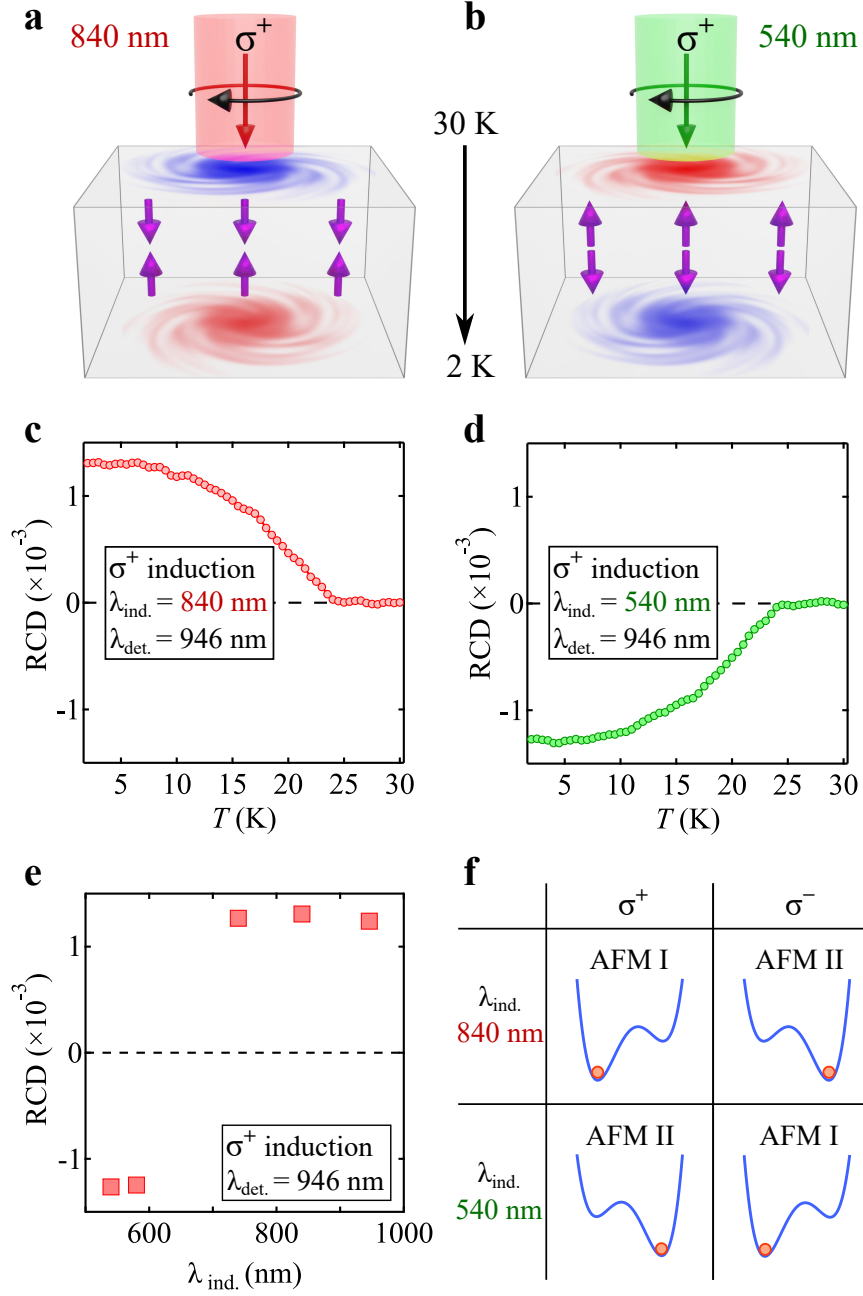


FIG. 4: Observation of the Axion induction. **a,c**, We shine σ^+ circularly-polarized induction light ($\lambda_{\text{induction}} = 540$ nm, $P_{\text{induction}} \simeq 1$ mW) on the 8SL MnBi_2Te_4 flake (sample-S1) while lowering its temperature from $T = 30$ K to 2 K (panel **a**). We turn off the induction light and measure the RCD with $\lambda_{\text{detection}} = 946$ nm while warming up (panel **c**). **b,d**, Same as panels (**a,c**) except the induction wavelength is $\lambda_{\text{induction}} = 840$ nm. **e**, Induction wavelength dependence. To consistently compare how induction wavelength $\lambda_{\text{induction}}$ influences the results of induction, we fix all other experimental parameters including induction helicity (fixed at σ^+) and detection wavelength (fixed at $\lambda_{\text{detection}} = 946$ nm) and we only vary $\lambda_{\text{induction}}$. **f**, Free energy diagrams summarize the optical control of the AFM order in even-layered MnBi_2Te_4 with light helicity and wavelength.

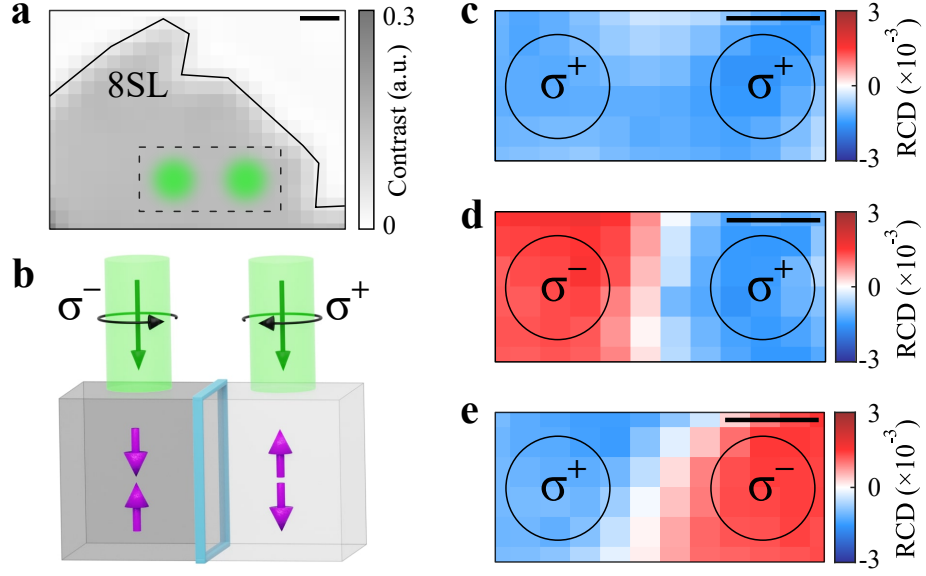


FIG. 5: **Optical creation of AFM domain wall by double Axion induction.** **a**, We shine two close-by circularly-polarized induction light beams on an 8SL MnBi₂Te₄ flake (sample-S5). Scale bar: 2 μm. $\lambda_{\text{induction}} = 540$ nm. **b**, Schematic illustration of the double induction leading to an AFM domain wall. **c-e**, RCD mappings of the area subject to the double induction with (σ^+, σ^+) , (σ^-, σ^+) , and (σ^+, σ^-) , respectively.

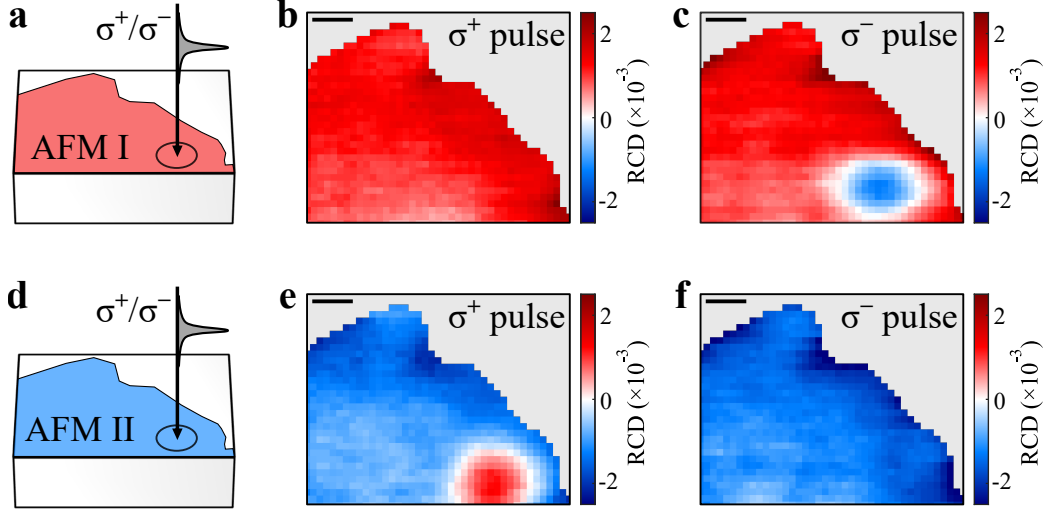
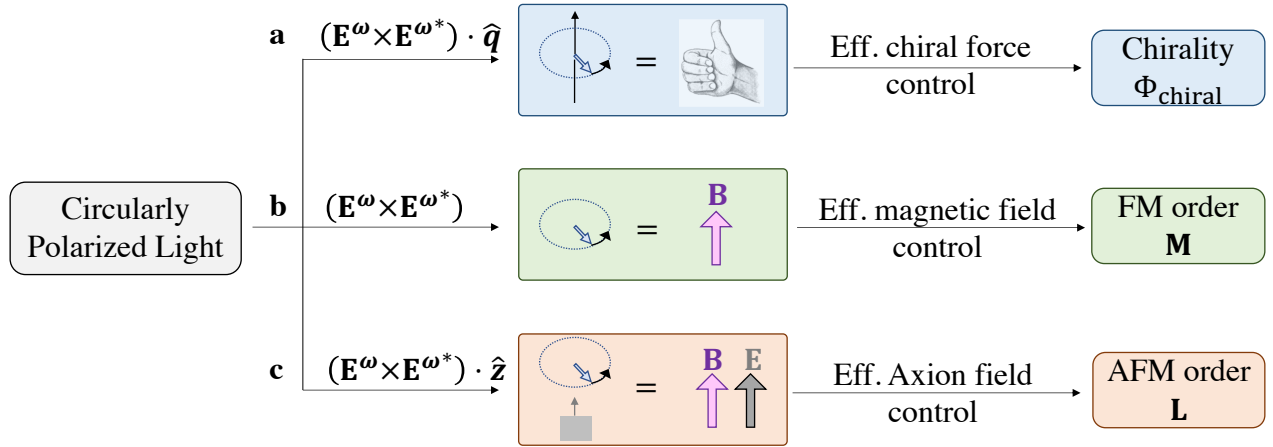
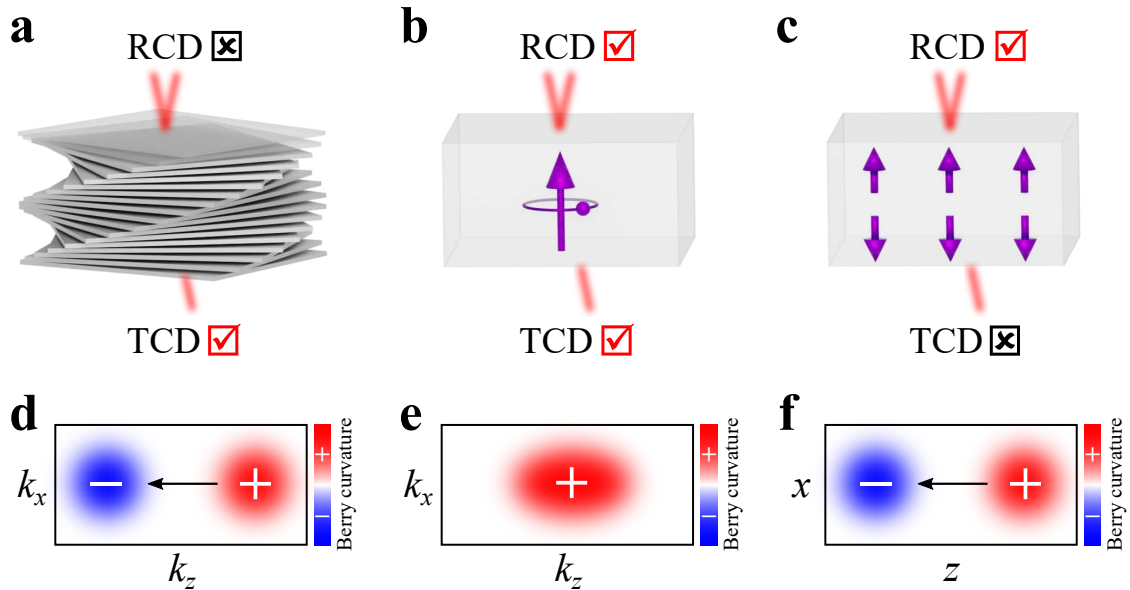


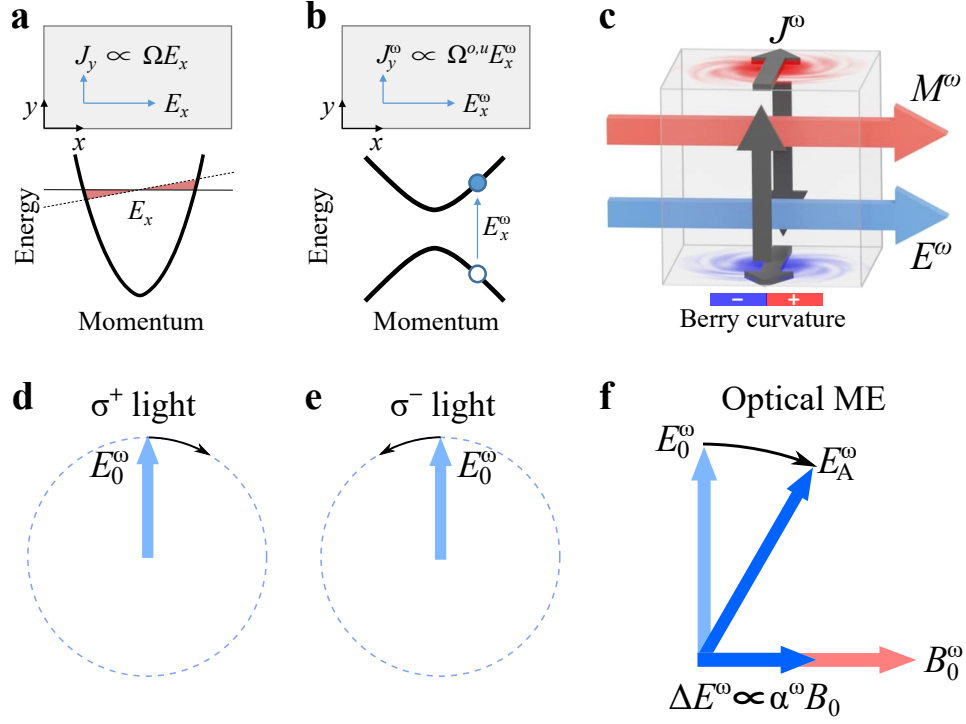
FIG. 6: **Direct optical switch of AFM order by ultrafast pulse with circularly polarization.** **a**, Schematic illustration of the entire 8SL sample (sample-S1) in the same AFM domain (achieved by sweeping the B field from +7 T to 0 T). We shine circularly-polarized ultrafast pulsed light while keeping the sample at $T = 18$ K (below $T_N = 25$ K). **b,c**, RCD maps after shining circularly-polarized ultrafast pulsed light. **d-f**, The same as panels (**a-c**) but for the opposite AFM domain prepared by sweeping the B field from -7 T to 0 T. See additional data in SI.II.4. Scale bar: $2 \mu\text{m}$.



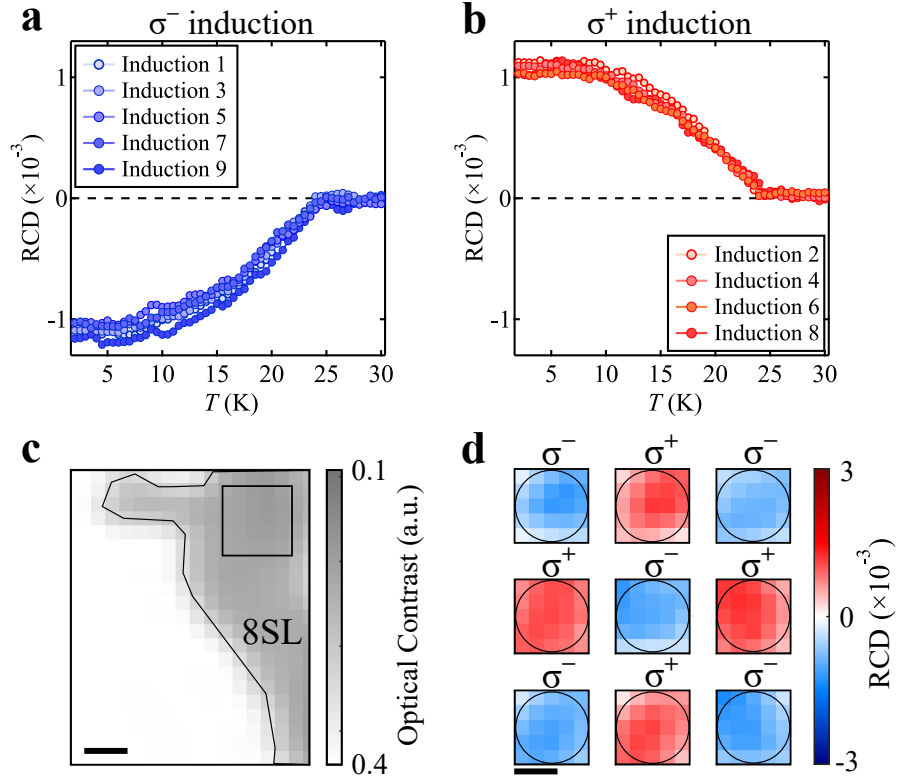
Extended Data Fig. 1: Distinct mechanism for the three classes of helicity-dependent optical control. $(\mathbf{E}^\omega \times \mathbf{E}^{\omega*}) \cdot \hat{\mathbf{q}}$, $(\mathbf{E}^\omega \times \mathbf{E}^{\omega*})$, and $(\mathbf{E}^\omega \times \mathbf{E}^{\omega*}) \cdot \hat{\mathbf{z}}$ are symmetry-equivalent to chirality, \mathbf{B} and $\mathbf{E} \cdot \mathbf{B}$, respectively.



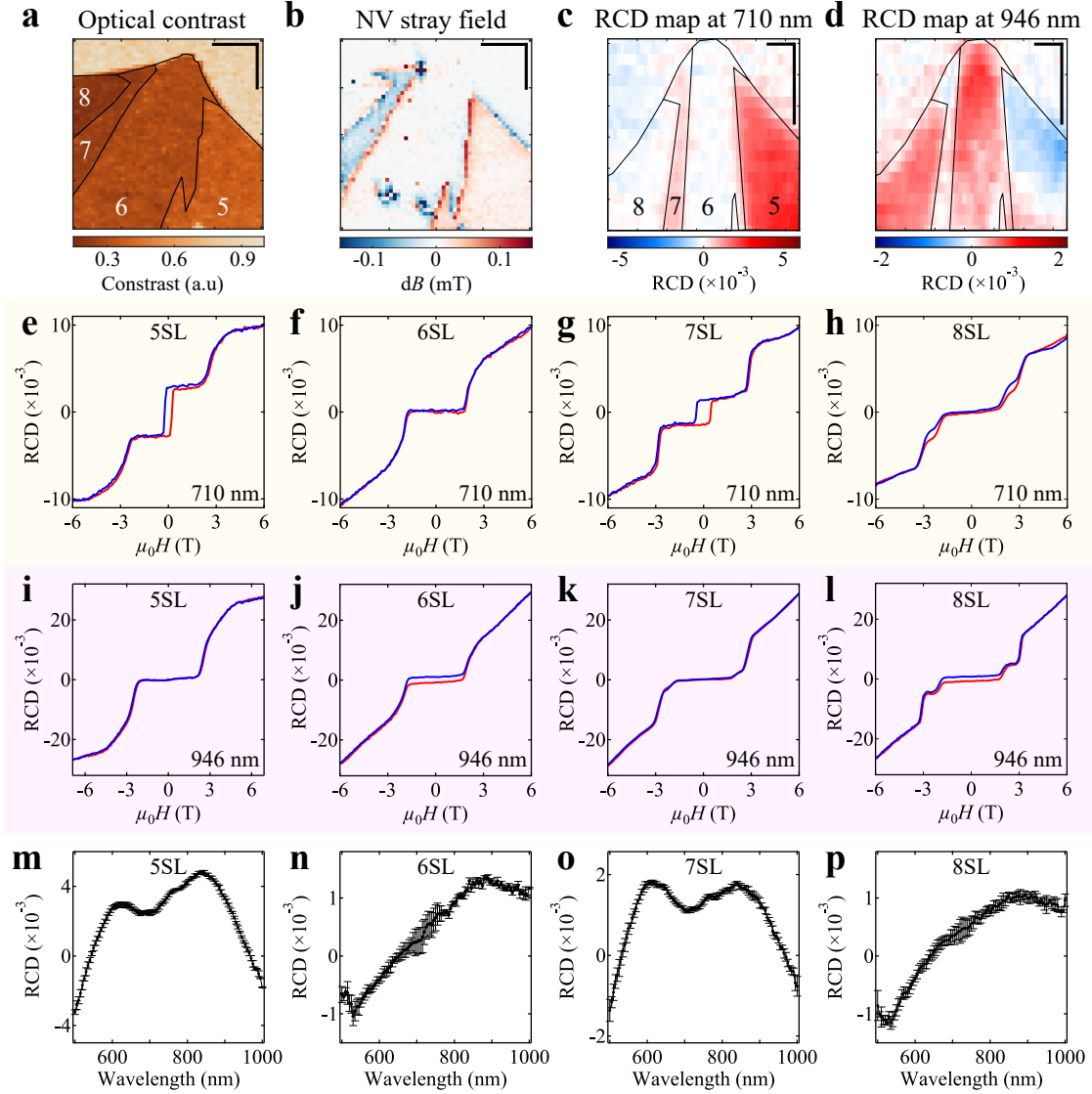
Extended Data Fig. 2: Three classes of CD in chiral crystals, ferromagnets and \mathcal{PT} -symmetric AFM. **a-c**, Chiral crystals, ferromagnets and \mathcal{PT} -symmetric AFM feature distinct nontrivial interactions with circularly-polarized light. They can only be distinguished by their transmission and reflection properties. **d-f**, Equally importantly, when bands with nontrivial topology or giant Berry curvature occur in these three classes of materials, the respective CD can dominantly arise from the Berry curvature properties, namely the Berry curvature k space dipole, the total Berry curvature, and the Berry curvature real space dipole, respectively.



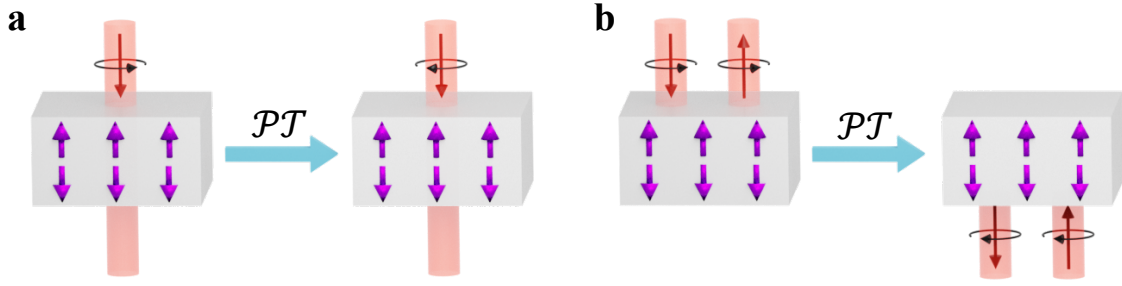
Extended Data Fig. 3: **a**, The Berry curvature causes transverse electron motion in response to an external DC E field. **b**, Analogously, the inter-band Berry curvature causes a transverse electron motion in response to light's E^ω field upon an interband transition. Ref. [66] provides a detailed theoretical analysis for the clear geometrical origin of the inter-band Berry curvature. **c**, The Berry curvature induced optical ME coupling can be visualized as an itinerant electron circulation in response to electric field. Specifically, upon the application of an electric field E^ω , Berry curvature leads to transverse electron motion. Because of the Berry curvature at $\pm Z$ is opposite, the transverse motions of electrons at $\pm Z$ are in opposite directions. This in turn leads to an itinerant electron circulation J^ω , which is equivalent to magnetization M^ω . **d,e**, Rotation of electric field E_0^ω for σ^\pm light. **f**, Light's magnetic field B^ω can lead to an electric polarization $P_0^\omega = \alpha(\omega)B_0^\omega$ through the optical ME effect, which rotates light's electric field E^ω . Suppose this rotation is in the clockwise direction. Then, this additional clockwise rotation would be along the same direction as the intrinsic rotation (also clockwise) for σ^+ light but opposite to the intrinsic rotation (counter-clockwise) for σ^- light. This provides an intuitive picture for why σ^\pm light can behave differently in an Axion insulator, a prerequisite for nonzero CD.



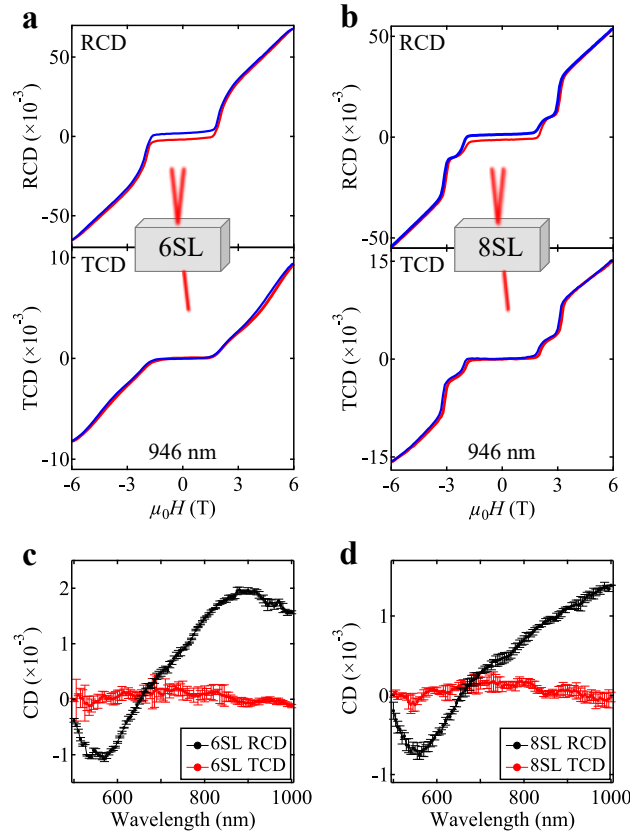
Extended Data Fig. 4: Reproducible RCD measurements for nine consecutive inductions with alternating induction helicities. **a**, RCD as a function of temperature while warming up after induction with σ^- light. **b**, Same as panel (a) but after induction with σ^+ light. **c**, Spatial mapping of the optical contrast near the 8SL MnBi₂Te₄ flake. The square box marks the region for induction experiments. **d**, RCD map after induction with opposite helicity. The circle marks the spot that is subject to the induction light while cooling; The σ^+ and σ^- on each small panel denotes the helicity of the induction light. Experimental parameters used for data in this figure: $\lambda_{\text{induction}} = 840$ nm, $P_{\text{induction}} \simeq 1$ mW; $\lambda_{\text{detection}} = 946$ nm, $P_{\text{detection}} \simeq 30$ μ W. Scale bars for panels (e,f) are 2 μ m.



Extended Data Fig. 5: Circular dichroism in 2D MnBi_2Te_4 . **a**, Optical contrast of sample-S2 on diamond structure, which consists of four connected flakes of 5SL, 6SL, 7SL and 8SL. **b**, Nitrogen vacancy center measured stray magnetic field of sample S2. **c**, RCD spatial mapping at $B = 0$ using $\lambda_{\text{detection}} = 710$ nm. The sample was cooled down with a finite B field and the B field was ramped to zero before the measurements. **d**, Same as panel **c** but using $\lambda_{\text{detection}} = 946$ nm with. No optical induction was performed in panels **c,d**. Scale bars (horizontal and vertical lines) are all $5 \mu\text{m}$. We note that the NV and CD measurements were performed in different setups. Hence the spatial mappings (**b** and **c,d**) are rotated with respect to each other. **e-h**, Magnetic hysteresis of RCD for 5SL, 6SL, 7SL and 8SL measured at $\lambda_{\text{detection}} = 710$ nm. **i-l**, Same as panels (**e-h**) but measured at $\lambda_{\text{detection}} = 946$ nm. **m-p**, RCD spectra at $B = 0$ for 5-8SL. The spectrum strongly depends on the evenness or oddness of the layer number, consistent with the different physical origins of the CDs in even and odd layers. It is interesting to note that ~ 700 nm is the symmetric (antisymmetric) point for odd (even) layers.



Extended Data Fig. 6: Symmetry analysis for CD in \mathcal{PT} -symmetric AFM. **a**, σ^- light transmitting through a sample. Upon \mathcal{PT} inversion, the AFM remains invariant and the light path also stays the same, but light helicity is reversed. As such, \mathcal{PT} enforces the transmission for σ^\pm to be identical, which means $\text{TCD} = 0$. **b**, σ^- light reflecting off a sample. Upon \mathcal{PT} inversion, the AFM remains invariant but the reflection is changed to the bottom surface. This means that \mathcal{PT} does not impose any constraint on RCD experiments, because RCD compares the reflections of σ^\pm lights from the same side of the sample. Carrying out the same analysis exhaustively confirms that there is no symmetry that can relate the reflections of light with opposite helicity while keeping the AFM invariant. Therefore, RCD is allowed.



Extended Data Fig. 7: RCD vs. TCD measurements of the 6SL and 8SL MnBi₂Te₄ in sample-S1. **a,b**, RCD and TCD magnetic hysteresis measurements at 946 nm. **c**, RCD and TCD spectra at $B = 0$.

Supplemental Information for
Axion optical induction of antiferromagnetic order

Table of contents:

- I. Addressing alternative origins for CD in even-layered MnBi_2Te_4
 - I.1. Protection layers (PMMA/hBN) induced CD
 - I.2. Uncompensated magnetization induced magnetic CD
 - I.3. Light attenuation induced residual CD
 - I.4. Higher order effects
- II. Additional data
 - II.1. Additional CD data
 - II.2. Additional induction data
 - II.3. Additional double induction data
 - II.4. Additional ultrafast switching data
 - II.5. Additional electrical transport data
- III. Symmetry analysis of the CD
 - III.1. General principles
 - III.2. Three classes of materials and their symmetries
 - III.3. Application to AFM and other systems
 - III.4. Math derivation for symmetry analysis
- IV. Theoretical studies
 - IV.1. Theoretical expressions for calculating the Axion CD
 - IV.2. Band structure of MnBi_2Te_4 and additional calculations
 - IV.3. Mathematical derivation of RCD/Kerr under different symmetry condition
- V. Additional discussions
 - V.1. Additional discussion about Berry curvature real space dipole
 - V.2. Additional discussion about optical control of AFM
 - V.3. Additional discussion about previous works on MnBi_2Te_4
 - V.4. Additional discussion about thickness dependence

I. Addressing alternative origins for CD in even-layered MnBi_2Te_4

In this section, we carefully consider alternative origins for the observed CD beyond the optical Axion electrodynamics. We enumerate systematic experimental data and theoretical analyses, which allow us to show that these alternative origins are not significant for our experiments.

I.1. Protection layers (PMMA/hBN) induced CD

We covered hBN and PMMA (poly(methyl methacrylate)) layers on the MnBi_2Te_4 flakes to protect them from oxidation before taking them out of the glovebox (see Methods section). We can exclude the possibility that the observed CD signals come from these protection layers as follows:

- PMMA and hBN are non-magnetic. Reflection CD is strictly prohibited under \mathcal{T} (see proof in SI.III.3).
- As shown by the temperature-dependence and B -hysteresis measurements (Figs. 2 and 3 in the main text), our observed CD signal clearly arises from the AFM order in MnBi_2Te_4 .

I.2. Uncompensated magnetization induced magnetic CD

We now consider the possibility that the AFM is uncompensated with nonzero M , which leads to magnetic CD. In even-layered MnBi_2Te_4 , this uncompensated M could arise from sample degradation or a vertical E field. Because this has been carefully addressed in the main text, we only enumerate the key evidence.

- Most importantly, we observe $\text{RCD} \neq 0$ but $\text{TCD} = 0$. We emphasize that RCD and TCD were measured simultaneously, which means on the same spot of the same flake without changing any other condition (T , B field).
- The NV center magnetometry measurements show no observable M .
- The hBN-encapsulated 6SL MnBi_2Te_4 sample is expected to minimize the vertical E field. However, as shown in Extended Data Fig.5, the RCD still persists.
- Sample degradation is minimized because the entire device fabrication process was finished in an Ar-filled glovebox without exposure to air, chemicals, or heat. The optical CD data are

of high quality. Using a similar fabrication process, we have also fabricated a 6SL MnBi_2Te_4 device with electrical contacts and performed transport experiments in the same cryostat as the optical CD measurements. In the FM phase at $B = -7$ T, we observed clear topological Chern insulator state with fully quantized R_{yx} and zero R_{xx} (Fig. S35). The high data quality helps to rule out the degradation possibility.

Based on these systematic data, we conclude that the uncompensated magnetization induced magnetic CD is not the dominant effect in the even-layered MnBi_2Te_4 .

I.3. Light attenuation induced residual CD

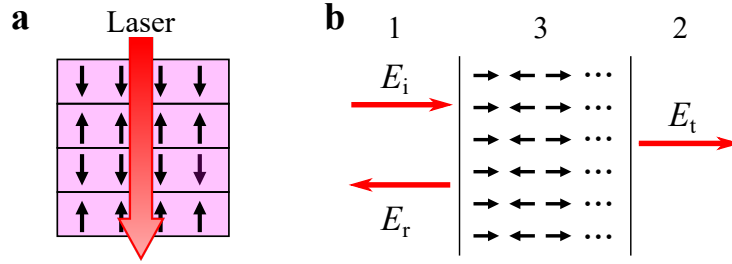


Fig. S1: **a**, Schematic illustration for the light attenuation induced residual CD. **b**, A layout to theoretically compute the light attenuation induced residual CD (see SI.I.3.2).

We now consider another important possibility based on the magnetic CD: The even-layered AFM is fully compensated, but the magnetic CD signals coming from opposite spin layers may not cancel, because the light intensity decays due to absorption (Fig. S1a). We refer to this mechanism as light attenuation induced residual CD.

I.3.1. Weak absorption in 2D MnBi_2Te_4 flakes

As shown in Fig. S2, the amplitude of the CD in 6SL is similar to that in 7SL. If we purely use the light attenuation induced residual CD mechanism to explain, then the result would only make sense in the very strong absorption limit. For instance, let us assume that the top layer absorbs all light. This means that the CD only probes the top layer, so the number of layers does not matter.

In sharp contrast, the actual absorption in 2D MnBi_2Te_4 is weak. Based on our direct measurements (Fig. S3), each MnBi_2Te_4 layer absorbs only $\sim 1.7\%$ light. This means that light probes the 2D MnBi_2Te_4 flake as a whole, rather than only the top layer. With a total absorbance of $\sim 10\%$

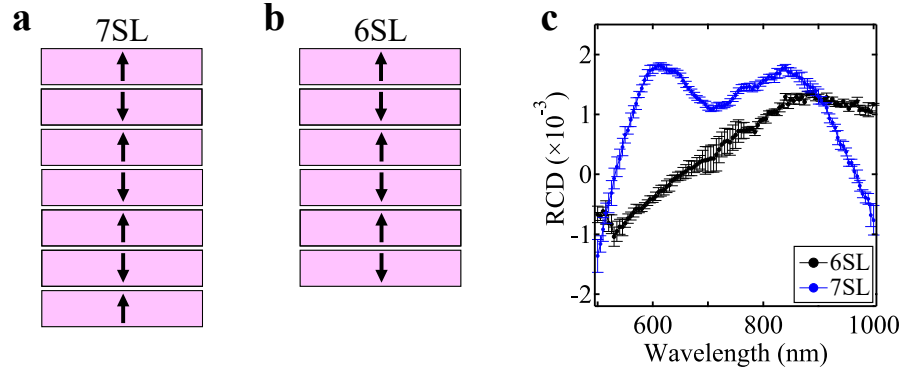


Fig. S2: Comparison between the RCD in 6SL and 7SL at $B = 0$.

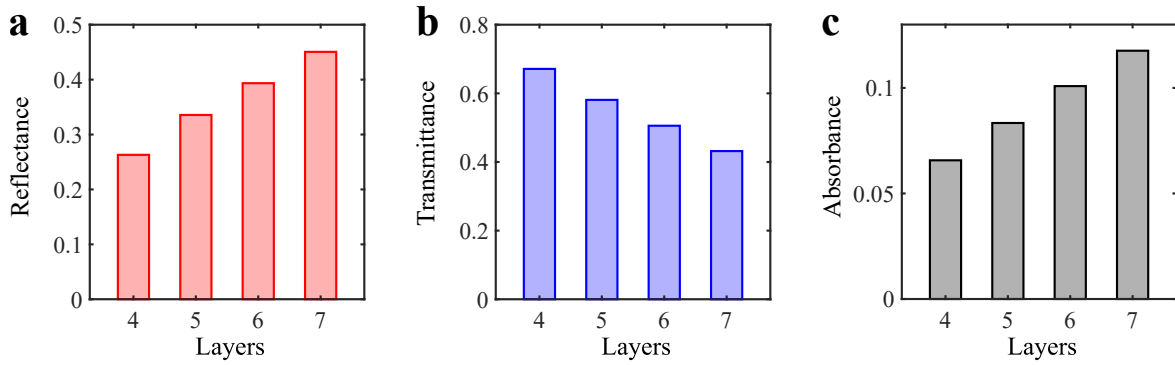


Fig. S3: Reflectance, transmittance and absorbance of 2D MnBi_2Te_4 flakes.

in 6SL or 7SL, it is highly unlikely that the residual CD in 6SL is similarly strong as the magnetic CD in 7SL.

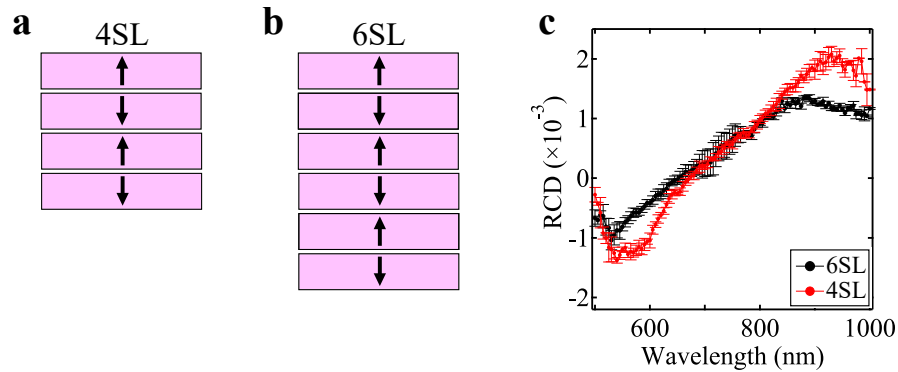


Fig. S4: Comparison between the RCD in 6SL and 4SL at $B = 0$.

We have further studied the CD in 4SL, which is found to be even stronger than 6SL (Fig. S4) but the total absorbance in 4SL is as low as $\sim 6\%$. These studies show that the light attenuation induced residual CD cannot explain our experiments.

Notes: We determined the absorbance of MnBi_2Te_4 in two independent ways. First, as shown in Fig. S3, we measured the reflectance and transmittance simultaneously in our 2D MnBi_2Te_4 flakes, and obtain the absorbance. Second, a recent FTIR experiment [1] measured the optical conductivity of bulk MnBi_2Te_4 , based on which we can obtain the light attenuation coefficient and therefore the averaged absorbance per layer. Both methods yield the consistent result, i.e., $\sim 1.7\%$ absorbance per layer.

I.3.3. Quantitative estimation of the light attenuation induced residual CD

To make our conclusion above more precise, we aim to quantitatively calculate the magnitude of the light attenuation induced residual CD. In fact, this attenuation induced residual CD effect has been theoretically derived in Ref. [2] by expanding the off-diagonal part of the dielectric tensor ϵ_{xy} to the first order in $\frac{d}{\lambda}$ (the interlayer distance $d \simeq 1$ nm) following the standard light scattering theory [3]. $\epsilon_{xy}(z) = \bar{\gamma}d \sum_{n=1}^{N-1} (-)^n \delta(z - nd)$, where $\bar{\gamma}$ represents the rotation power for a single FM layer and N is the number of layers. The \mathbf{E} field in the entire space can be obtained by solving the following equation: $(\epsilon \frac{4\pi^2}{\lambda^2} - \text{curl curl})\mathbf{E} = -\frac{4\pi^2}{\lambda^2} \epsilon_{xy}(z)\mathbf{E}_3$, where $\epsilon = \epsilon_{xx} = \epsilon_{yy}$ is the diagonal part of the dielectric tensor, \mathbf{E} and \mathbf{E}_3 are the electric fields outside and inside the AFM (see layout in Fig. S1b). This was solved in Ref. [2]. In the thin film limit (number of layer N is small), the magnetic CD and attenuation induced residual CD can be both expressed by the RCD of a single FM layer,

$$\text{Magnetic CD} = \frac{1}{N} \text{RCD}^{\text{1SL}} \quad N \text{ is odd} \quad (\text{S8})$$

$$= 0 \quad N \text{ is even} \quad (\text{S9})$$

$$\text{attenuation induced residual CD} = 2\pi \frac{d}{\lambda} \text{RCD}^{\text{1SL}} \quad \text{both odd and even} \quad (\text{S10})$$

We know that the magnetization M in odd layers is inversely proportional to the layer number N , and the M in even layers is zero. Indeed, from From Eqs. S8 and S9, we see that the magnetic CD behaves in the same way, consistent with the expectation that the magnetic CD is proportional to M . On the other hand, for the attenuation induced residual CD, we see that the relevant quantity is $\frac{d}{\lambda} \sim \frac{1}{1000}$ from Eq. S10, which is very small ($d \simeq 1$ nm and typical $\lambda = 1000$ nm). In fact, the factor of $\frac{d}{\lambda}$ can be intuitively derived by the following picture: as light propagates and attenuates, each spin layer feels a spatially varying electric field $E(z) = E_0 e^{ik_z z}$ (k_z is the light wave-vector). By considering the reflection from each spin layer, the ratio between attenuation

induced residual CD and $\text{RCD}^{1\text{SL}}$ can be estimated as $(1 - e^{2ik_z d} + e^{4ik_z d} - e^{6ik_z d} + \dots)/(1 + e^{2ik_z d} + e^{4ik_z d} + e^{6ik_z d} + \dots) \propto \frac{d}{\lambda}$. We could now estimate the attenuation induced residual CD based on our own experimental data. Using Eqs. S10 and S8, we can express the light attenuation induced residual CD by the measured magnetic CD in 7SL. By using $d = 1$, $\lambda = 1000$ nm, and $N = 7$, we obtain attenuation induced residual CD $\sim 4\%$ of the magnetic CD in 7SL. By contrast, our 6SL RCD experimental data is similarly large as 7SL (Fig. S2).

I.4. Higher order effects

We now explore the possibility of CD due to higher order effects in electromagnetic fields, which in general can arise from many microscopic mechanisms. However, a unifying property is that the CD amplitude due to higher order effects is expected to depend strongly on the optical power. To be more specific, let us consider the following mechanism as an example: The even-layered AFM is fully compensated, but light can generate a nonzero static M (e.g. the inverse Faraday effect), which in turn leads to a magnetic CD. In this case, the CD is expected to be proportional to the laser power. This is quite intuitive: Without light, the material has $M = 0$. Light induces M . As such, stronger light means larger light-induced M , which in turn results in stronger CD.

By contrast, the CD processes we considered in the main text are linear optical effects, i.e., the amplitude of CD is independent of the optical power. This can be understood by the fact that they are direct measures of the material's properties. For example, the Axion CD is proportional to the material's ME coupling; the magnetic CD is proportional to the material's M ; the natural optical activity is proportional to the material's spatial chirality. Therefore, their magnitude is independent of the optical power.

We have carefully studied how CD depends on the optical power. As shown in Fig. S7, our CD in both 5SL and 6SL MnBi_2Te_4 is clearly independent of optical power, therefore ruling out the possibility of higher order effects.

II. Additional data

II.1. Additional CD data

RCD magnetic hystereses at multiple wavelengths: To better understand the RCD signals of the MnBi_2Te_4 system, in Figs. S5a-p, we show the RCD magnetic hystereses for 5SL-8SL at multiple wavelengths, including 540 nm, 710nm, 840 nm and 946 nm. These data are all consistent with the RCD spectra shown in Figs. S5q-t.

Temperature dependence of RCD data: In order to highlight the nonzero RCD signal at $B = 0$, we define $\delta\text{RCD}(B) = \text{RCD}^{\text{Backward}}(B) - \text{RCD}^{\text{Forward}}(B)$ (Backward/Forward refer to the scanning direction of the magnetic hysteresis). Figures S6a,b show the T and B dependence of δRCD in 6SL, where the Axion CD near $B = 0$ is clearly observed. Figures S6c,d show the T and B dependence of δRCD in 5SL, where the magnetic CD near $B = 0$ is clearly observed.

Optical power dependence of the RCD data: As shown in Fig. S7, the RCD data for both 5SL and 6SL are independent of the detection optical power, which shows that both the magnetic CD and Axion CD are linear optical effects.

Additional TCD magnetic hysteresis and spectrum: In the main text, we showed that the TCD signals of 6SL MnBi_2Te_4 vanish at $B = 0$. To substantiate this conclusion, we measured TCD magnetic hystereses for 6SL at multiple wavelengths (540 nm, 800 nm, 840 nm and 900 nm, Fig. S8), which all show vanishing TCD signals at $B = 0$. On the other hand, we also measured TCD magnetic hystereses for 5SL at multiple wavelengths (800 nm, 840 nm and 900 nm, Fig. S9a-c), which further demonstrate that magnetic CD exists in transmission. Additionally, Fig. S9d shows the 5SL TCD spectrum, which is quite similar to the 5SL RCD spectrum shown in Fig. S5q.

Reproducibility of simultaneous TCD and RCD measurements: One of our most crucial observations is that the Axion CD only shows up in reflection but is absent in transmission (i.e., nonzero RCD but zero TCD). This conclusion was found to be highly reproducible. First, we performed measurements of 6SL flakes on different substrates (see Figs. S10b,e). Independent of the substrates, we found nonzero RCD but zero TCD. Second, on the same substrate, we

performed measurements on flakes with different thicknesses (6SL and 8SL, see Figs. S10e,h). For both 6SL and 8SL, we found nonzero RCD but zero TCD. These systematic results further demonstrate the unique transmission and reflection properties of Axion CD.

RCD signal in hBN-encapsulated MnBi_2Te_4 sample: In the main text, we discussed the possibility of uncompensated magnetization due to a built-in electric field induced by asymmetric dielectric environment, which is an alternative mechanism for our observed RCD signal. To further rule out this possibility, here we show the RCD signals measured in a hBN-encapsulated sample (S4). The hBN-encapsulated sample is supposed to give minimal built-in electric field. As shown in Fig. S11, the RCD hysteresis and spectra of hBN-encapsulated sample is very similar to that of sample-S3, which has diamond on bottom and hBN on top. This is contradictory to the possibility of built-in electric field induced magnetization.

Reproducibility of Axion CD on different substrates: In Fig. S12, we summarize all samples mentioned in the main text, which are on different substrates (diamond, sapphire and hBN). Despite the different substrates, all 6SL flakes show highly reproducible Axion CD signals (Figs. S12b,e,h,k). Furthermore, their RCD spectra are quite similar in terms of both amplitude and shape (Figs. S12c,f,i,l). The small variation of the RCD amplitude could come from the different substrate refractive indices. In conclusion, Axion CD is robust and reproducible, and does not rely on a specific type of substrate.

Thickness dependence of RCD: Figure S13a shows the measured RCD for 4, 6, 8, 10 SLs and thick samples. RCD were observed in all thicknesses. From our data, we see that the RCD is slightly weaker with increasing thickness and remains finite in the very thick limit. Theoretically, we have computed the RCD for 2, 4, 6 SLs based on DFT band structures. As shown in Fig. S13b, the calculated RCD are similarly large. For larger thickness than 6SL, the DFT calculations become too heavy to run. Using a simple tight-binding (TB) effective model [4], we can simulate up to 50SL (Fig. S13c), which shows that the Kerr effect indeed persists. But we caution that band structures of this TB effective model may not be able to capture the realistic MnBi_2Te_4 band structure, especially for the high energy states. Nevertheless, the purpose of TB model is to show that optical Axion electrodynamics persists in thick samples.

Consistent sign of the CD: In order to check if the sign of the CD is consistent every

time we turn on the PEM, we have performed the following testing: (1) We measured the CD value of an MnBi_2Te_4 sample, (2) We turned off the PEM and turned it back on, (3) We redid the same measurement. We repeated the above steps many times. As shown in Fig. S14b, for every measurement, the sign of the CD (the phase of the lock-in) is invariant. We explain this based on the PEM+lock-in setup shown in Fig. S14a. The PEM output reference wave (also reference for lock-in) definitively corresponds to the σ^+ and σ^- polarizations. This is because the PEM reference wave is synchronized with the piezoelectric voltage, which is used to control the retardation of the optical head.

Background removal for CD: It is well-known that beam splitter when used at $\sim 45^\circ$ can lead to significant CD offset. In order to minimize the unwanted background, we used a plate beam splitter at near-normal incidence. To check our background level, we measure CD both on the sample (Fig. S15b), and next to the sample (Fig. S15a). We see that the background is in general ~ 5 times smaller than the signal. We therefore remove the background from the signal by subtracting Fig. S15b with Fig. S15a.

RCD signal of Cr_2O_3 single crystal: In order to substantiate the broad applicability of Axion optical induction, we also measured the RCD signal of Cr_2O_3 (shown in S16). The RCD signal of Cr_2O_3 is consistent with previous pioneering work by Krichevtsov et al[5].

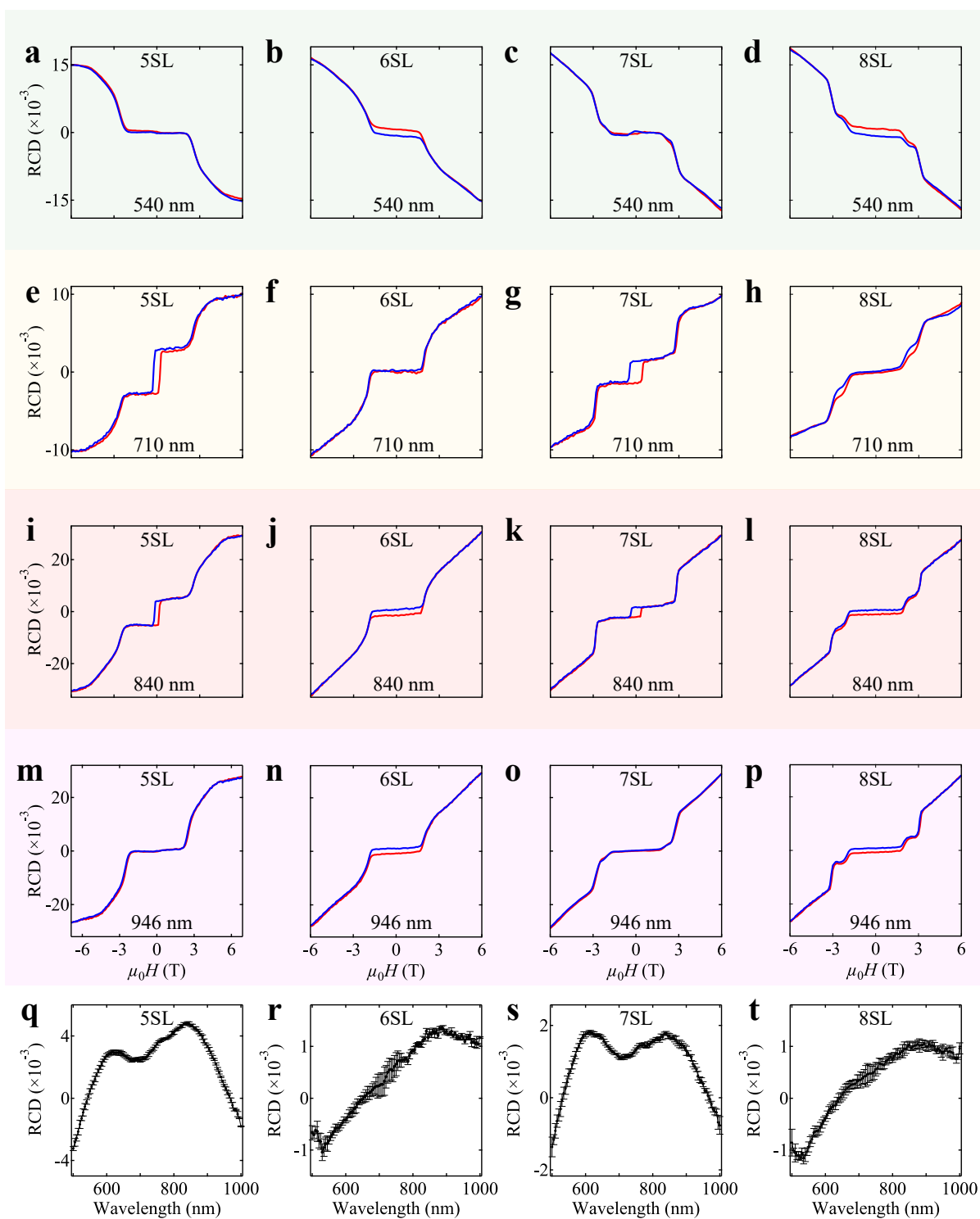


Fig. S5: **a-p**, Magnetic hystereses of RCD for 5SL, 6SL, 7SL and 8SL measured using different wavelengths. **q-t**, RCD spectra for 5SL, 6SL, 7SL and 8SL.

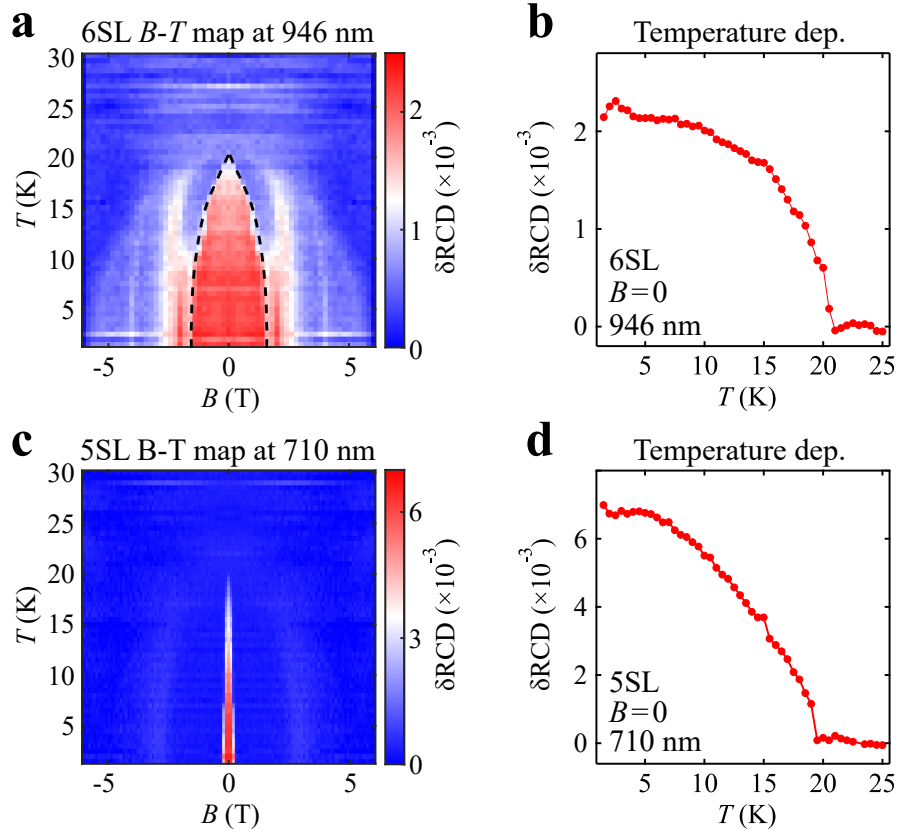


Fig. S6: $\delta\text{RCD}(B) = \text{RCD}^{\text{Backward}}(B) - \text{RCD}^{\text{Forward}}(B)$. **a,b,** Temperature T and magnetic field B dependence of δRCD in 6SL at $\lambda_{\text{detection}} = 946$ nm. The Axion CD near $B = 0$ is clearly observed. **c,d,** Same as panels (**a,b**) but for 5SL at $\lambda_{\text{detection}} = 710$ nm. The magnetic CD near $B = 0$ is clearly observed.

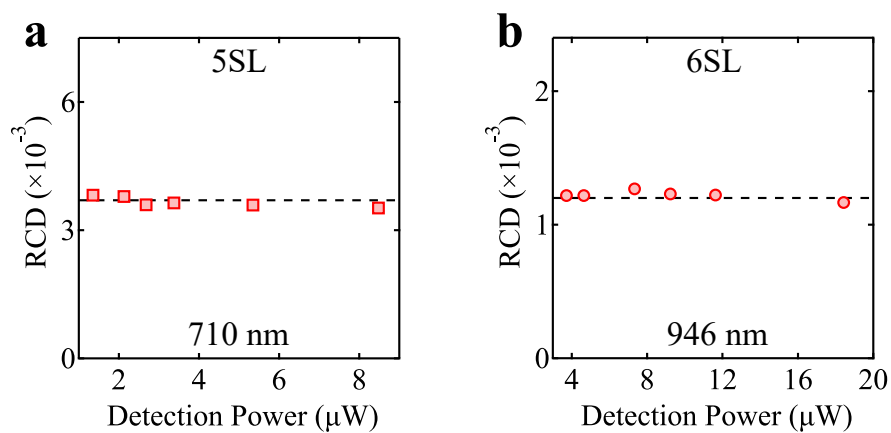


Fig. S7: **a**, Optical power dependence of the 5SL RCD signal ($\lambda_{\text{detection}} = 710 \text{ nm}$). **b**, Detection power dependence of the 6SL RCD signal ($\lambda_{\text{detection}} = 946 \text{ nm}$).

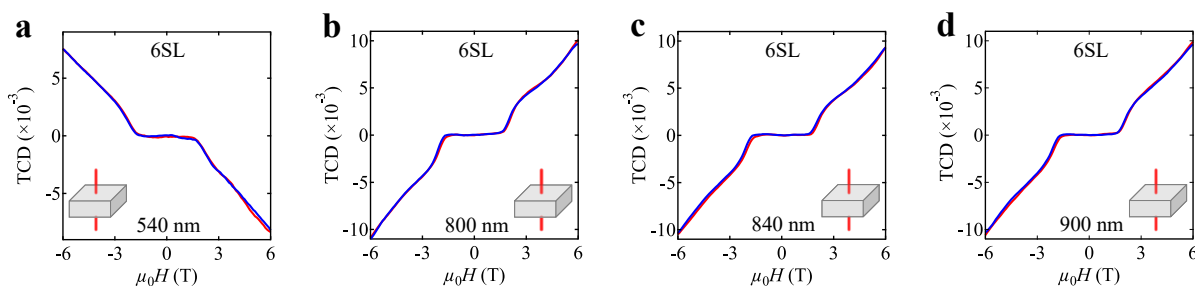


Fig. S8: **a-d**, Magnetic hystereses of TCD for 6SL measured at 540 nm, 800 nm, 840 nm and 900 nm.

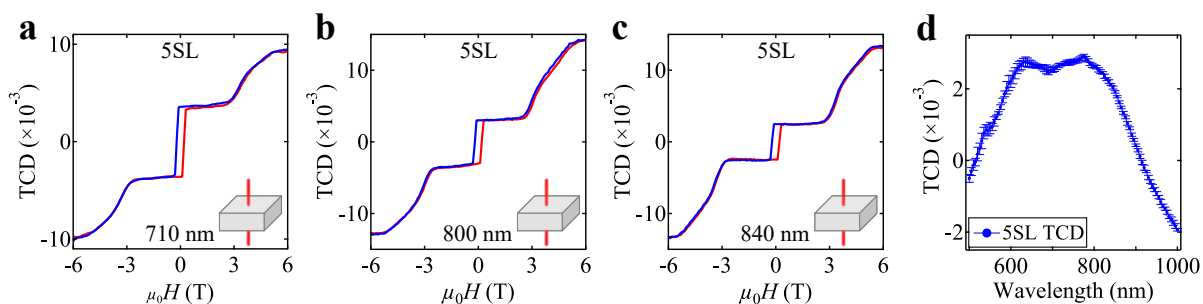


Fig. S9: **a-c**, Magnetic hystereses of TCD for 5SL measured at 710 nm, 800 nm and 840 nm. **d**, TCD spectrum at $B = 0$ for 5SL.

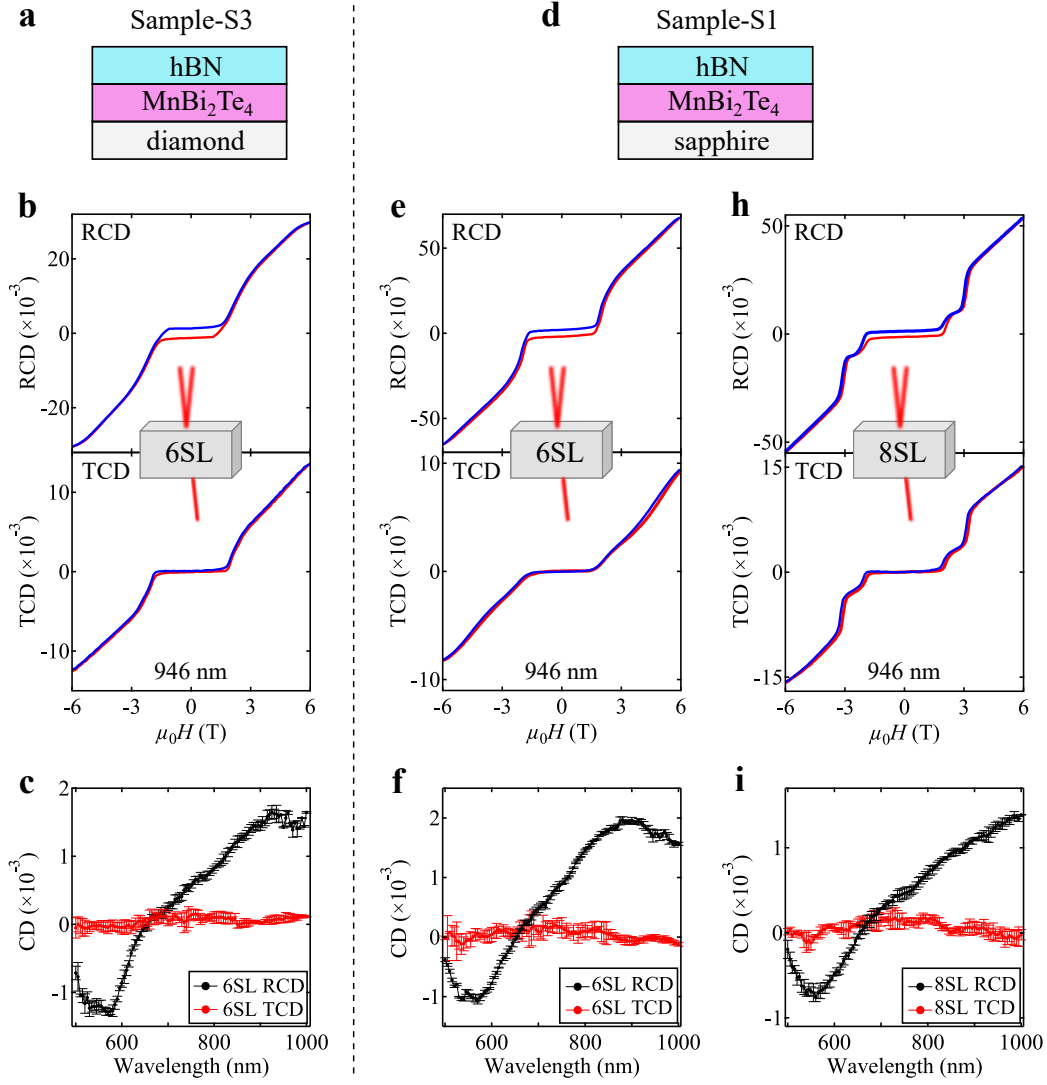


Fig. S10: Simultaneous RCD and TCD measurements in both samples-S3 and S1. **a-c**, Sample schematic (panel **a**), simultaneous RCD and TCD magnetic hystereses using $\lambda_{\text{detection}} = 946$ nm (panel **b**), and RCD and TCD spectra at $B = 0$ (panel **c**) for the 6SL flake of sample-S3 on diamond substrate. **d-i** Same as panels **a-c** but for the 6SL and 8SL flakes of sample-S1 on sapphire substrate.

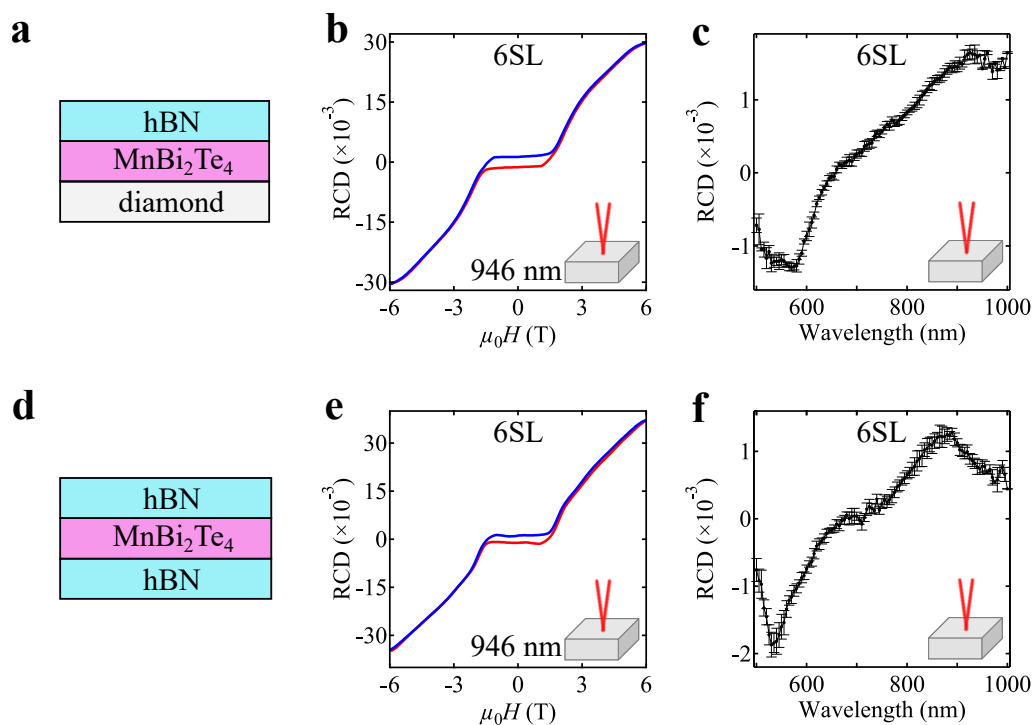


Fig. S11: Comparison between sample-S2 on diamond and sample-S4 encapsulated by hBN. **a-c**, For the sample-S2 on diamond substrate. **a**, Sample schematic, **b**, RCD magnetic hysteresis at 946 nm, **c**, RCD spectrum at $B = 0$. **d-f**, Same as panels (**a-c**) but for sample-S4 encapsulated by hBN.

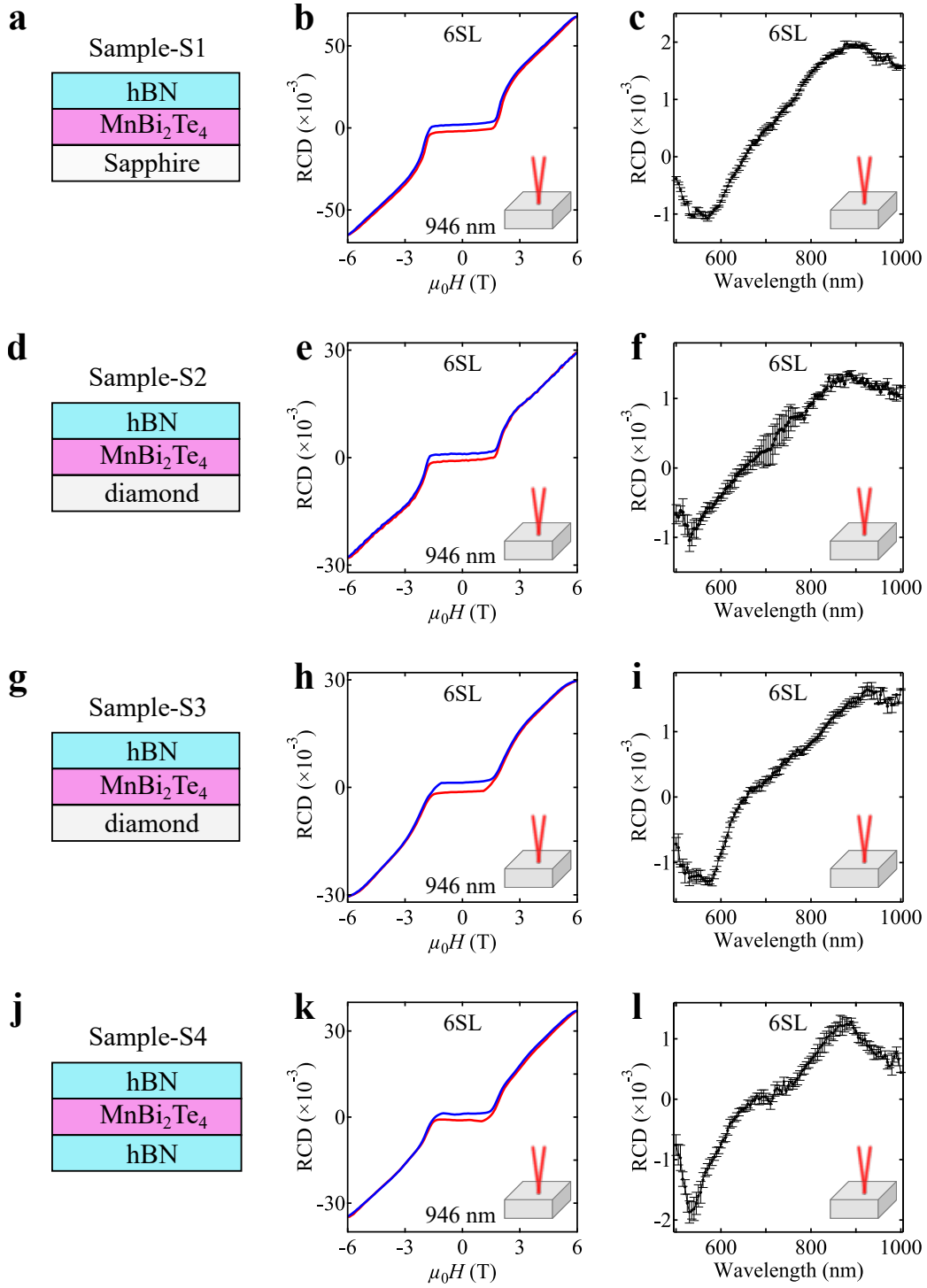


Fig. S12: Reproducible observations of the Axion CD in multiple samples on different substrates. **a-c**, Sample schematic (panel **a**), RCD magnetic hysteresis using $\lambda_{\text{detection}} = 946$ nm (panel **b**), and RCD spectrum at $B = 0$ (panel **c**) for Sample-S1. Similar results for sample-S2 (panels **d-f**), sample-S3 (panels **g-i**) and sample-S4 (panels **j-l**).

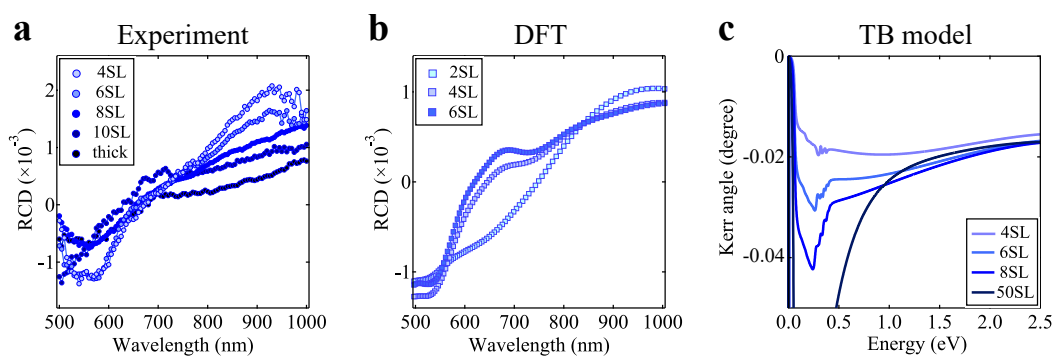


Fig. S13: **a**, Measured RCD data. **b**, Calculated RCD based on DFT band structures. **c**, Calculated complex Kerr angle based on an effective tight-binding model described in Ref. [4].

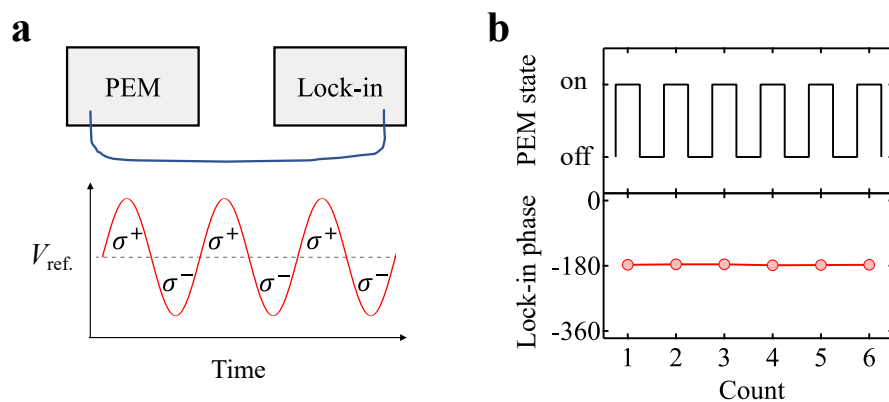


Fig. S14: **a**, PEM+lock-in setup. The PEM reference wave has definitive correspondence with σ^+ and σ^- polarizations. **b**, We parked the beam on a particular spot on an 8SL sample. We turned the PEM off multiple times and measure the lock-in phase (the sign of the CD) every time we turn the PEM back on.

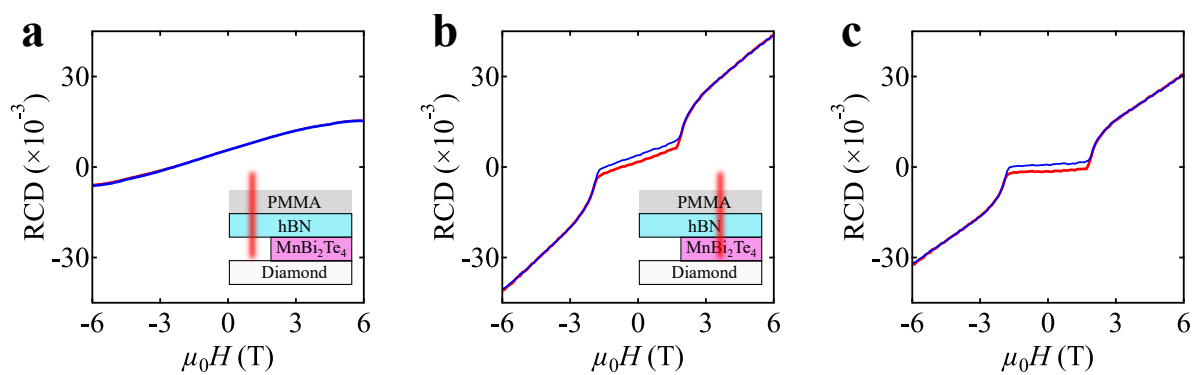


Fig. S15: **a,b**, Raw CD data when the beam spot is parked on the MnBi₂Te₄ flake (**b**) or next to the flake (**a**). **c**, CD after we subtract (**b**) by (**a**).

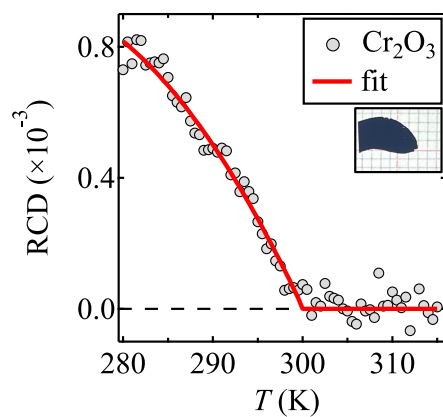


Fig. S16: RCD signal of Cr₂O₃ single crystal. Inset is the image of the Cr₂O₃ crystal (grid: 1 mm).

$\lambda_{\text{detection}} = 540 \text{ nm}$.

II.2. Additional induction data

Default experimental conditions: In order to systematically study the Axion induction, it is important to keep a consistent set of experimental conditions. In our experiments, we keep the following set of default experimental conditions: $\lambda_{\text{induction}} = 840$ nm, $P_{\text{induction}} \simeq 1$ mW; $\lambda_{\text{detection}} = 946$ nm and $P_{\text{detection}} \simeq 30$ μ W; induction initial and ending temperatures at 30 K and 2 K. When we try to study how the induction depends on a specific parameter, we keep all the other parameters at their default condition and only vary that specific parameter.

General remarks about the induction experiments: In our optical experiments (both induction and CD), light is focused to a spot of the diffraction limit (~ 1 μ m). For the areas that are chosen for induction (see Fig. S18), we have carefully studied their RCD signals as a function of B -field (by measuring magnetic hysteresis at 2 K) and T (upon multiple cooldowns without induction light). We found that after cooling down from 30 K to 2 K without induction, the RCD always reaches the maximal amplitude; only the sign is random (shown in Fig. S17). This suggests that, at least on the length scale of diffraction limit (~ 1 μ m), the areas chosen for induction are always in a single-domained state. Therefore, the results of induction are ternary: (1) the induction leads to the AFM state I (positive RCD at $\lambda_{\text{detection}} = 946$ nm); (2) the induction leads to the AFM state II (negative RCD at $\lambda_{\text{detection}} = 946$ nm); (3) the induction cannot favor one state, so the results are random just like no induction.

The induction ability: To characterize these different induction results, we define the quantity of induction ability. We define the RCD after induction from 30 K to 2 K with $\lambda_{\text{induction}} = 840$ nm and $P_{\text{induction}} = 1$ mW as the reference RCD (RCD^{ref}). We can then perform induction at other conditions and measure RCD. The induction ability is the ratio between the measured RCD and the reference RCD. Induction ability = $\frac{\text{RCD}}{\text{RCD}^{\text{ref}}}$. Therefore, if the induction leads to the same AFM state as the reference induction, then the induction ability will be $\simeq +1$; if the induction leads to the opposite AFM state as the reference induction, then the induction ability will be $\simeq -1$. If the induction has no effect, then we perform the induction 6 consecutive inductions and take the averaged RCD value, and the induction ability will be $\simeq 0$.

Spatial reproducibility: To substantiate the Axion induction, we have performed induction experiments at multiple locations on the 8SL MnBi_2Te_4 flake (sample-S1), which gave consistent results (shown in Fig S18).

Induction wavelength dependence: In addition to the induction wavelength dependence

data in the main text, Fig. S19 shows additional RCD spatial maps and temperature dependence data at multiple induction wavelengths ($\lambda_{\text{induction}} = 540 \text{ nm}, 580 \text{ nm}, 740 \text{ nm}, 840 \text{ nm}$ and 946 nm).

Induction power dependence: We investigate how induction depends on the optical power of the induction light. As shown in Fig. S21, we found that, for $P_{\text{induction}} \gtrsim 400 \mu\text{W}$, the induction can effectively control the AFM state. Below this power, the induction was found to show no effect, possibly due to the influence of defects and disorder.

Laser heating effect: It is important to characterize the effect of laser heating both in the induction and the CD detection processes (we use the same light source for induction and CD). In order to do so, we measured the temperature dependence of RCD while warming up at multiple laser powers, as shown in Fig. S22a. We focus on the temperature at which the RCD signal vanishes (defined as T^*). Without laser heating, $T^* = T_{\text{N}}$. Laser heating will manifest as a decrease of T^* (See detailed explanation in the caption of Fig. S22). As shown in Fig. S22b, at $P_{\text{detection}} = 1 \text{ mW}$, T^* decreases by $\simeq 2 \text{ K}$, indicating that laser heating caused a 2 K temperature increase locally at the sample. Therefore, we can draw the following conclusions about laser heating effect.

(1) For all RCD measurements, we consistently use $P_{\text{detection}} = 30 \mu\text{W}$. So laser heating during RCD measurements is minimal.

(2) For the optical induction, we consistently use $P_{\text{induction}} = 1 \text{ mW}$. So laser heating caused the sample temperature to increase by $\sim 2 \text{ K}$. In our typical induction process, we start to shine the induction light at 30 K and turn off the induction light at 2 K. Therefore, this small temperature increase is unimportant for our induction.

Magnetic hysteresis after optical induction: To further substantiate the Axion induction, we measure the magnetic hysteresis of the RCD after performing optical induction. As shown in Fig. S20, after induction with opposite helicity, the RCD is found to start from opposite branches of the magnetic hysteresis. This further confirms that induction with opposite helicity leads to opposite AFM states at low temperatures.

RCD spectra after optical induction: Figure S23 shows the RCD spectra after optical induction. The RCD spectra are opposite if we performed optical induction with opposite light helicity or different induction wavelengths (840 nm vs. 540 nm).

Induction initial temperature and ending temperature: The novel coupling between circular light and the Axion insulator state allows us to lift the energy degeneracy between the opposite AFM states. In order to actually choose one AFM state over the other, we need to further overcome the potential barrier between the opposite AFM states. In the vicinity of the Néel

temperature, the potential barrier is small, allowing us to achieve the control. For all induction experiments in the main text, the induction initial and ending temperatures were kept at 30 K and 2 K.

We now investigated how the induction initial and ending temperatures influence the induction result. First, we keep the ending temperature at 2 K while varying the initial temperature. As shown in Fig. S24a, for initial temperature higher than 23 K, the induction can effectively control the AFM state; by contrast, for initial temperature below 23 K, the induction ability approaches zero, suggesting that the potential barrier between opposite AFM states at low temperature is too strong to overcome. Second, we keep the initial temperature at 30 K while varying the ending temperature. As shown in Fig S24b and Fig S25, for ending temperature lower than 23 K, the induction can effectively control the AFM state.

Induction of 6SL: In Fig. S26, we show the induction results of 6SL sample.

Induction of 5SL: In Figs. S27a,b, we show the induction results of 5SL sample. Because odd-layered samples has an obvious M (like a ferromagnet), the primary interaction is between M and circularly-polarized light (confirmed by our simultaneous RCD TCD measurements in 5SL Figs. S27c,d). Therefore, the induction of odd-layered sample arises from the helicity-dependent optical control of M , which has been demonstrated previously in a range of ferromagnets.

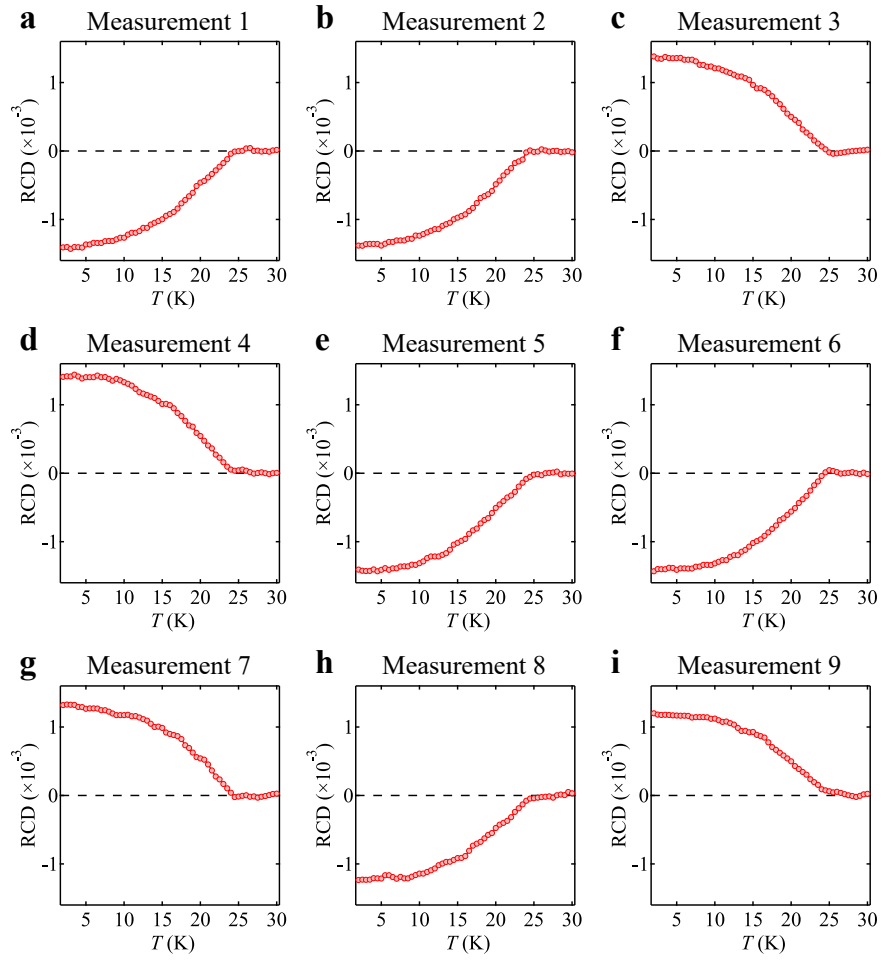


Fig. S17: Consecutive temperature dependent RCD measurements without induction of 8SL MnBi_2Te_4 in sample-S1 measured at $\lambda_{\text{detection}} = 946$ nm. These measurements show that cooling down without induction leads to a single-domained state, but the sign is random.

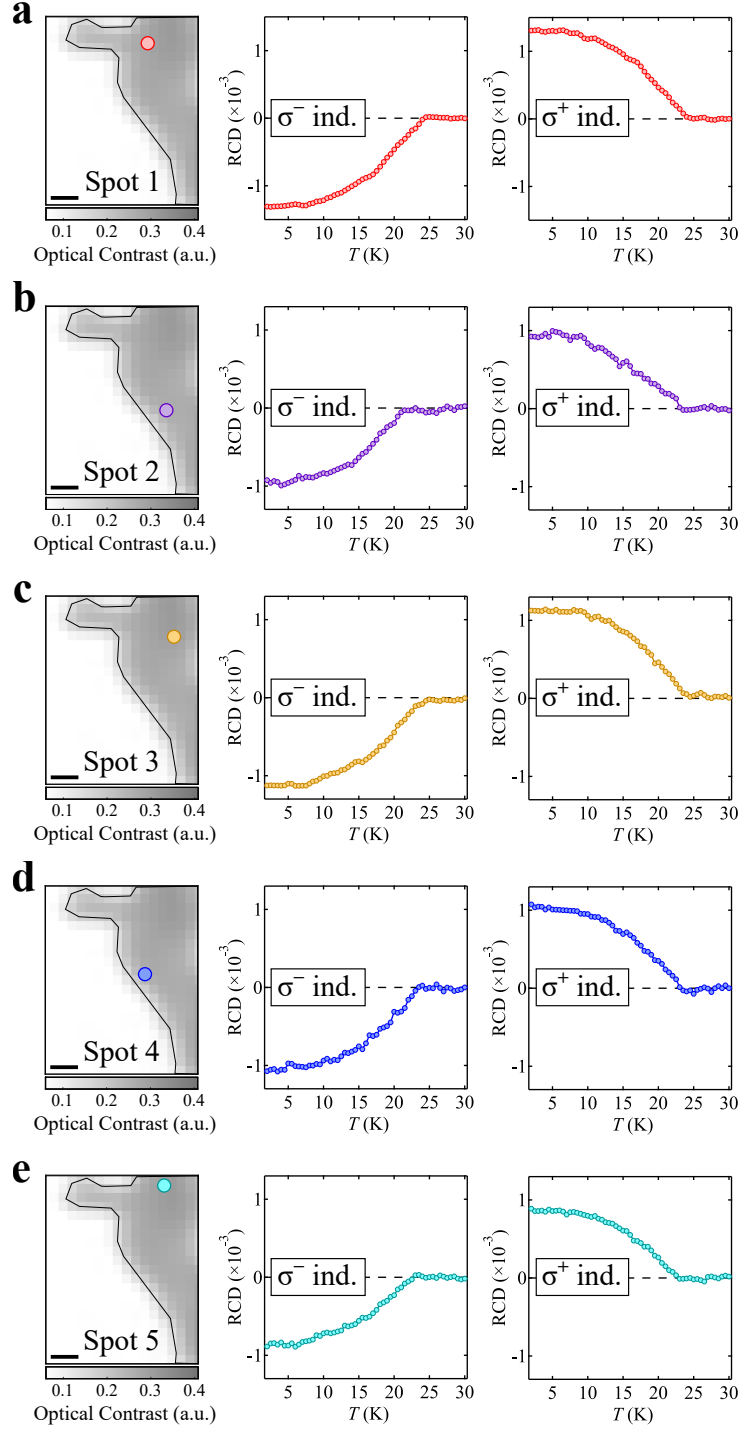


Fig. S18: Spatial reproducibility of the Axion induction. **a**, On the left is the optical contrast map of the 8SL MnBi₂Te₄ flake in sample-S1. The red dot marks the laser spot for induction experiments. On the right is the RCD signal as a function of temperature while warming up after induction with σ^\pm light. Scale bar: 2 μm . **b-e**, Same as panel (a) but at different spatial locations of the sample. Experimental parameters for data in this figure: $\lambda_{\text{induction}} = 840 \text{ nm}$, $P_{\text{induction}} \simeq 1 \text{ mW}$; $\lambda_{\text{detection}} = 946 \text{ nm}$, $P_{\text{detection}} \simeq 30 \mu\text{W}$.

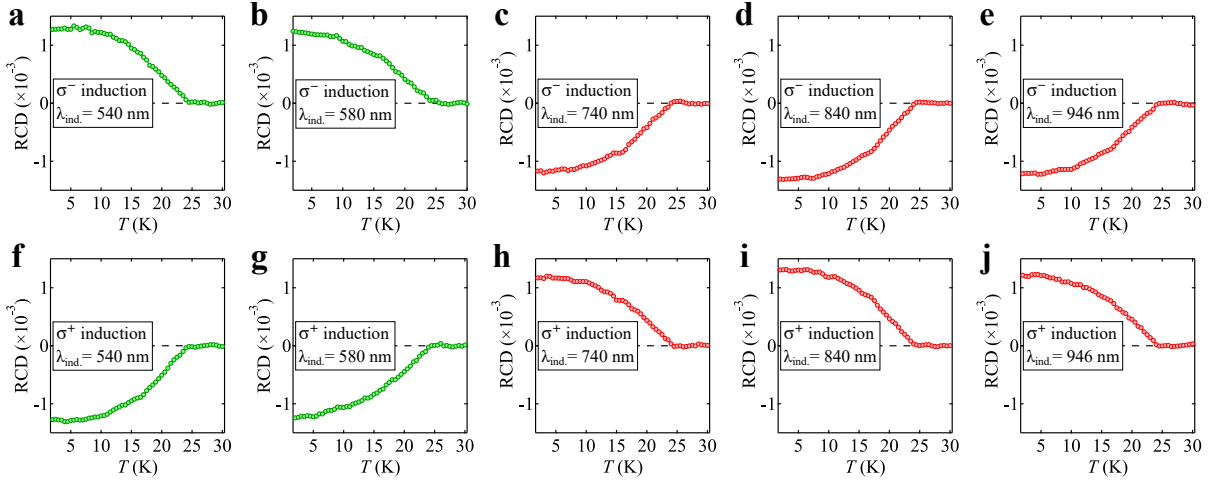


Fig. S19: Detailed results of Axion induction at multiple wavelengths. **a**, On the left is the RCD map at a particular area after induction ($\lambda_{\text{induction}} = 540 \text{ nm}$) with opposite helicity. The circle marks the laser spot for the induction light. On the right is the RCD signal as a function of temperature while warming up after induction with σ^{\pm} light. Scale bar: $2 \mu\text{m}$. **b-e**, Same as panel **(a)** but with the $\lambda_{\text{induction}}$ being 580 nm, 740 nm, 840 nm and 946 nm. Experimental parameters for data in this figure: $\lambda_{\text{induction}}$ noted in the figure, $P_{\text{induction}} \simeq 1 \text{ mW}$; $\lambda_{\text{detection}} = 946 \text{ nm}$, $P_{\text{detection}} \simeq 30 \mu\text{W}$.

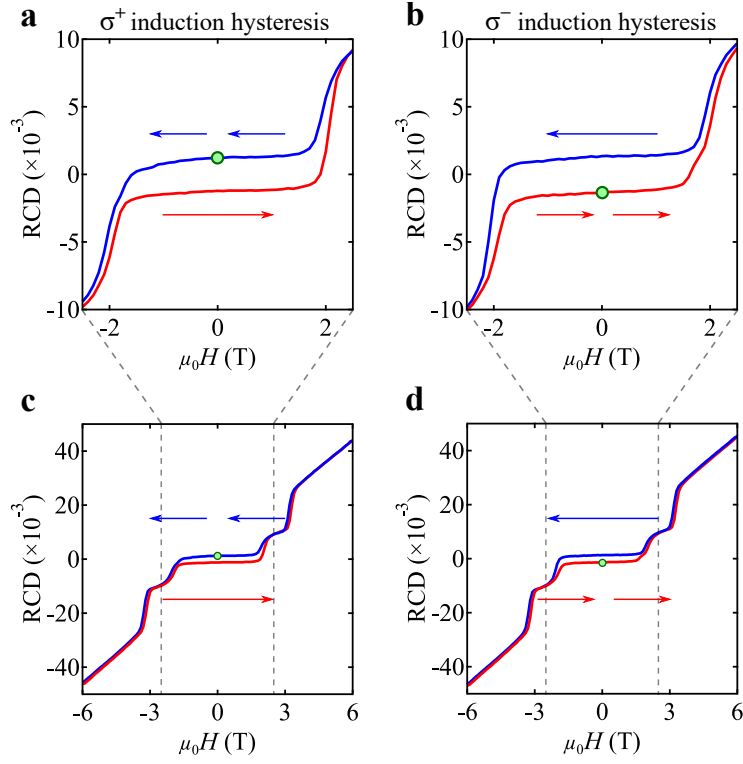


Fig. S20: a-d, Magnetic hysteresis of RCD after induction with opposite helicity in 8SL MnBi_2Te_4 of sample-S1. The starting points at $B = 0$ (green dots in panels **(a,b)**) are clearly on opposite hysteresis branch, again showing that the opposite induction helicity leads to opposite AFM domains. Experimental parameters for data in this figure: $\lambda_{\text{induction}} = 840 \text{ nm}$, $P_{\text{induction}} \simeq 1 \text{ mW}$; $\lambda_{\text{detection}} = 946 \text{ nm}$, $P_{\text{detection}} \simeq 30 \mu\text{W}$.

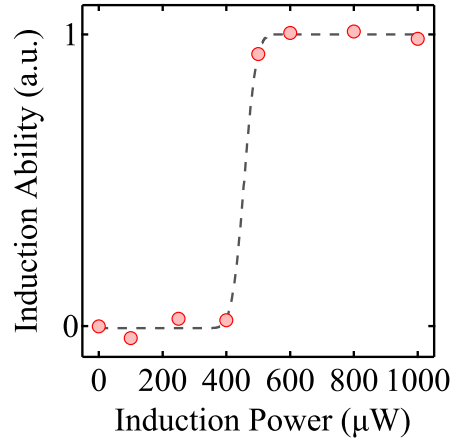


Fig. S21: Induction ability (see definition in the text SI.II.2) as a function of induction optical power. Experimental parameters for data in this figure: $\lambda_{\text{induction}} = 840 \text{ nm}$; $\lambda_{\text{detection}} = 946 \text{ nm}$. $P_{\text{detection}} = 30 \mu\text{W}$. The induction power is noted in the figure.

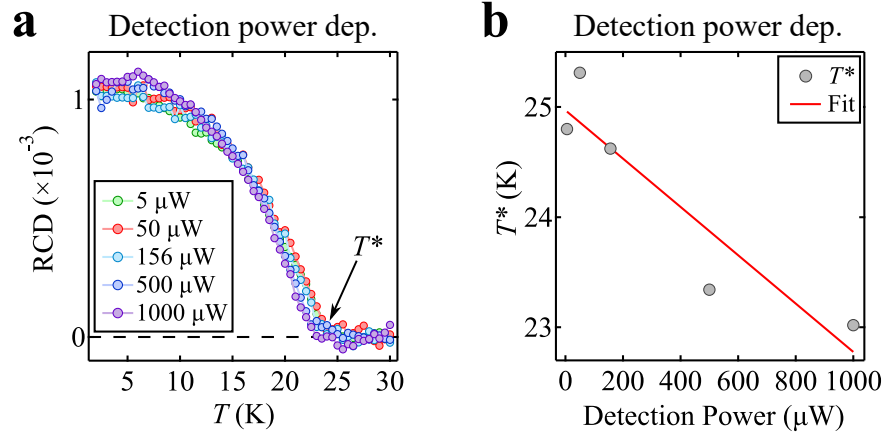


Fig. S22: **a**, RCD as a function of T measured while warming up at different optical powers. Note that T is the temperature of sample holder. In the presence of laser heating, when the sample reaches the Néel temperature T_N (i.e., when RCD signal vanishes), the sample holder temperature T^* is lower than T_N . Therefore, the difference between T^* and T_N is a measure of the laser-heating-induced temperature increase. **b**, T^* as a function of the optical power. T^* decreases with increasing $P_{\text{detection}}$. At $P_{\text{detection}} = 1$ mW, T^* decreases by $\simeq 2$ K, indicating that laser heating caused a 2 K temperature increase locally at the sample. $\lambda_{\text{detection}} = 840$ nm.

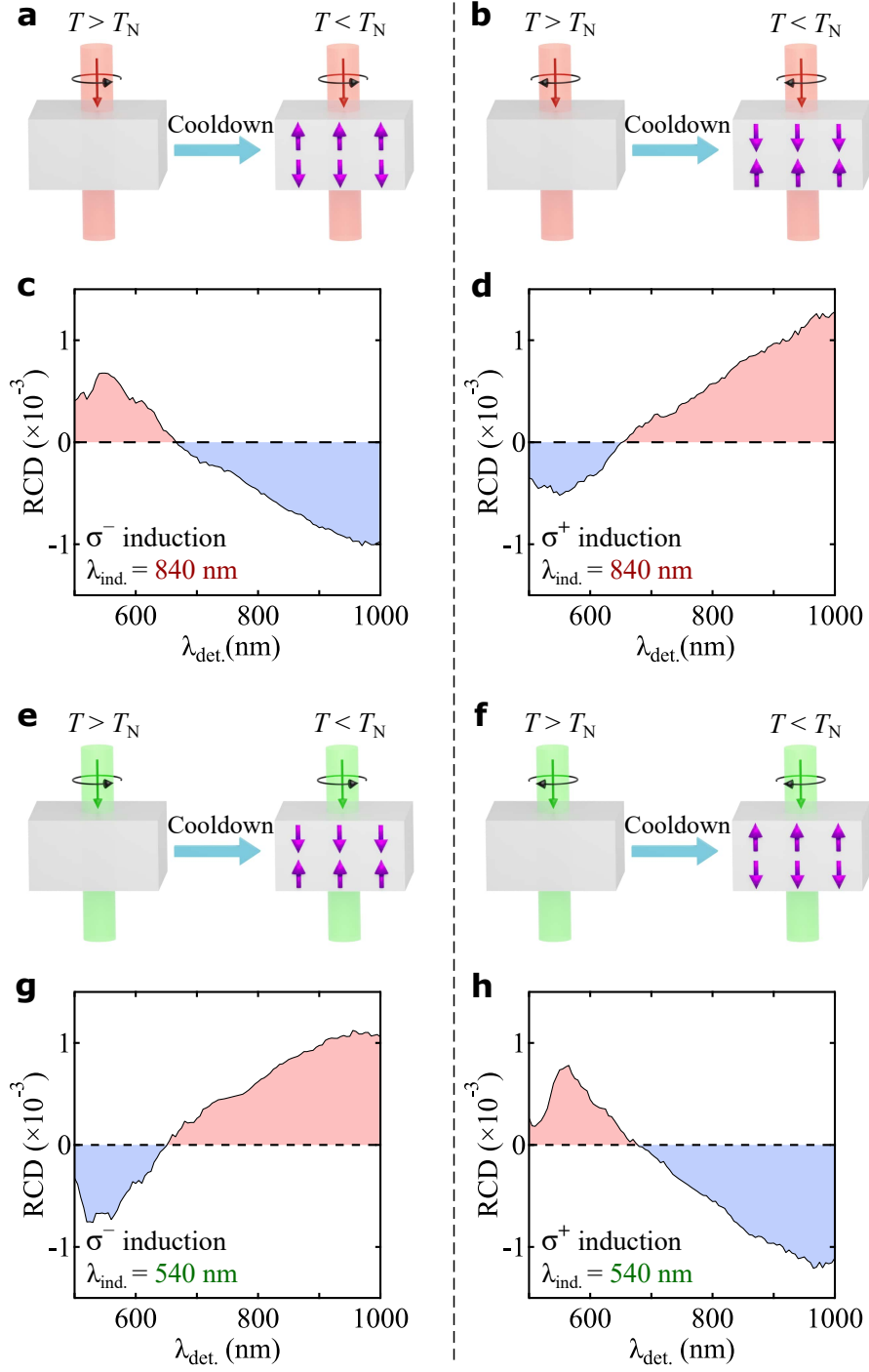


Fig. S23: RCD spectra after induction. **a,c**, We shine σ^- induction light ($\lambda_{\text{induction}} = 840 \text{ nm}$, $P_{\text{induction}} \simeq 1 \text{ mW}$) on the 8SL MnBi_2Te_4 flake (sample-S1) while lowering its temperature from $T = 30 \text{ K}$ to 2 K (panel **a**). Upon reaching 2 K , we turn off the induction light, and measure the RCD's spectra (panel **c**) at 2 K . **b,d**, Same as panels (**a,c**) except that we perform induction with σ^+ . **e-h**, Same as panels (**a-d**) except that we change $\lambda_{\text{induction}}$ to $\lambda_{\text{induction}} = 540 \text{ nm}$.

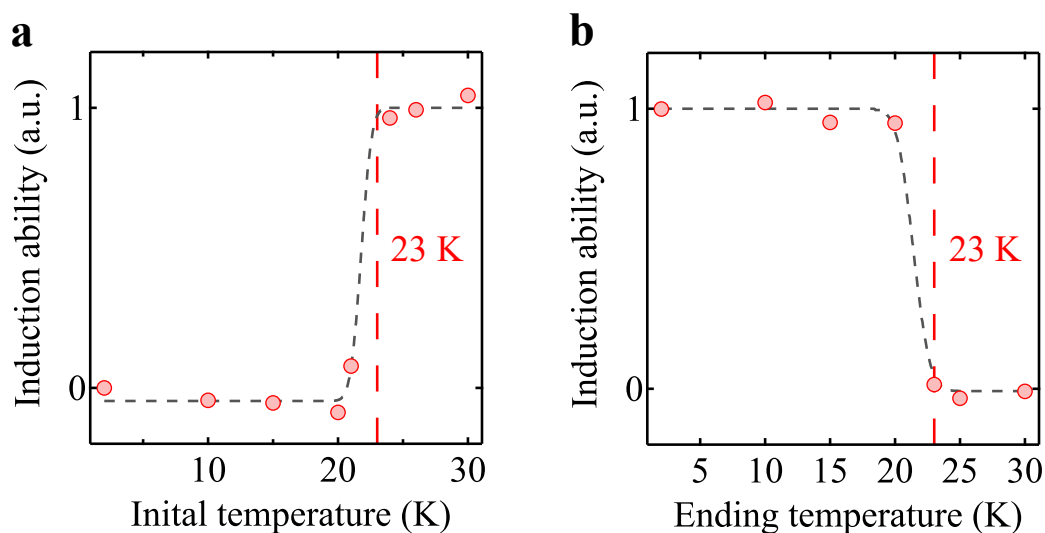


Fig. S24: Dependence of induction initial temperature and ending temperature. The initial (ending) temperature is the temperature at which we turn on (off) the induction light. **a**, We keep the ending temperature at 2 K and measure the induction ability as a function of the initial temperature. **b**, We keep the initial temperature at 30 K and measure the induction ability as a function of the ending temperature. Experimental parameters for data in this figure: $\lambda_{\text{induction}} = 840 \text{ nm}$, $P_{\text{induction}} \simeq 1 \text{ mW}$; $\lambda_{\text{detection}} = 946 \text{ nm}$, $P_{\text{detection}} \simeq 30 \text{ }\mu\text{W}$.

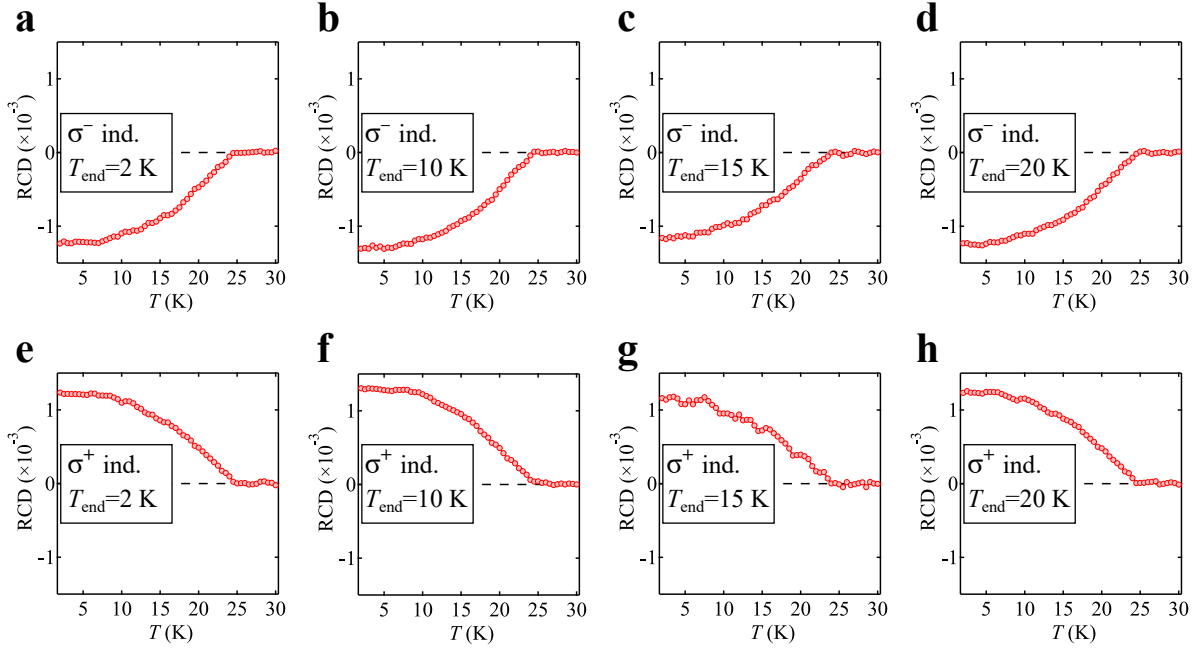


Fig. S25: **a-d**, We performed induction with σ^- helicity by keeping the initial temperature at 30 K and varying the ending temperature T_{end} . After induction, we cool the sample to 2 K. We then measure RCD as a function of temperature while warming up. **e-h**, Same as panels (**a-e**) but induction was performed with σ^+ helicity. This figure is in supplementary to Fig. S24b. Experimental parameters for data in this figure: $\lambda_{\text{induction}} = 840$ nm, $P_{\text{induction}} \simeq 1$ mW; $\lambda_{\text{detection}} = 946$ nm, $P_{\text{detection}} \simeq 30$ μ W.

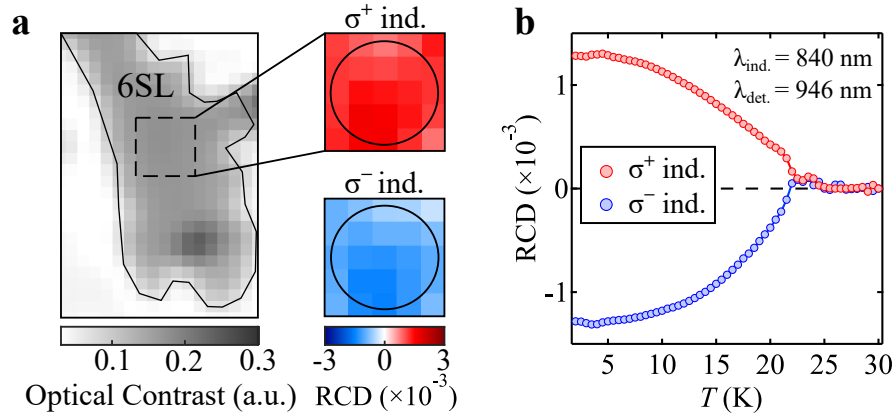


Fig. S26: **a**, Left: Optical contrast of the 6SL flake. Right: RCD upon induction using σ^\pm . **b**, Temperature-dependence of RCD after induction using σ^\pm .

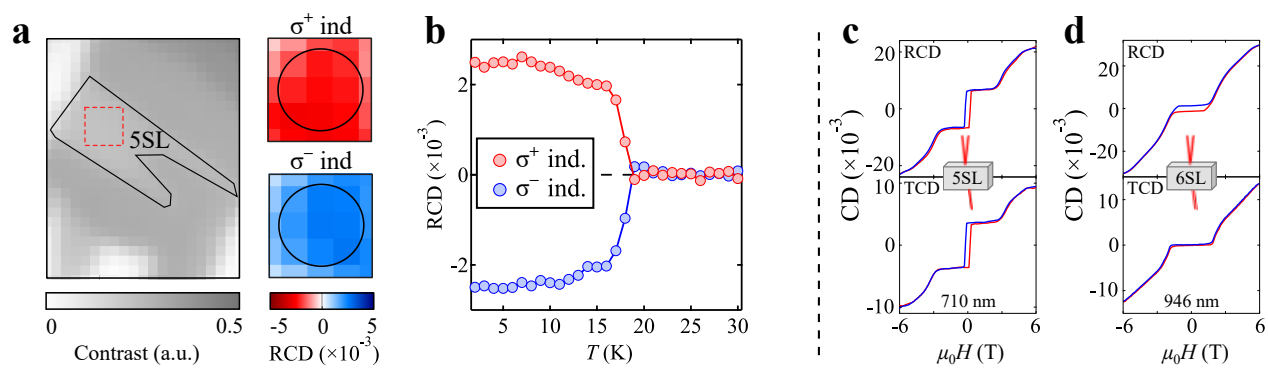


Fig. S27: **a**, Left: Optical contrast of the 5SL flake. Right: RCD upon induction using σ^\pm . **b**, Temperature-dependence of RCD after induction using σ^\pm . **c,d**, Simultaneous RCD TCD measurements for 5SL and 6SL.

II.3. Additional double induction data

Optical set-up for the double induction experiments: As shown in Fig. S28a, starting from a single beam, we constructed two collinear, spatially separated beams by the two beam splitters. Their polarizations were controlled separately by the combination of the half-waveplate and quarter-waveplate. Figures S28b-c show the optical contrast map and microscope image of double induction beams.

Single optical induction experiments on sample-S5: The double induction experiments were conducted on a new sample (S5). For consistency, we conducted single induction experiments as shown in Fig. S29. We observed consistent optical induction results as before, which provide the basis for the double induction experiments.

Detailed investigation into the AFM domain wall: In the main text, we showed that double induction beams with opposite helicity could create an AFM domain wall (also shown in Figs. S30a-d). Here, we scan a line-cut plot across the AFM domain wall (Figs. S30e-f). In contrast to both domains, the domain wall itself showed zero RCD signal, consistent with either Néel type or Bloch type AFM domain walls. In Figs. S30g-h, the temperature dependence of the RCD line-cut further supports our conclusion.

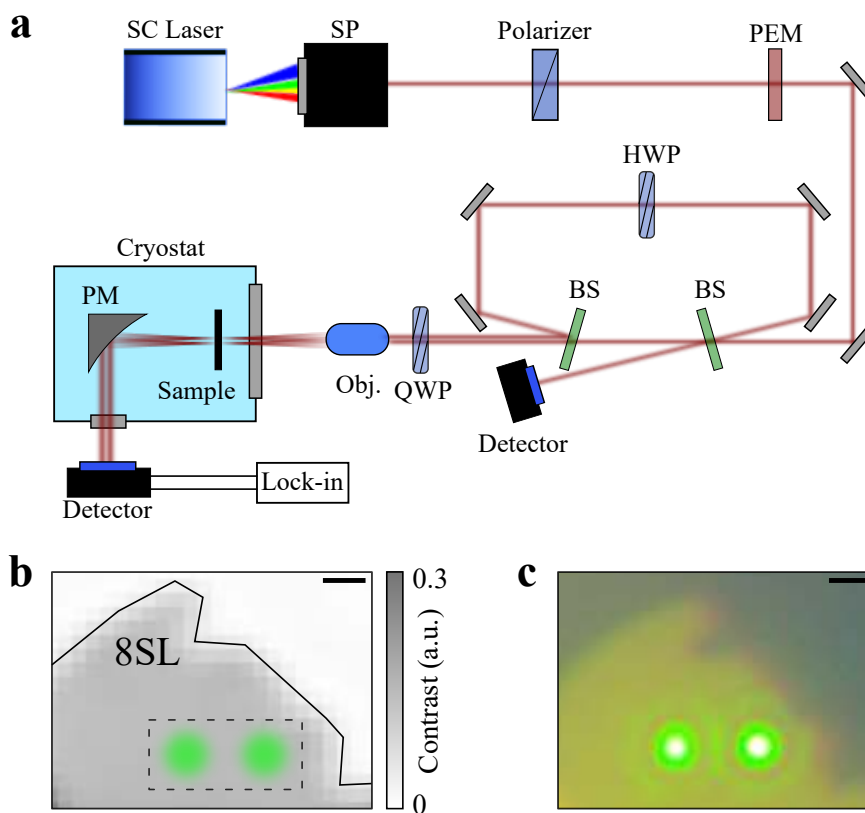


Fig. S28: **a**, Schematic drawing of optical set-up for double induction experiments. SC Laser: supercontinuum Laser, SP: spectrometer, BS: beamsplitter, HWP: half-waveplate, QWP: quarter-waveplate, Obj: Objective, PM: parabolic mirror. **b**, Optical contrast of the 8SL flake. **c**, Microscope image of the 8SL flake with double induction beams. Scale bar: $2 \mu\text{m}$.

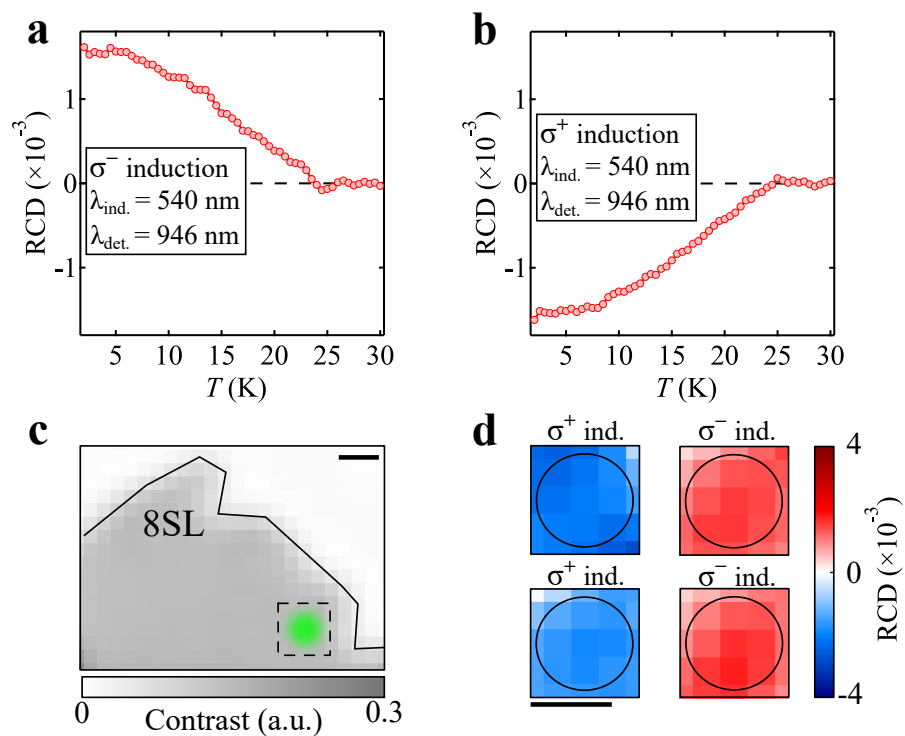


Fig. S29: **a,b**, Temperature dependence of RCD after induction using σ^\pm (with $\lambda_{\text{induction}} = 540$ nm). **c**, Optical contrast of the 8SL flake. **d**, RCD map upon induction using σ^\pm .

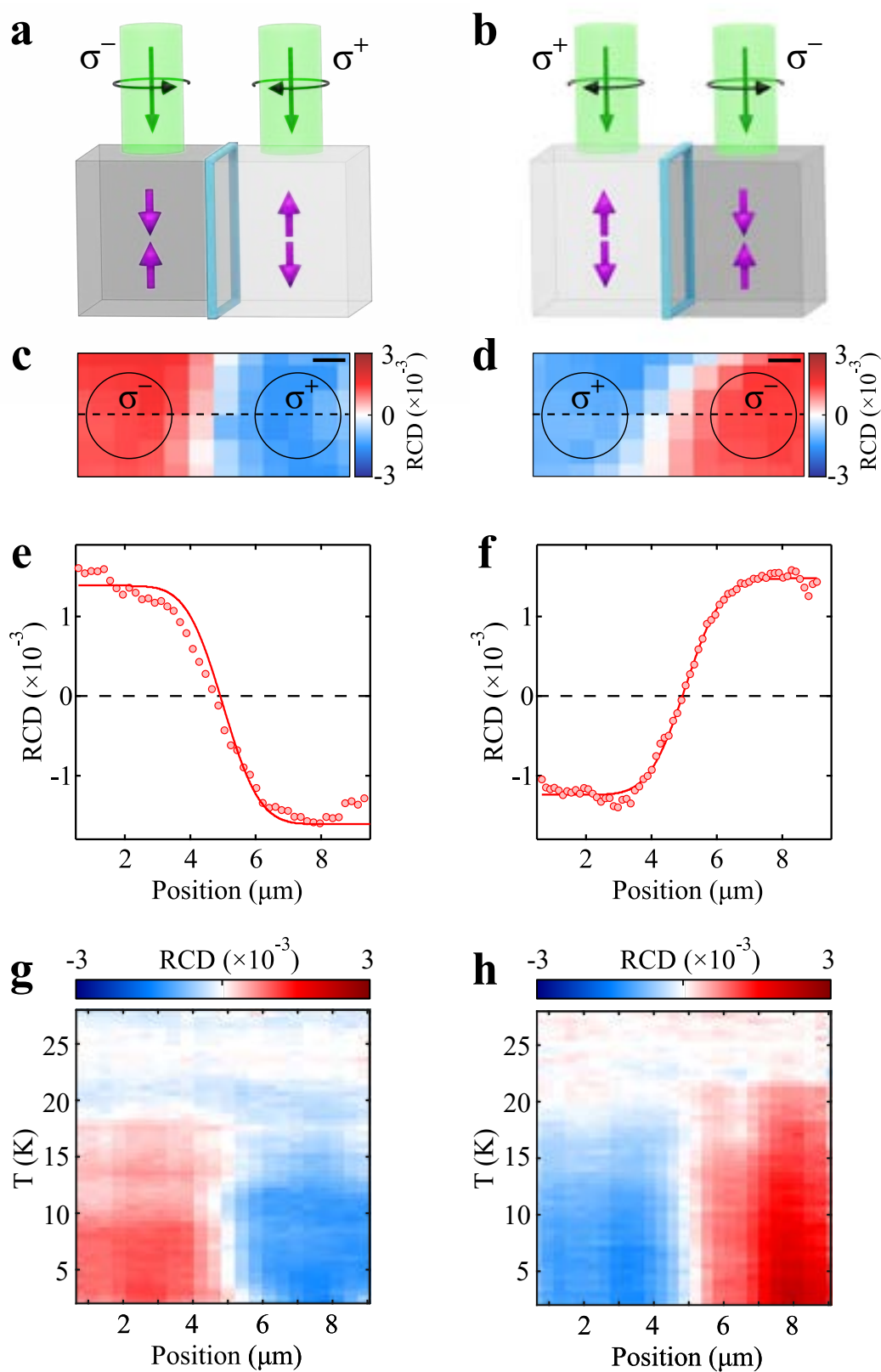


Fig. S30: **a-b** Schematics of the double induction. **c-d**, RCD map after double induction. **e-f**, RCD line-cut plot along the dashed lines in panels (c,d). **g-h**, Temperature dependence of the line-cut plot.

II.4. Additional ultrafast switching data

Optical induction experiments with ultrafast laser: In the main text, we showed direct switching by ultrafast pulses while the sample temperature was kept at 18 K. Before doing that, we also conducted optical induction experiments with ultrafast pulses, i.e., we shone the ultrafast pulsed light while cooling the entire sample from 30 K to 2K. We found that the ultrafast pulses can also achieve optical induction with similar results as the super-continuum laser (Fig. S31).

Comparison of RCD map before and after ultrafast switching: Figures S32a,d show the RCD map of the prepared single domain state before ultrafast switching, which is in clear contrast to RCD map after ultrafast switching (shown in Figs. S32b-c,e-f).

Reproducibility of ultrafast switching: To further substantiate the ultrafast switching results, we repeated the switching experiments multiple times for each helicity and domain type (as shown in Fig. S34), which all yielded consistent results.

Statistics of ultrafast switching: As shown in Fig. S33, we measured the statistics of ultrafast switching. While we can definitely switch the sign of the RCD based on helicity, we cannot reach the saturated RCD value every time. We note that our preliminary results can be further improved by detailed explorations in the future. With optimized conditions (e.g. wavelength, rep. rate, pulse energy, etc.), it may be possible to switch to a fully-saturated state.

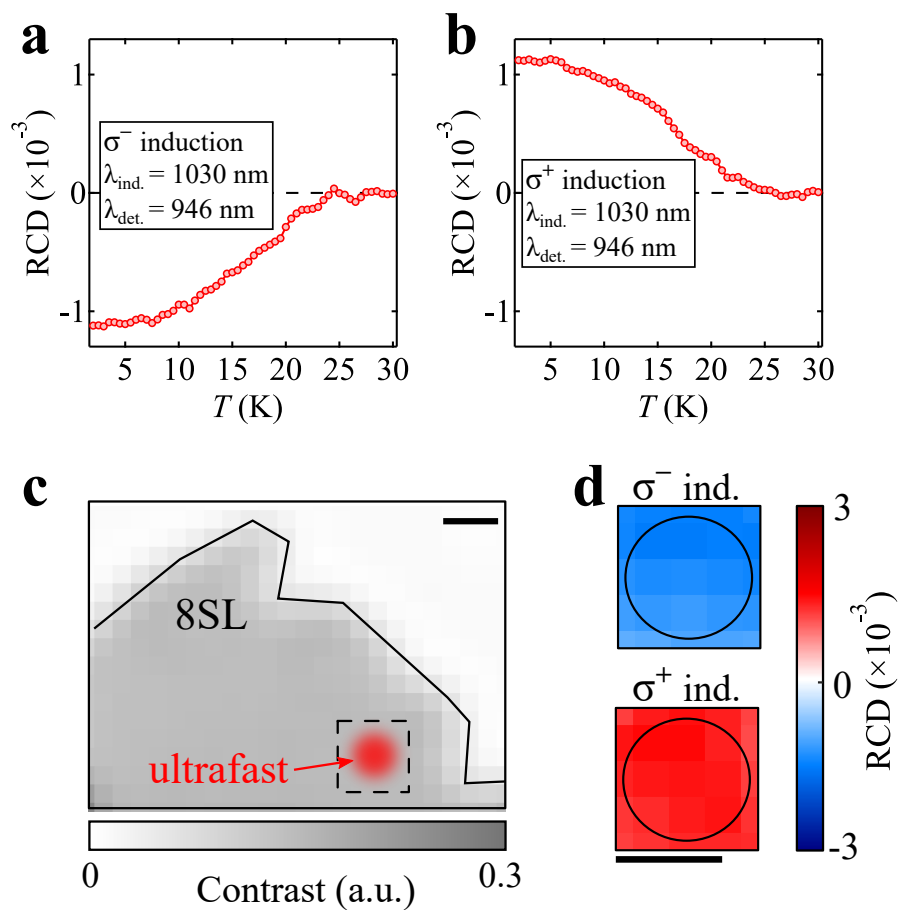


Fig. S31: Axion induction with the circularly-polarized ultrafast light. **a-b**, Temperature-dependence of RCD after induction using σ^\pm ultrafast light (with $\lambda_{\text{induction}} = 1030 \text{ nm}$). **c**, Optical contrast of the 8SL flake. **d**, RCD map upon induction using σ^\pm .

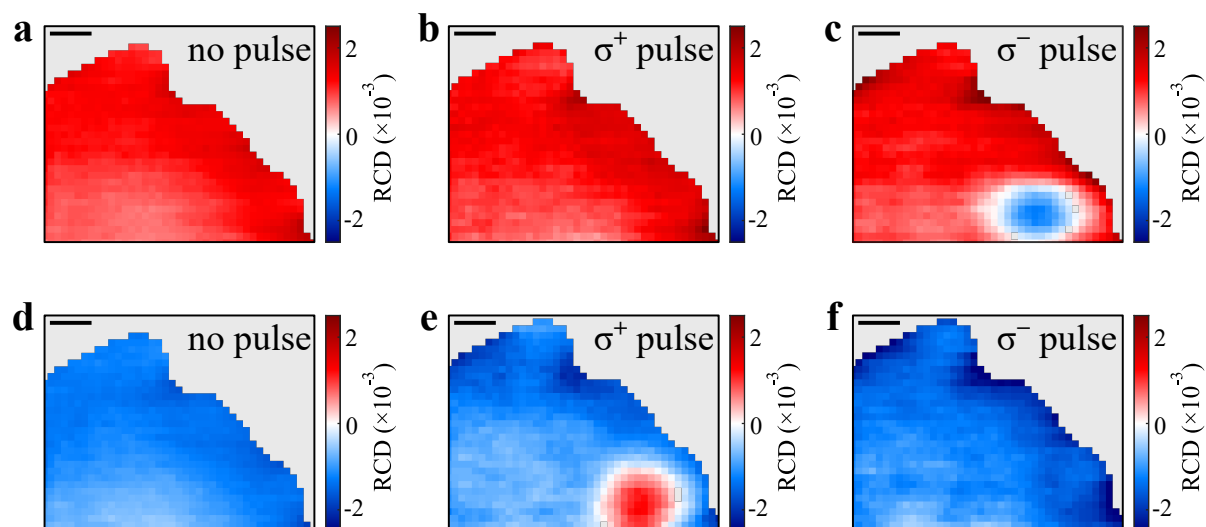


Fig. S32: **a**, RCD map of the single domain state prepared by sweeping the B field from +7 T to 0 T. **b-c**, RCD map after optical induction with σ^\pm ultrafast pulse. **d-f**, Same as panel (a-c) but with the single domain state prepared by sweeping the B field from -7 T to 0 T.

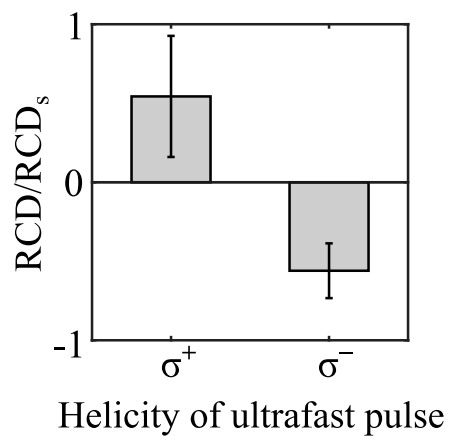


Fig. S33: Ultrafast switching statistics. RCD value after illumination with ultrafast light, weighed against the saturated value RCD_s .

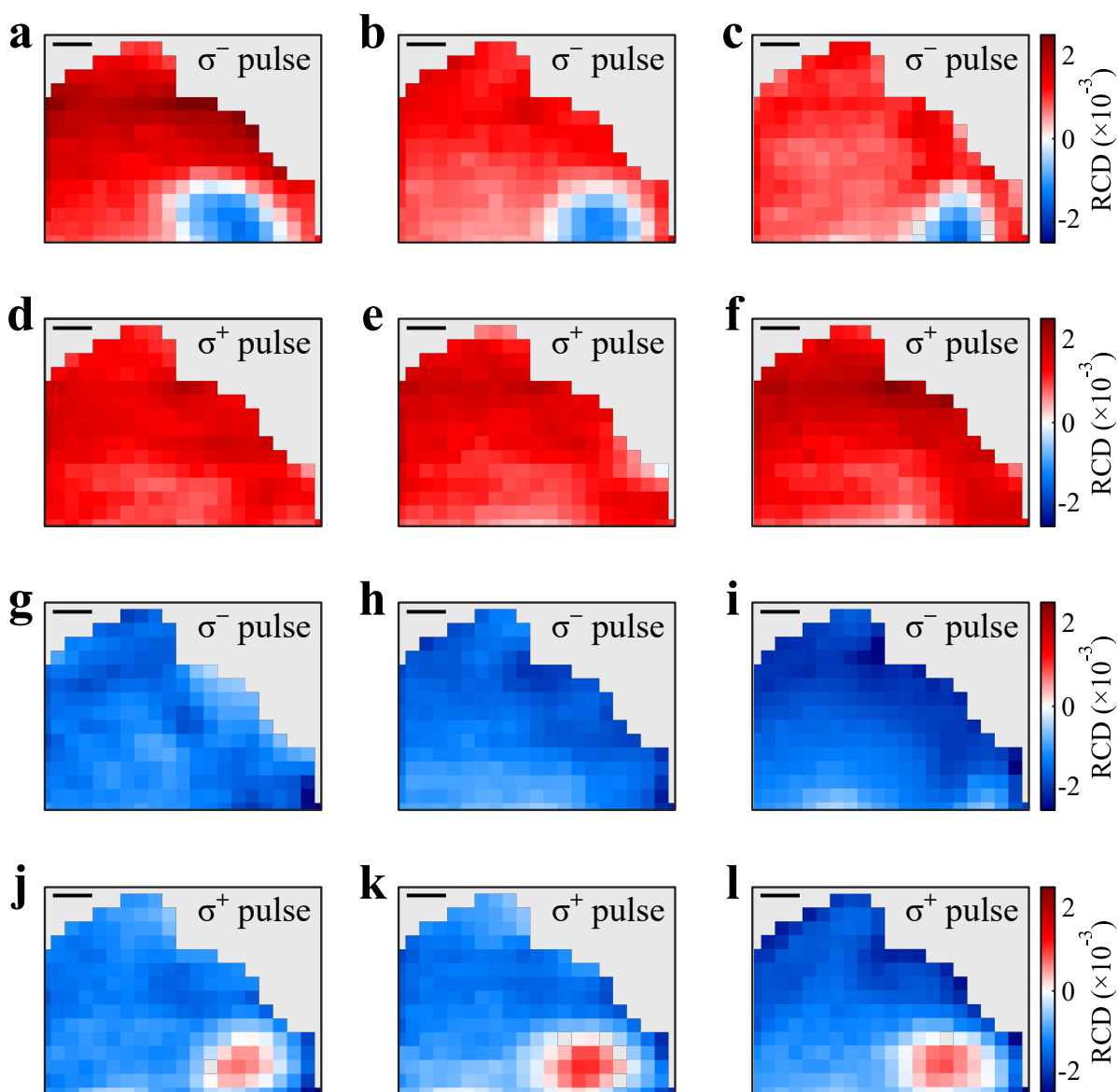


Fig. S34: Reproducibility of switching with circularly-polarized ultrafast light. **a-c**, RCD maps after shining σ^- ultrafast pulsed light (we first prepare the single domain state by sweeping the B field from +7 T to 0 T). **d-f**, The same as panels (**a-c**) but with σ^+ ultrafast pulsed light. **g-i**, Same as panels (**a-f**) but with the single domain state prepared by sweeping the B field from -7 T to 0 T. Scale bar: 2 μm .

II.5. Additional electrical transport data

The entire device fabrication process was finished in an Ar-filled glovebox without exposure to air, chemicals, or heat. Using a similar fabrication process, we have also fabricated a 6SL MnBi₂Te₄ device with electrical contacts and performed transport experiments in the same cryostat as the optical CD measurements (Fig. S35). In the FM phase at $B = -7$ T, we observed clear topological Chern insulator state with fully quantized R_{yx} and zero R_{xx} .

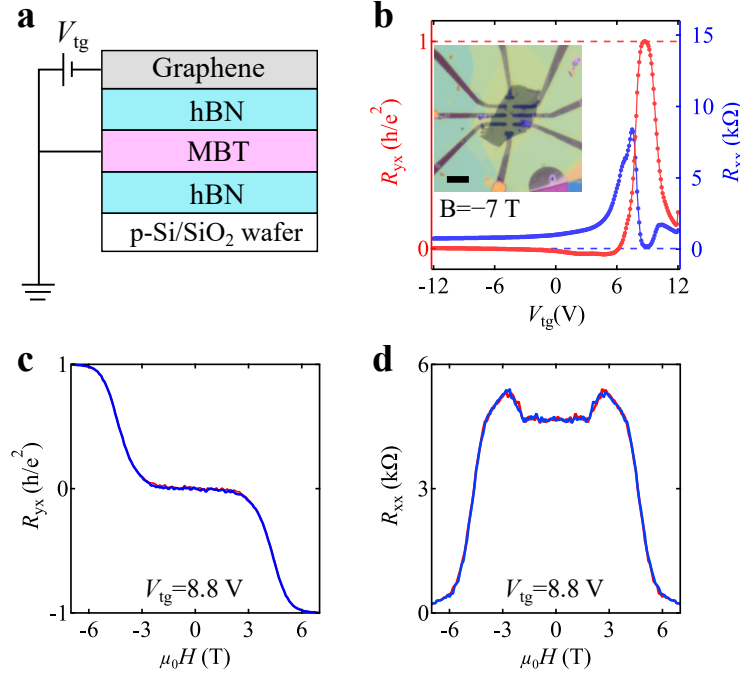


Fig. S35: **a**, Schematic layout for the 6SL MnBi₂Te₄ sample (Sample-S5) used for electrical transport. The transport experiments were performed in the same cryostat as the optical CD. **b**, Longitudinal (R_{xx}) and Hall (R_{yx}) responses as a function of the gate voltage in the FM phase at $B = -7$ T. Inset: Optical image of the sample. Scale bar: $10 \mu\text{m}$. **c,d**, R_{yx} and R_{xx} as a function of B with the gate voltage tuned to the charge neutrality.

III. Symmetry analysis of the CD

III.1. General principles

We start by outlining the general principles for the symmetry analysis of the CD. We need to specify a system (i.e., a chiral crystal, a FM, or an AFM) and enumerate all the symmetries of that particular system. We also need to specify a particular CD process, e.g. RCD or TCD. Once both the system and the CD process are specified, then the general principles for the symmetry analysis are as follows:

(1) **To prove the CD is zero:** One needs to identify a symmetry which can keep the system and the light path invariant but flip the light helicity.

(2) **To prove the CD is allowed:** One needs to exhaustively examine all symmetries, to show that there is no symmetry that can achieve (1).

III.2. Three material classes and their symmetries

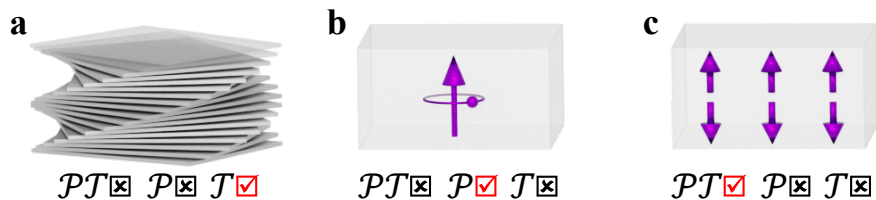


Fig. S36: Three material classes (Chiral crystals, FM and AFM) and their respective symmetry properties. Note that the symmetries described here are for the typical cases. Strictly speaking, it is possible for FMs to be in a noncentrosymmetric lattice (\mathcal{P} -breaking), or chiral crystals to have magnetism (\mathcal{T} -breaking). But most FMs are not considered to be associated with inversion symmetry breaking and most spatially chiral systems are not considered to be associated with time-reversal symmetry breaking. When all symmetries are broken, then all kinds of CD would be allowed in the system (in some sense, the distinction between different material classes is lost when all symmetries are broken, because phases of matter are only classified based on the symmetry).

III.3. Application to AFM and other systems

We now carry out symmetry analysis for CD in these three material classes.

We start from the \mathcal{PT} -symmetric AFMs. In the main text, we have shown that \mathcal{PT} enforces $\text{TCD} = 0$. So we will be brief: As shown in Fig. S37a, upon \mathcal{PT} , both the AFM order and light path remain invariant, but light helicity is reversed. As such, \mathcal{PT} enforces the transmission coefficients for σ^\pm to be identical, which means $\text{TCD} = 0$. We can also show that RCD is allowed, because there is no symmetry that can keep the AFM order and reflection light path invariant but only flip the light helicity. For instance, \mathcal{PT} changes the reflection to the bottom surface (Fig. S37b). On the other hand, \mathcal{T} flips the AFM order (Fig. S37c).

We now study the chiral crystals. We show that \mathcal{T} enforces $\text{RCD} = 0$. As shown in Fig. S37d, upon \mathcal{T} , the chiral crystal remains invariant, the reflection light path also stays the same, but light helicity is reversed. As such, \mathcal{T} enforces the reflection coefficients for σ^\pm to be identical, which means $\text{RCD} = 0$ in chiral crystals.

Using the same method, we can show that chiral crystals allow TCD, and that FMs allow both RCD and TCD.

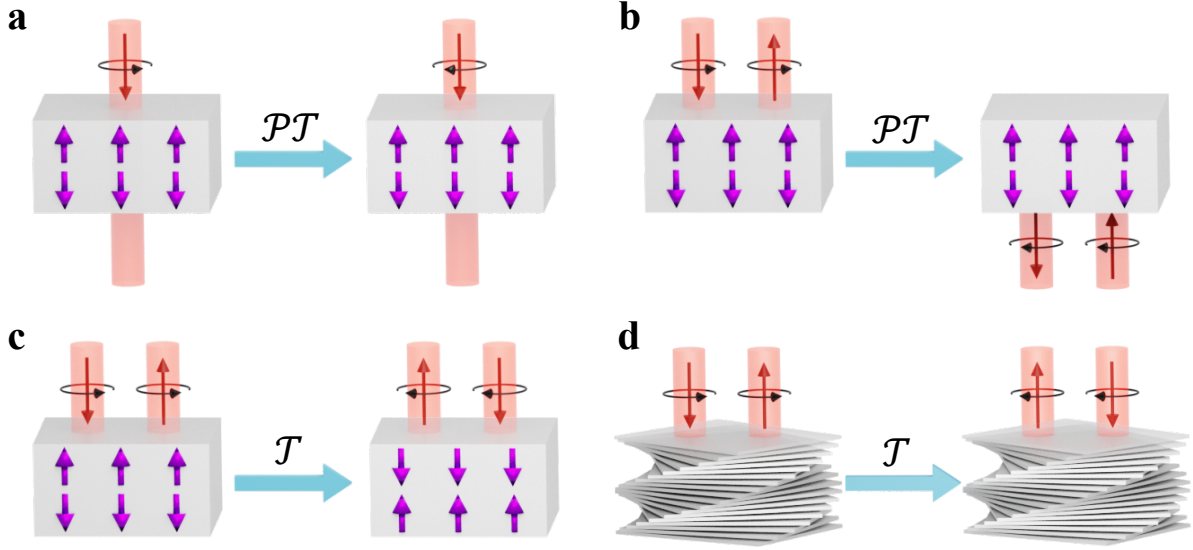


Fig. S37: Symmetry transformation for different CD experiments on different material systems (see detailed analysis in SI III.3).

III.4. Math derivation for symmetry analysis

We now provide mathematical derivation for the above symmetry analysis. We will be brief in this section because the detailed derivation can be found in previous works by Halperin and others [6–9]. We consider a generic experimental layout (Fig. S38), which consists of the sample at the origin, the light source at position \mathbf{r}_1 , and the detector at position \mathbf{r}_2 . The propagator $\chi_{ij}(\mathbf{r}_1, \mathbf{r}_2)$ (the Green's function) contains all information about how the light starts from the light source at \mathbf{r}_1 , interacts with sample at the origin, and reaches the detector at \mathbf{r}_2 . This propagator is defined as follows

$$\langle \hat{A}_a(t_1, \mathbf{r}_1) \rangle = \langle \hat{A}_a(t_1, \mathbf{r}_1) \rangle_{J=0} + \int dt_2 d\mathbf{r}_2 \chi_{ab}(t_1, \mathbf{r}_1; t_2, \mathbf{r}_2) J_b(t_2, \mathbf{r}_2), \quad (\text{S11})$$

where \hat{A} is the vector potential, $J_a(t', \mathbf{r}')$ is the source current, and

$$\chi_{ab}(t_1, \mathbf{r}_1; t_2, \mathbf{r}_2) = \langle \hat{A}_a(t_1, \mathbf{r}_1) \hat{A}_b(t_2, \mathbf{r}_2) \rangle = \sum_n \rho_n \langle \hat{A}_a(t_1, \mathbf{r}_1) \psi_n | \hat{A}_b(t_2, \mathbf{r}_2) \psi_n \rangle \quad (\text{S12})$$

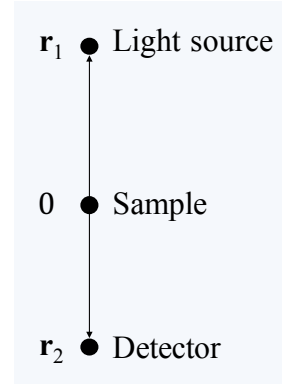


Fig. S38: Schematics layout.

is the Green's function for the vector potential \hat{A} , where ψ_n is the eigenstate of the density operator $\hat{\rho}$ of the whole medium, including the sample and the vacuum while excluding the detector and source, where ρ_n is the corresponding eigenvalue.

Therefore, we can perform symmetry analysis for the Green's function $\chi_{ij}(\mathbf{r}_1, \mathbf{r}_2)$. In particular, the circular dichroism with light propagating along the z direction is given by the antisymmetric part of the Green's function

$$\text{circular dichroism} \propto \chi_{xy} - \chi_{yx} \quad (\text{S13})$$

1. **Reflection CD:** For reflection CD, the key feature is that the light source and the detector are on the same side of the sample, so we can make them spatially overlap, i.e., $\mathbf{r}_2 = \mathbf{r}_1$. Therefore, we have

$$\text{Reflection CD} \propto \chi_{xy}(\mathbf{r}_1, \mathbf{r}_1) - \chi_{yx}(\mathbf{r}_1, \mathbf{r}_1). \quad (\text{S14})$$

One can show that time-reversal symmetry \mathcal{T} enforces

$$\chi_{xy}(\mathbf{r}_1, \mathbf{r}_1) \equiv \chi_{yx}(\mathbf{r}_1, \mathbf{r}_1) \quad \text{under } \mathcal{T} \text{ symmetry} \quad (\text{S15})$$

As such, we see that RCD identically vanishes under \mathcal{T} .

2. **Transmission CD:** For transmission CD, the key feature is that the light source and the detector are on the opposite side of the sample, so we can require, i.e., $\mathbf{r}_2 = -\mathbf{r}_1$. Therefore, we have

$$\text{Transmission CD} \propto \chi_{xy}(\mathbf{r}_1, -\mathbf{r}_1) - \chi_{yx}(\mathbf{r}_1, -\mathbf{r}_1). \quad (\text{S16})$$

One can show that space-time symmetry \mathcal{PT} enforces

$$\chi_{xy}(\mathbf{r}_1, -\mathbf{r}_1) \equiv \chi_{yx}(\mathbf{r}_1, -\mathbf{r}_1) \quad \text{under } \mathcal{PT} \text{ symmetry} \quad (\text{S17})$$

As such, we see that TCD identically vanishes under \mathcal{PT} .

IV. Theoretical studies

IV.1. Theoretical expressions for calculating the Axion CD

In this section, we provide the theoretical expressions that are needed to compute the RCD based on the optical Axion electrodynamics. The detailed derivations for these expressions can be found in Ref. [4] (Please note the same ME coefficient is denoted as α in our paper but $G^{(z)}$ in Ref. [4]). An illustration of the key steps is shown in Fig. S39.

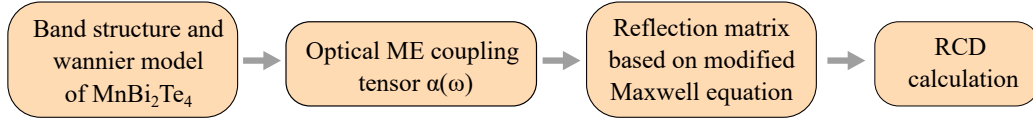


Fig. S39: Key steps for the theoretical calculations of the Axion CD

IV.1.1. Band Structure and the Wannier model

First we calculated the band structure and Wannier functions of 2D even-layer MnBi_2Te_4 flakes using first-principles DFT calculations.

IV.1.2. The Optical ME coupling

Using the first-principles electronic structure, we can calculate the optical ME coupling. Based on the detailed theoretical studies in Ref. [4], the expression for optical ME coupling is as follows:

$$\alpha_{xx}(\omega) = \frac{e^2}{\hbar L} \sum_{o,u} \int d^2\mathbf{k} \frac{\varepsilon_{ou}(\mathbf{k})}{\varepsilon_{uo}(\mathbf{k}) - \hbar\omega} \text{Im} \left[\frac{\hbar^2 \langle o(\mathbf{k}) | \hat{v}^x | u(\mathbf{k}) \rangle \langle u(\mathbf{k}) | -\frac{1}{2} (\hat{v}^y \hat{r}^z + \hat{r}^z \hat{v}^y) + \hat{m}_x^s | o(\mathbf{k}) \rangle}{\varepsilon_{uo}^2(\mathbf{k})} \right], \quad (\text{S18})$$

$o(\mathbf{k})$ and $u(\mathbf{k})$ are the occupied and unoccupied Bloch states and $\varepsilon_{uo}(\mathbf{k})$ is their energy difference. As explained in the main text, the ME coupling can be decomposed into the spin and orbital (Berry

curvature) contributions as follows:

$$\alpha_{xx}(\omega) = \alpha_{xx}^{\text{Berry}}(\omega) + \alpha_{xx}^{\text{spin}}(\omega), \quad (\text{S19})$$

$$\alpha_{xx}^{\text{Berry}}(\omega) = \frac{e^2}{\hbar L} \sum_{\text{o,u}} \int d^2\mathbf{k} \frac{\varepsilon_{\text{uo}}(\mathbf{k})}{\varepsilon_{\text{uo}}(\mathbf{k}) - \hbar\omega} \text{Im} \left[\frac{\hbar^2 \langle \text{o}(\mathbf{k}) | \hat{v}^x | \text{u}(\mathbf{k}) \rangle \langle \text{u}(\mathbf{k}) | \hat{v}^y \hat{r}^z | \text{o}(\mathbf{k}) \rangle}{\varepsilon_{\text{uo}}^2(\mathbf{k})} \right], \quad (\text{S20})$$

$$\alpha_{xx}^{\text{spin}}(\omega) = \frac{e^2}{\hbar L} \sum_{\text{o,u}} \int d^2\mathbf{k} \frac{\varepsilon_{\text{ou}}(\mathbf{k})}{\varepsilon_{\text{uo}}(\mathbf{k}) - \hbar\omega} \text{Im} \left[\frac{\hbar^2 \langle \text{o}(\mathbf{k}) | \hat{v}^x | \text{u}(\mathbf{k}) \rangle \langle \text{u}(\mathbf{k}) | \hat{m}_x^s | \text{o}(\mathbf{k}) \rangle}{\varepsilon_{\text{uo}}^2(\mathbf{k})} \right], \quad (\text{S21})$$

Here we have assumed that \hat{r}^z commutes with \hat{v}^y (we have confirmed that this is a good approximation for our first-principles calculated DFT electronic structure). Equation S20 is the Berry curvature induced optical ME coupling we used in the main text. Equation S21 is the spin induced optical ME coupling. Figure S40 shows the real and imaginary components of $\alpha_{xx}(\omega)$ for both spin and orbital (Berry curvature) contributions.

In addition, we clarify the relationship between the optical ME coupling coefficients and Axion angle $\theta(\omega)$.

$$\theta(\omega) = \pi \frac{2\hbar}{e^2} \frac{1}{3} \sum_{i=x,y,z} \alpha_{ii}(\omega), \quad (\text{S22})$$

$$\alpha_{xx}(\omega) = \frac{e^2}{\hbar L} \sum_{\text{o,u}} \int d^2\mathbf{k} \frac{\varepsilon_{\text{ou}}(\mathbf{k})}{\varepsilon_{\text{uo}}(\mathbf{k}) - \hbar\omega} \text{Im} \left[\frac{\hbar^2 \langle \text{o}(\mathbf{k}) | \hat{v}^x | \text{u}(\mathbf{k}) \rangle \langle \text{u}(\mathbf{k}) | -\frac{1}{2} (\hat{v}^y \hat{r}^z + \hat{r}^z \hat{v}^y) + \hat{m}_x^s | \text{o}(\mathbf{k}) \rangle}{\varepsilon_{\text{uo}}^2(\mathbf{k})} \right], \quad (\text{S23})$$

$$\alpha_{yy}(\omega) = \frac{e^2}{\hbar L} \sum_{\text{o,u}} \int d^2\mathbf{k} \frac{\varepsilon_{\text{ou}}(\mathbf{k})}{\varepsilon_{\text{uo}}(\mathbf{k}) - \hbar\omega} \text{Im} \left[\frac{\hbar^2 \langle \text{o}(\mathbf{k}) | \hat{v}^y | \text{u}(\mathbf{k}) \rangle \langle \text{u}(\mathbf{k}) | +\frac{1}{2} (\hat{v}^x \hat{r}^z + \hat{r}^z \hat{v}^x) + \hat{m}_y^s | \text{o}(\mathbf{k}) \rangle}{\varepsilon_{\text{uo}}^2(\mathbf{k})} \right], \quad (\text{S24})$$

$$\alpha_{zz}(\omega) = \frac{e^2}{\hbar L} \sum_{\text{o,u}} \int d^2\mathbf{k} \frac{\varepsilon_{\text{ou}}(\mathbf{k})}{\varepsilon_{\text{uo}}(\mathbf{k}) - \hbar\omega} \text{Im} \left[\frac{\frac{\hbar^2}{2} (\langle \text{o}(\mathbf{k}) | \hat{r}^z | \text{u}(\mathbf{k}) \rangle \langle \text{u}(\mathbf{k}) | \hat{v}^x \hat{v}^y | \text{o}(\mathbf{k}) \rangle - \langle \text{o}(\mathbf{k}) | \hat{r}^z \hat{v}^x | \text{u}(\mathbf{k}) \rangle \langle \text{u}(\mathbf{k}) | \hat{v}^y | \text{o}(\mathbf{k}) \rangle)}{\varepsilon_{\text{uo}}^2(\mathbf{k})} \right. \\ \left. - (x \leftrightarrow y) + \frac{\hbar^2 \langle \text{o}(\mathbf{k}) | \hat{v}^z | \text{u}(\mathbf{k}) \rangle \langle \text{u}(\mathbf{k}) | \hat{m}_z^s | \text{o}(\mathbf{k}) \rangle}{\varepsilon_{\text{uo}}^2(\mathbf{k})} \right] \quad (\text{S25})$$

We see that $\theta(\omega)$ is proportional to the trace of the optical ME tensor. For our CD experiments, α_{xx} and α_{yy} are relevant since the light's E and B fields are inside the 2D plane. Moreover, $\alpha_{xx} \equiv \alpha_{yy}$ because of MnBi_2Te_4 's three-fold rotational symmetry. As such, $\alpha_{xx}(\omega)$ is sufficient for the CD calculations, so in the main text we omitted the subscript xx . In fact, our calculations (Fig. S42) show that α_{xx} , α_{yy} and α_{zz} have very similar amplitude. Therefore, we have

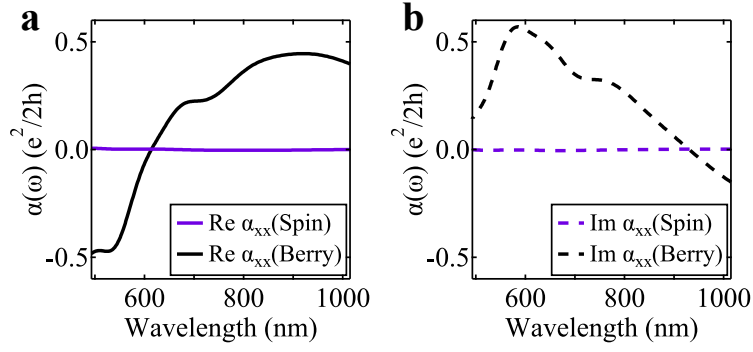


Fig. S40: Real and imaginary parts of $\alpha_{xx}^{\text{spin}}$ and $\alpha_{xx}^{\text{Berry}}$.

$$\theta(\omega) = \pi \frac{2h}{e^2} \frac{1}{3} \sum_{i=x,y,z} \alpha_{ii}(\omega) \simeq \pi \frac{2h}{e^2} \alpha_{xx}(\omega) \quad (\text{S26})$$

IV.1.3. Reflection matrix based on modified Maxwell equations

We now aim to analyze the light reflection based on the optical Axion electrodynamics. As shown in Fig. S41, we consider an Axion insulator film (medium 2) sandwiched by two dielectric media (1 and 3). Suppose the incident electric field is $\mathbf{E}^{\text{I}} = (E_x^{\text{I}}, E_y^{\text{I}})$. Then the reflected electric field can be related by a reflection matrix $\mathbf{E}^{\text{R}} = R\mathbf{E}^{\text{I}}$, and the reflection matrix R is defined in Eq. S27

$$R = \begin{pmatrix} R_{xx} & R_{xy} \\ -R_{xy} & R_{xx} \end{pmatrix} \quad (\text{S27})$$

For the film with finite thickness considered here (Fig. S41b), the final reflected electric field \mathbf{E}^{R} consists of contributions from both the top (t) and the bottom (b) surfaces, which can be described as follows:

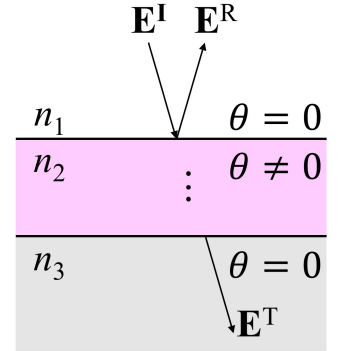


Fig. S41: Schematics of reflection and transmission.

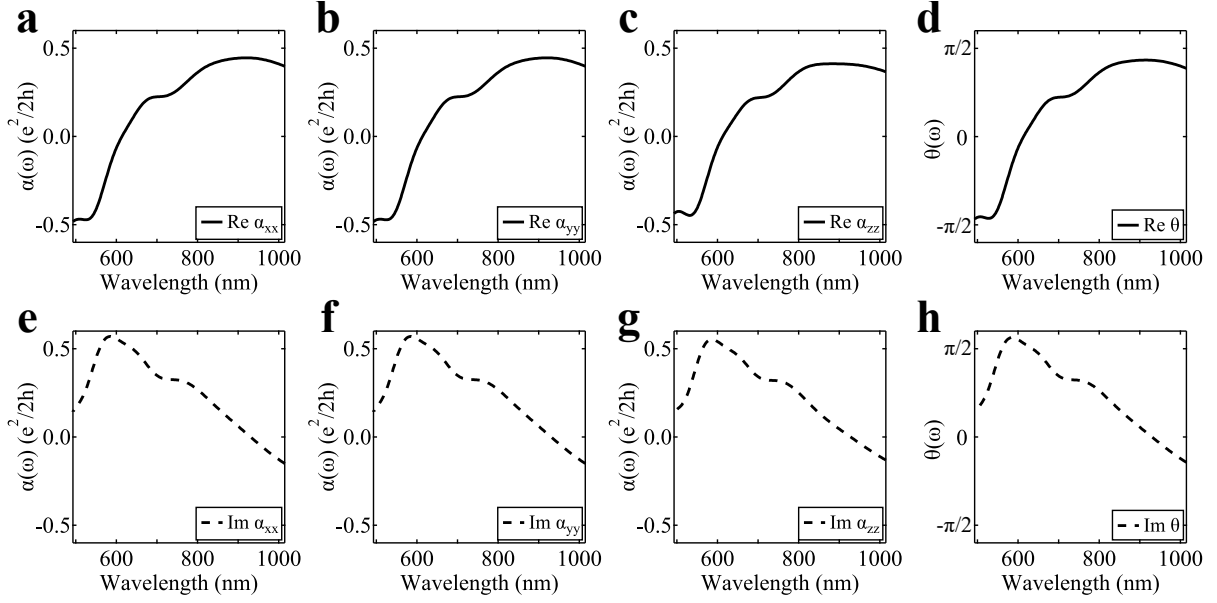


Fig. S42: Real and imaginary parts of α and θ . Note that we only show the orbital (Berry curvature) contribution here, since the spin contribution is vanishingly small.

$$\begin{aligned}
(R_t)_{xx} &= \frac{(n_1 - n_2)(n_1 + n_2) - (\mu_0 c \alpha_{xx})^2}{(\mu_0 c \alpha_{xx})^2 + (n_1 + n_2)^2}, \\
(R_t)_{xy} &= \frac{-2n_1(\mu_0 c \alpha_{xx})}{(\mu_0 c \alpha_{xx})^2 + (n_1 + n_2)^2}, \\
(R'_t)_{xx} &= \frac{-(n_1 - n_2)(n_1 + n_2) - (\mu_0 c \alpha_{xx})^2}{(\mu_0 c \alpha_{xx})^2 + (n_1 + n_2)^2}, \\
(R'_t)_{xy} &= \frac{-2n_2(\mu_0 c \alpha_{xx})}{(\mu_0 c \alpha_{xx})^2 + (n_1 + n_2)^2}, \\
(R_b)_{xx} &= \frac{(n_2 - n_3)(n_2 + n_3) - (\mu_0 c \alpha_{xx})^2}{(\mu_0 c \alpha_{xx})^2 + (n_2 + n_3)^2}, \\
(R_b)_{xy} &= \frac{2n_2(\mu_0 c \alpha_{xx})}{(\mu_0 c \alpha_{xx})^2 + (n_2 + n_3)^2}.
\end{aligned} \tag{S28}$$

where R_t and R'_t are reflections of the top surface from medium 1 to 2 and from medium 2 to 1, R_b is the reflection of the bottom surface from medium 2 to 3, and n_i is the refractive index of the medium i . We see that α_{xx} appears in the expressions. This is because to solve for R_t , R'_t and R_b , we needed to use the optical Axion electrodynamics based on the modified Maxwell equations. The detailed derivations are described in Ref. [4].

We then plug in R_t , R'_t and R_b to the following equation. The final reflection matrix R is then obtained by solving this equation:

$$R = R_t + e^{2i\phi}(1 + R'_t)R_b (1 - e^{2i\phi}R'_tR_b)^{-1} (1 + R_t), \quad (\text{S29})$$

Here, $\phi = n_2\omega L/c$ is the complex-valued phase obtained by the one-way propagation through the sample (L : sample thickness).

IV.1.4. RCD calculation

Based on the reflection matrix obtained above, we then calculate the RCD by:

$$\text{RCD} = \frac{|R_{++}|^2 - |R_{--}|^2}{|R_{++}|^2 + |R_{--}|^2} = \frac{2\text{Im}[R_{xx}^*R_{xy}]}{|R_{xx}|^2 + |R_{xy}|^2}, \quad (\text{S30})$$

where $R_{++} = 2(R_{xx} - iR_{xy})$ and $R_{--} = 2(R_{xx} + iR_{xy})$.

IV.1.5. TCD calculation

Similarly, we could also express the transmission matrix T as follows

$$T = e^{i\phi}(1 + R_b) (1 - e^{2i\phi}R'_tR_b)^{-1} (1 + R_t) = \begin{pmatrix} T_{xx} & T_{xy} \\ -T_{xy} & T_{xx} \end{pmatrix}. \quad (\text{S31})$$

Based on the transmission matrix obtained above, we then calculate the TCD by:

$$\text{TCD} = \frac{|T_{++}|^2 - |T_{--}|^2}{|T_{++}|^2 + |T_{--}|^2} = \frac{2\text{Im}[T_{xx}^*T_{xy}]}{|T_{xx}|^2 + |T_{xy}|^2} \quad (\text{S32})$$

where $T_{++} = 2(T_{xx} - iT_{xy})$ and $T_{--} = 2(T_{xx} + iT_{xy})$.

(1) No TCD with \mathcal{PT} symmetry

When we consider the 2D even-layered MnBi_2Te_4 flakes alone or hBN-encapsulated MnBi_2Te_4 flakes, \mathcal{PT} symmetry is strictly preserved and TCD is strictly prohibited. Indeed, using Eqs. S31 and S32, one can check that

$$\text{TCD} \equiv 0 \quad \text{under } \mathcal{PT} \quad (\text{S33})$$

(2) Very small TCD with asymmetric dielectrics

In the experiments, the MnBi_2Te_4 flakes are interfaced with different dielectric materials. So we need to reconsider the symmetry of the whole system. For the hBN/ MnBi_2Te_4 /diamond structure,

since the refractive indices of hBN and diamond are slightly different ($n^{\text{hBN}=2.2}$, $n^{\text{diamond}=2.4}$ at 1 eV [10, 11]), the \mathcal{PT} symmetry of the whole system is slightly broken, which in principle could allow TCD (see detailed discussion in Ref. [4]). This TCD signal should be very small, since the degree of \mathcal{PT} symmetry breaking is very weak. Main Fig. 4f shows the calculated results for the hBN/MnBi₂Te₄/diamond structure. Indeed, our calculations show that the TCD in this case is negligibly small.

IV.2. Band structure of MnBi₂Te₄ and additional calculations

In this subsection, we provide an introduction of the electronic structure of 2D MnBi₂Te₄. We hope this serves as useful information for readers who are not familiar with this new material.

IV.2.1. Localized magnetic ions versus low-energy itinerant electrons

The recent discoveries of the vdW magnets [12–14] have attracted great interest as they enable us to explore magnetism in the ultra-2D limit. MnBi₂Te₄ [15–26] provides novel possibilities: Known 2D magnets such as CrI₃ are wide-gap magnetic insulators whose physics is dominated by the localized magnetic ions. By contrast, in addition to localized magnetic ions, MnBi₂Te₄ features low-energy itinerant electrons. These low-energy electronic states arise from the delocalized Bi and Te p orbitals: They make up the bulk conduction and valance bands, with the topological surface states (TSSs) in between. Figure S43 shows the first-principles calculated electronic structure of MnBi₂Te₄ over a large energy window. Indeed, we see that the Mn $3d$ bands are located at very high energies. Therefore, in our optical experiments (photon energy 1.2 eV to 2.4 eV), they are not expected to directly contribute. This is consistent with our calculations showing that the spin contribution is negligibly small in the ME coupling.

IV.2.2. Low-energy electronic structures of 2D MnBi₂Te₄

As a reference, Fig. S44 shows the first-principles calculated low-energy electronic structures of 2D MnBi₂Te₄ as a function of thickness. We note the following aspects: (1) The lowest conduction band plus the highest valance band make up the topological surface states (TSSs). (2) The higher bands are the bulk bands.

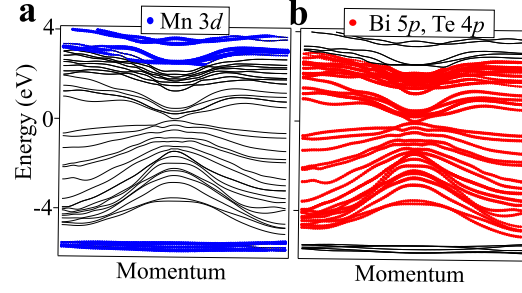


Fig. S43: **a**, First-principles calculated electronic structure of MnBi_2Te_4 with the Mn $3d$ orbitals highlighted. **b**, Same as panel (a) but with the Bi $5p$ and Te $4p$ orbitals highlighted.

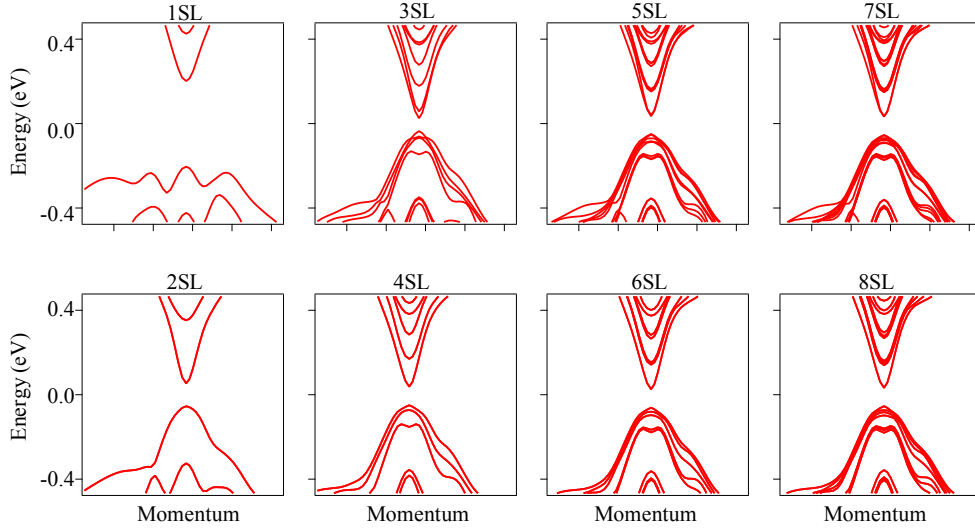


Fig. S44: First-principles calculated band structures of 2D MnBi_2Te_4 .

IV.2.3. Band-resolved contributions for optical ME coupling

As described above, the Mn magnetic spins are not expected to contribute significantly to our optical ME coupling, because the Mn bands are located at very high energies (Fig. S43). By contrast, the main contribution is from the Bi and Te electronic bands. Figure S45 shows the band-resolved contribution for the optical ME coupling at $\hbar\omega = 1.77$ eV.

In Fig. S46, we compare the total α and the α from TSS contributions (i.e., inter-band transitions where the initial state or final state or both are the TSSs) for 2, 4, and 6SL. While the TSSs give finite contribution, the contribution from higher bands is generally larger. For 2SL, the TSS contribution is quite significant, which is possibly because there are fewer higher bulk bands in 2SL.

In Fig. S47a, we compute the optical conductivity $\sigma(\omega)$ from 550 – 1000 nm for 6SL MnBi_2Te_4 . We observe a small bump near 700 nm (1.77 eV). In Fig. S47b, we show a band resolved contribution for $\sigma(\omega)$. This small bump may arise from the transitions shown by the black arrows shown in

Fig. S47b, where the conduction and valence bands turn out to be roughly "parallel".

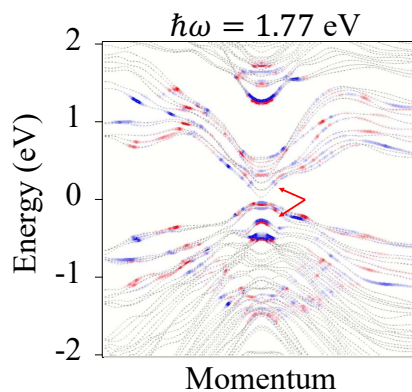


Fig. S45: Band-resolved contribution to the optical ME coupling at $\hbar\omega = 1.77$ eV (700 nm).

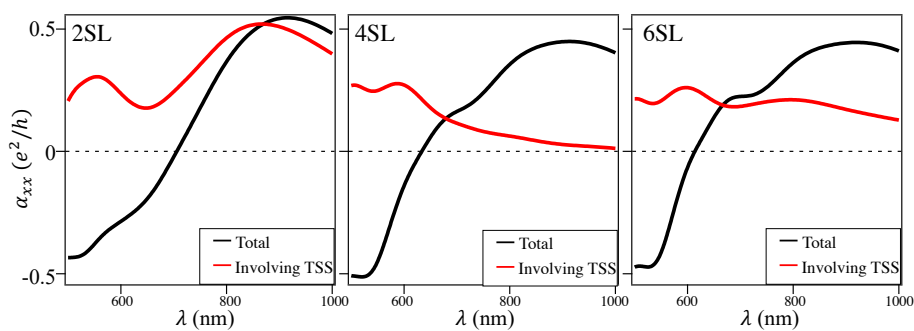


Fig. S46: Calculated $\alpha(\omega)$ for 2, 4, 6 SL from all possible contributions (black) and $\alpha(\omega)$ from contributions only involving the lowest CB or highest VB.

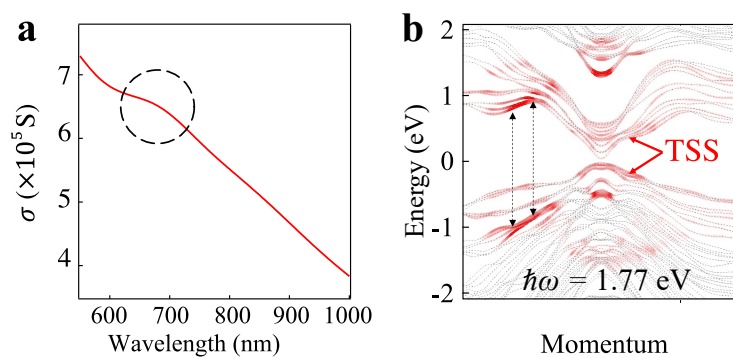


Fig. S47: **a**, Calculated optical conductivity $\sigma(\omega)$ for 6SL. **b**, Band resolved contribution for the calculated optical conductivity $\sigma(\omega)$. The lowest conduction and highest valence bands are the topological surface states (TSS).

IV.3. Mathematical derivation of RCD/Kerr under different symmetry condition

Below, we show that by considering the general wave equation and proper boundary conditions, we can show in a unifying scheme that RCD/Kerr is zero under \mathcal{T} -symmetry; but RCD/Kerr is nonzero with \mathcal{T} -breaking (especially for our MnBi_2Te_4 system). In this derivation, we used G for the optical ME coupling.

1. Wave equation

The wave equation up to electric quadrupole/magnetic dipole takes the following form [27]:

$$\left[\delta_{ij} + \epsilon_0^{-1} \tilde{\chi}_{ij} + i\mu_0 n c \sum_k \kappa_k \tilde{\sigma}_{ijk} + n^2 (\kappa_i \kappa_j - \delta_{ij}) \right] E_j = 0 \quad (\text{S34})$$

where $\tilde{\chi}_{ij} = \chi_{ij} - i\chi'_{ij}$ satisfying $\chi_{ij} = \chi_{ji}$ and $\chi'_{ij} = -\chi'_{ji}$, $\kappa_i = k_i/|\mathbf{k}|$ is the propagation direction of light, n is the refractive index, $\tilde{\sigma}_{ijk} = \sigma_{ijk}^S - i\sigma_{ijk}^A$ is the complex bulk conductivity coefficient defined by $\tilde{\sigma}_{ij}(\mathbf{q}) = \tilde{\sigma}_{ij}(0) + \tilde{\sigma}_{ijk}q_k + \dots$, and

$$\begin{aligned} \sigma_{ijk} &= i \left[\epsilon_{ikl} G_{jl} + \epsilon_{jkl} G_{il} - \frac{1}{2} \omega (a'_{ijk} + a'_{jik}) \right] = \sigma_{jik}, \\ \sigma'_{ijk} &= i \left[-\epsilon_{ikl} G'_{jl} + \epsilon_{jkl} G'_{il} + \frac{1}{2} \omega (a_{ijk} - a_{jik}) \right] = -\sigma'_{jik}. \end{aligned} \quad (\text{S35})$$

Let us assume C_{3z} and C_{2x} symmetries for simplicity. We further impose that the bulk Hall response is zero, i.e., $\chi'_{ij} = 0$, in order to focus on the magneto-electric and electric-quadrupole effects. For $\kappa = \pm \hat{z}$, the wave equation is

$$\begin{pmatrix} 1 + \epsilon_0^{-1} \chi_{xx} - n^2 & n\kappa_z \mu_0 c \sigma'_{xyz} \\ -n\kappa_z \mu_0 c \sigma'_{xyz} & 1 + \epsilon_0^{-1} \chi_{xx} - n^2 \end{pmatrix} \begin{pmatrix} E_x \\ E_y \end{pmatrix} = 0. \quad (\text{S36})$$

The refractive index satisfying the wave equation is given by

$$n_{\pm}^{\kappa_z} = \sqrt{1 + \epsilon_0^{-1} \chi_{xx} + (i\mu_0 c \sigma'_{xyz}/2)^2} \mp i\kappa_z \mu_0 c \sigma'_{xyz}/2, \quad (\text{S37})$$

for circular polarization $\hat{\pm} = \hat{x} + i\hat{y}$.

2. Reflection and transmission from a single interface

We consider the interface of medium 1 ($z > 0$) and medium 2 ($z < 0$) with the surface normal \hat{z} . For normal incidence, in the circularly polarized basis,

$$\begin{pmatrix} H_+ \\ H_- \end{pmatrix} = \frac{1}{\mu_0 c} \begin{pmatrix} -\mu_0 c \tilde{T}_{xx}^{\mu} - i n_{\mu+}^{\kappa_z} \kappa_z & 0 \\ 0 & -\mu_0 c \tilde{T}_{xx}^{\mu} + i n_{\mu-}^{\kappa_z} \kappa_z \end{pmatrix} \begin{pmatrix} E_+ \\ E_- \end{pmatrix} \quad (\text{S38})$$

within the media $\mu = 1$ or 2 , where n_{\pm} depends on the sign κ_z , and $\kappa_z = -1$ for incident and transmitted light, while $\kappa_z = 1$ for reflected light. Here,

$$\begin{aligned}\tilde{T}_{xx} &= T_{xx} - iT'_{xx} \\ &= \frac{1}{3}(G_{xx} - G_{zz}) - \frac{1}{6}\omega(a'_{yzx} - a'_{zyx}) - i \left[G'_{xx} - \frac{1}{2}\omega(a_{yzx} - a_{zyx}) \right] \\ &= \frac{i}{3}\sigma_{zxy} - \frac{1}{2}\sigma'_{xyz}.\end{aligned}\tag{S39}$$

As we consider light incident from medium 1 to medium 2, the electric field in medium 1 consists of incident and reflected fields while that in medium 2 is the transmitted field.

$$\begin{aligned}\mathbf{E}_1 &= \mathbf{E}^i + \mathbf{E}^r \equiv (1 + r)\mathbf{E}^i, \\ \mathbf{E}_2 &= \mathbf{E}^t \equiv t\mathbf{E}^i,\end{aligned}\tag{S40}$$

where

$$r = \begin{pmatrix} r_{++} & r_{+-} \\ r_{-+} & r_{--} \end{pmatrix} = \begin{pmatrix} r_{++} & 0 \\ 0 & r_{--} \end{pmatrix}, \quad t = 1 + r\tag{S41}$$

by C_{3z} symmetry and the continuity of \mathbf{E} at the interface.

The \mathbf{B} field satisfies the boundary condition as follows

$$\mathbf{B}^t = \mathbf{B}^i + \mathbf{B}^r + \mu_0 \hat{z} \times \mathbf{j}_s,\tag{S42}$$

where $\mathbf{j}_s = [(e^2/2\pi h)(\theta_2^{(z)} - \theta_1^{(z)}) + (\tilde{T}_{xx}^2 - \tilde{T}_{xx}^1)]\mathbf{E} \times \hat{z}$ is the total two-dimensional surface current density. By solving the boundary condition, we obtain

$$\begin{aligned}r_{++} &= \frac{n_{1L} - n_{2L} - i\mu_0 c \sigma_{xy}^s}{n_{1R} + n_{2L} + i\mu_0 c \sigma_{xy}^s}, \\ r_{--} &= \frac{n_{1R} - n_{2R} + i\mu_0 c \sigma_{xy}^s}{n_{1L} + n_{2R} - i\mu_0 c \sigma_{xy}^s}, \\ r_{+-} &= r_{-+} = 0,\end{aligned}\tag{S43}$$

where $n_{\mu L} = n_{\mu+}^- = n_{\mu-}^+$ is the refractive index for left circularly polarization, and $n_{\mu R} = n_{\mu-}^- = n_{\mu+}^+$ is the refractive index for the right circularly polarization, where the expression of $n_{\mu+}^{\kappa_z}$ is given by Eq. S37, and

$$\sigma_{xy}^s = (e^2/2\pi h)(\theta_2^{(z)} - \theta_1^{(z)}) + (\tilde{T}_{xx}^2 - \tilde{T}_{xx}^1)\tag{S44}$$

is the two-dimensional surface conductivity. From the expressions of r_{++} and r_{--} and Eq. (S37), we obtain the Kerr angle

$$\varphi_K = \tan^{-1} \frac{r_{xy}}{r_{xx}} = \tan^{-1} \left[\frac{-i(r_{++} - r_{--})}{r_{++} + r_{--}} \right]. \quad (\text{S45})$$

3. Cancellation and absence of Kerr in nonmagnetic systems

In a nonmagnetic system, the \mathcal{T} -symmetry dictates $G_{ij} = a'_{ijk} = T_{xx} = \theta^{(z)} = 0$, $G'_{ij}, a_{ijk}, T'_{xx} \neq 0$, Therefore, we found

$$\begin{aligned} r_{++} - r_{--} &\propto [2i\mu_0 c(T'_{xx}{}^{\mu=2} - T'_{xx}{}^{\mu=1})] - [n_{1R} - n_{1L} - (n_{2R} - n_{2L})] \\ &= [i\mu_0 c(\sigma_{xyz}^{A,\mu=2} - \sigma_{xyz}^{A,\mu=1})] - [n_{1R} - n_{1L} - (n_{2R} - n_{2L})] \\ &= 0 \end{aligned} \quad (\text{S46})$$

Again, we have $n_{\mu L} = n_{\mu+}^- = n_{\mu-}^+$ is the refractive index for left circularly polarization, and $n_{\mu R} = n_{\mu-}^- = n_{\mu+}^+$ is the refractive index for the right circularly polarization, where the expression of $n_{\mu\pm}^{\kappa_z}$ is given by $n_{\pm}^{\kappa_z} = \sqrt{1 + \epsilon_0^{-1} \chi_{xx} + (i\mu_0 c \sigma'_{xyz}/2)^2} \mp i\kappa_z \mu_0 c \sigma'_{xyz}/2$. We also have $\tilde{T}_{xx}^\mu = T'_{xx}{}^\mu = \sigma_{xyz}^{A,\mu=2}/2$ because $T_{xx}^\mu = 0$ with \mathcal{T} symmetry (Eq. S37).

We can understand this cancellation as a compensation between bulk and surface responses.

- The refractive indices part “ $n_{1R} - n_{1L} - (n_{2R} - n_{2L})$ ” are responsible for circular birefringence (the natural optical activity) in the bulk.
- $\sigma_{xyz}^{A,\mu=2} - \sigma_{xyz}^{A,\mu=1}$ is responsible for the surface current that leads to the jump of B field at the surface.

Their effects cancel such that there is no net polar Kerr rotation (i.e., no Kerr rotation at normal incidence), compatible with results from previous papers including Refs. [28–30].

4. No cancellation and nonzero Kerr in MnBi_2Te_4

By contrast, in \mathcal{PT} -symmetric AFMs, the \mathcal{PT} -symmetry and the \mathcal{T} -breaking dictates $G'_{ij} = a_{ijk} = T'_{xx} = 0$, $G_{ij}, a'_{ijk}, T_{xx}, \theta^{(z)} \neq 0$. Correspondingly, we got

$$r_{xy} = \frac{1}{2i}(r_{++} - r_{--}) = -\frac{2n_1\mu_0 c[\frac{e^2}{2\pi\hbar}(\theta_2^{(z)} - \theta_1^{(z)}) + (\tilde{T}_{xx}^2 - \tilde{T}_{xx}^1)]}{(\mu_0 c[\frac{e^2}{2\pi\hbar}(\theta_2^{(z)} - \theta_1^{(z)}) + (\tilde{T}_{xx}^2 - \tilde{T}_{xx}^1)])^2 + (n_1 + n_2)^2}. \quad (\text{S47})$$

Here, we see that the Kerr rotation has two origins: $(\tilde{T}_{xx}^2 - \tilde{T}_{xx}^1)$ is the gyrotropic birefringence (which has been known previous) and $(\theta_2^{(z)} - \theta_1^{(z)})$ is the Axion contribution (our new results).

- In MnBi_2Te_4 , $\tilde{T}_{xx}^2 - \tilde{T}_{xx}^1 = 0$ because the bulk MnBi_2Te_4 respects inversion symmetry. So the dominant contribution is the optical Axion electrodynamics.
- In Cr_2O_3 , both contributions exist.

In any case, there is no cancellation hence the Kerr rotation is always nonzero in \mathcal{PT} -symmetric AFM including even-layered MnBi_2Te_4 .

V. Additional discussion

V.1. Additional discussion about Berry curvature real space dipole

In the main text, we noted that the $\alpha_{xx}^{\text{Berry}}(\omega)$ can be understood as the Berry curvature real space dipole. We provide some additional discussion about this point.

V.1.1. Berry curvature real space dipole is dictated by \mathcal{PT} symmetry

\mathcal{PT} maps real space location z to $-z$; \mathcal{PT} also flips Ω to $-\Omega$. Therefore, we have the following relationship

$$\Omega(z) \stackrel{\mathcal{PT}}{=} -\Omega(-z), \quad (\text{S48})$$

which means that the Berry curvature Ω at location z is always opposite to that at $-z$. Therefore, \mathcal{PT} dictates (1) the total Berry curvature summed up all over the space identically vanishes but (2) there is a real space dipole of Berry curvature.

As a side note, using the same philosophy, we can study spatially-chiral materials, where time-reversal symmetry \mathcal{T} dictates $\Omega(k) \stackrel{\mathcal{T}}{=} -\Omega(-k)$. So in noncentrosymmetric materials (1) total Berry curvature summed up all over the k space identically vanishes but (2) there is a k space dipole of Berry curvature. We can also study FMs, where space-inversion symmetry \mathcal{P} dictates $\Omega(k) \stackrel{\mathcal{P}}{=} \Omega(-k)$. So the total Berry curvature in FMs is nonzero.

V.1.2. The ME effect can be visualized by the Berry curvature real space dipole

Next, we show that the ME effect can be visualized by the Berry curvature real space dipole. Figure S49a shows the Berry curvature real space dipole. It is known that Berry curvature leads to an anomalous velocity, i.e., a deflection of electron trajectory. Because the Berry curvature at $\pm z$ is opposite, upon applying in-plane E field, electrons at $\pm z$ deflect toward opposite directions. As shown in Figure S49b, this can be visualized as an itinerant circulation, which in turn leads to a magnetization M . Therefore, because of the Berry curvature real space dipole, E can generate M , i.e., an ME effect.

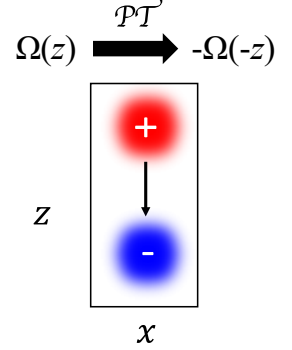


Fig. S48: \mathcal{PT} symmetry.

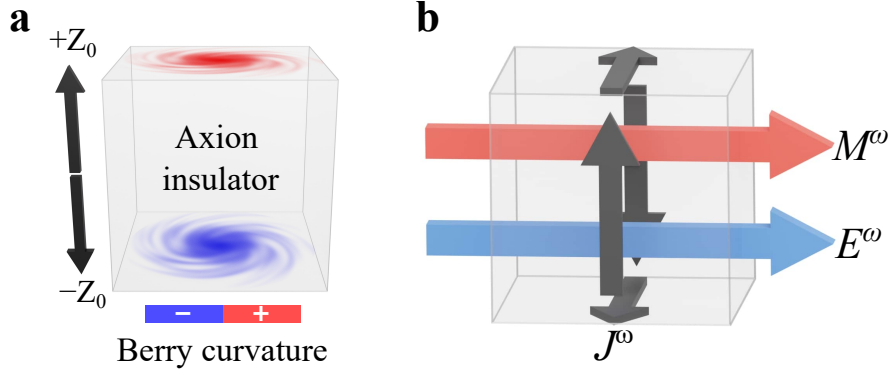


Fig. S49: The ME effect can be visualized by the Berry curvature real space dipole.

3. Mathematical derivations

As explained above, qualitatively, the ME effect is a natural consequence of the Berry curvature real space dipole. We further establish the mathematical relationship between the ME coefficient $\alpha_{xx}^{\text{Berry}}(\omega)$ and the Berry curvature real space dipole. As shown in Eq. S49, we have

$$\begin{aligned}
 \alpha_{xx}^{\text{Berry}}(\omega) &= \frac{e^2}{\hbar L} \sum_{o,u} \int d^2\mathbf{k} \frac{\varepsilon_{uo}(\mathbf{k})}{\varepsilon_{uo}(\mathbf{k}) - \hbar\omega} \text{Im} \left[\frac{\hbar^2 \langle o(\mathbf{k}) | \hat{v}^x | u(\mathbf{k}) \rangle \langle u(\mathbf{k}) | \hat{v}^y \hat{r}^z | o(\mathbf{k}) \rangle}{\varepsilon_{uo}^2(\mathbf{k})} \right] \\
 &\simeq \frac{e^2}{\hbar L} \sum_{o,u} \int d^2\mathbf{k} \frac{\varepsilon_{uo}(\mathbf{k})}{\varepsilon_{uo}(\mathbf{k}) - \hbar\omega} \langle \hat{r}^z \rangle \text{Im} \left[\frac{\hbar^2 \langle o(\mathbf{k}) | \hat{v}^x | u(\mathbf{k}) \rangle \langle u(\mathbf{k}) | \hat{v}^y | o(\mathbf{k}) \rangle}{\varepsilon_{uo}^2(\mathbf{k})} \right] \\
 &= \frac{e^2}{2\hbar L} \sum_{o,u} \int d^2\mathbf{k} \frac{\varepsilon_{uo}(\mathbf{k})}{\varepsilon_{uo}(\mathbf{k}) - \hbar\omega} \langle \hat{r}^z \rangle \Omega_{uo}, \tag{S49}
 \end{aligned}$$

where $\Omega_{uo} = 2\text{Im} \left[\frac{\hbar^2 \langle o(\mathbf{k}) | \hat{v}^x | u(\mathbf{k}) \rangle \langle u(\mathbf{k}) | \hat{v}^y | o(\mathbf{k}) \rangle}{\varepsilon_{uo}^2(\mathbf{k})} \right]$ is the inter-band Berry curvature. The key approximation in Eq. S49 is that \hat{r}^z is moved out of the inner product. We provide additional discussions/clarifications about this point. This is a good approximation when the wavefunction of the electronic states is concentrated at a particular height z (i.e., in a particular layer). To see that, we insert a complete Hilbert space into the inner product as shown in Eq. S50. When wavefunction of the electronic states is concentrated in a particular layer, then we have $\langle \mathbf{p}(\mathbf{k}) | \hat{r}^z | o(\mathbf{k}) \rangle \simeq \delta_{po} \langle \hat{r}^z \rangle$. As a result, we can move \hat{r}^z out of the inner product and Eq. S50 becomes the Berry curvature real space dipole. In the limit of decoupled layer systems, then the wavefunctions are indeed purely localized at each layers. In the presence of interlayer coupling, the wavefunction will have finite weight on multiple layers. Nevertheless, for van der Waals materials, the interlayer coupling is expected to be relatively weak. Hence, the wavefunction of the electronics states is relatively localized.

$$\begin{aligned}
\alpha_{xx}^{\text{Berry}}(\omega) &= \frac{e^2}{\hbar L} \sum_{\text{o,u}} \int d^2\mathbf{k} \frac{\varepsilon_{\text{uo}}(\mathbf{k})}{\varepsilon_{\text{uo}}(\mathbf{k}) - \hbar\omega} \text{Im} \left[\frac{\hbar^2 \langle \text{o}(\mathbf{k}) | \hat{v}^x | \text{u}(\mathbf{k}) \rangle \langle \text{u}(\mathbf{k}) | \hat{v}^y \hat{r}^z | \text{o}(\mathbf{k}) \rangle}{\varepsilon_{\text{uo}}^2(\mathbf{k})} \right] \\
&= \frac{e^2}{\hbar L} \sum_{\text{o,u}} \int d^2\mathbf{k} \frac{\varepsilon_{\text{uo}}(\mathbf{k})}{\varepsilon_{\text{uo}}(\mathbf{k}) - \hbar\omega} \text{Im} \left[\frac{\hbar^2 \langle \text{o}(\mathbf{k}) | \hat{v}^x | \text{u}(\mathbf{k}) \rangle \sum_{\text{p}} \langle \text{u}(\mathbf{k}) | \hat{v}^y | \text{p}(\mathbf{k}) \rangle \langle \text{p}(\mathbf{k}) | \hat{r}^z | \text{o}(\mathbf{k}) \rangle}{\varepsilon_{\text{uo}}^2(\mathbf{k})} \right] \\
&\simeq \frac{e^2}{\hbar L} \sum_{\text{o,u}} \int d^2\mathbf{k} \frac{\varepsilon_{\text{uo}}(\mathbf{k})}{\varepsilon_{\text{uo}}(\mathbf{k}) - \hbar\omega} \langle \hat{r}^z \rangle \text{Im} \left[\frac{\hbar^2 \langle \text{o}(\mathbf{k}) | \hat{v}^x | \text{u}(\mathbf{k}) \rangle \sum_{\text{p}} \langle \text{u}(\mathbf{k}) | \hat{v}^y | \text{p}(\mathbf{k}) \rangle \delta_{\text{po}}}{\varepsilon_{\text{uo}}^2(\mathbf{k})} \right] \\
&= \frac{e^2}{\hbar L} \sum_{\text{o,u}} \int d^2\mathbf{k} \frac{\varepsilon_{\text{uo}}(\mathbf{k})}{\varepsilon_{\text{uo}}(\mathbf{k}) - \hbar\omega} \langle \hat{r}^z \rangle \text{Im} \left[\frac{\hbar^2 \langle \text{o}(\mathbf{k}) | \hat{v}^x | \text{u}(\mathbf{k}) \rangle \langle \text{u}(\mathbf{k}) | \hat{v}^y | \text{o}(\mathbf{k}) \rangle}{\varepsilon_{\text{uo}}^2(\mathbf{k})} \right] \\
&= \frac{e^2}{2\hbar L} \sum_{\text{o,u}} \int d^2\mathbf{k} \frac{\varepsilon_{\text{uo}}(\mathbf{k})}{\varepsilon_{\text{uo}}(\mathbf{k}) - \hbar\omega} \langle \hat{r}^z \rangle \Omega_{\text{uo}} \tag{S50}
\end{aligned}$$

V.2. Additional discussion about optical control of AFM

In this section, we briefly discuss previous pioneering works on optical control of AFM [31–39], which are of great interest especially given the difficulty of this task. This discussion also justifies that helicity-dependent optical control of fully-compensated AFM order has not been achieved before. Especially, we discuss three representative works:

1. **Optical control through electric polarization P in TbMnO_3 :** In the multiferroic TbMnO_3 , the AFM order L is connected to P . Therefore, by reversing P , one can reverse L . In Ref. [31], a single P domain was first prepared by electric-field in a TbMnO_3 sample; a small area was optically heated above T_c ; when the laser was turned off, the small area went to opposite P (because of the stray electric field exerted by the surrounding single P domain [40]) and therefore the opposite L . In this way, AFM order is controlled by controlling P . The optical induced thermal effect is the driving force for the order parameter reversal.

2. **Optical control by B field and linear dichroism in MnF_2 :** Upon applying B field, MnF_2 shows a linear dichroism (LD) [32] (different absorption when light polarization is along $[110]$ and $[\bar{1}10]$). Moreover, the sign of LD is opposite for the opposite AFM states. Therefore, by applying $B = 0.5$ T, Ref. [38] achieved control of AFM order using linearly polarized light.

3. **Optical control of ferrimagnet:** Ferrimagnet has M and L that are connected. M can directly couple to circularly-polarized light like in a ferromagnet. Therefore, by reversing M , one also reverses L , as demonstrated by Ref. [37].

V.3. Additional discussion about previous theoretical works on MnBi_2Te_4

Previous theoretical works have comprehensively studied the electronic, magnetic and topological properties of MnBi_2Te_4 bulk and thin films. Here we have made a table to summarize their important pioneering findings:

	Magnetization	Topological phase	Topological phase at high B field
MnBi_2Te_4 monolayer	$M \neq 0$	Trivial insulator[41]	Trivial insulator[41]
MnBi_2Te_4 even layer	$M = 0$	Axion insulator[41–43]	Chern insulator[41]
MnBi_2Te_4 odd layer	$M \neq 0$	QAH insulator[41, 42]	Chern insulator[41]
MnBi_2Te_4 bulk*	$M = 0$	AFM TI [15, 42, 44]	Weyl semi-metal[42, 44]

*In addition, the ‘Möbius insulator’ phase is also reported in the canted AFM phase of MnBi_2Te_4 bulk[45].

V.4. Additional general discussion about thickness dependence

The Axion CD, induction and the underlying optical Axion ME coupling can persist in the thick sample limit (which is indeed what we observed in Fig. S13). Below, we explain how we can understand the physics in the thick limit, focusing on two aspects: (1) symmetry constraints and (2) finite optical penetration depth. Because the Axion CD and induction arises from the Axion optical ME coupling (Fig. R13). We will focus on understanding the Axion optical ME coupling in thick samples.

(1) Symmetry: Bulk MnBi_2Te_4 restores the space inversion symmetry \mathcal{P} and the time-reversal symmetry \mathcal{T} (precisely \mathcal{T} multiples a fractional lattice translation). This leads to a problem: symmetry dictates the ME coupling to vanish under \mathcal{P} or \mathcal{T} , so it seems that bulk should not support an Axion ME coupling. The key is to differentiate a periodic sample with no surface and a finite thick sample.

For a finite thick sample: \mathcal{P} and \mathcal{T} symmetries are still broken in the macroscopic sense. As shown in Fig. S50a, the interior of a thick sample respects \mathcal{P} and \mathcal{T} . But the surfaces strongly

break \mathcal{P} and \mathcal{T} . This is crucial because the Axion ME coupling manifests as a surface response (surface itinerant current perpendicular to the applied E field). Therefore, even though the interior respects \mathcal{P} and \mathcal{T} , a thick sample still hosts Axion ME coupling.

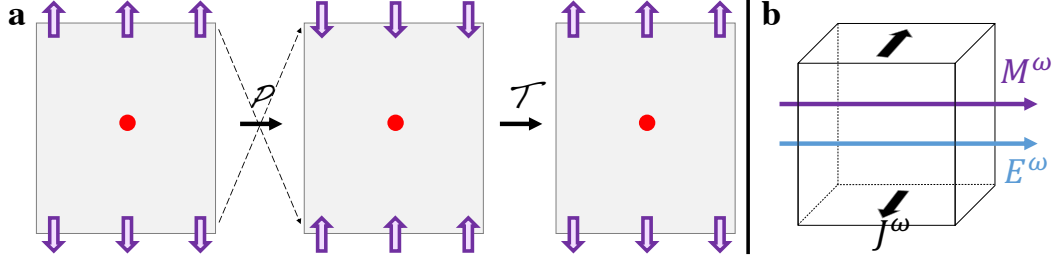


Fig. S50: a, A finite even-layered thick sample (no matter how thick) breaks \mathcal{P} and \mathcal{T} macroscopically due to the opposite magnetization at the surface. The red circle denote the macroscopic inversion center. **b**, The Axion ME coupling manifests as surface itinerant current $J^\omega \perp E^\omega$.

For a periodic system: both \mathcal{P} and \mathcal{T} symmetries are preserved. It has no surfaces, therefore the Axion ME coupling cannot be defined.

(2) Light penetration depth: We now try to understand how the light penetration depth influences the Axion optical ME coupling (and hence the Axion CD). The Axion optical ME coupling can be visualized by the surface Hall currents: As shown in Fig. S50b, light electric field E^ω leads to a Hall current J^ω at the surface. Because the top and bottom surfaces have opposite Berry curvature, they have opposite J^ω (Fig. S50b). Globally, we can visualize the J^ω at the surfaces as a circulating current, which naturally leads to an M^ω .

In a thin flake, light penetrates the sample, so the top and bottom surfaces have similarly large E^ω and hence similarly large J^ω , which leads to an M^ω as explained above.

In a thick sample, light strongly decays. So only the top surface has a large E^ω and hence a large J^ω . Nevertheless, this still leads to a nonzero M^ω .

-
- [1] Xu, B. *et al.* Infrared study of the multiband low-energy excitations of the topological antiferromagnet MnBi_2Te_4 . *Phys. Rev. B* **103**, L121103 (2021).
- [2] Dzyaloshinskii, I. & Papamichail, E. Nonreciprocal optical rotation in antiferromagnets. *Phys. Rev. Lett.* **75**, 3004 (1995).
- [3] Landau, L. D. *et al.* *Electrodynamics of continuous media*, vol. 8 (elsevier, 2013).
- [4] Ahn, J., Xu, S.-Y. & Vishwanath, A. Theory of optical axion electrodynamics. Preprint at <https://arxiv.org/abs/2205.06843> (2022).
- [5] Krichevtsov, B., Pavlov, V., Pisarev, R. & Gridnev, V. Spontaneous non-reciprocal reflection of light from antiferromagnetic Cr_2O_3 . *J. Phys. Condens. Matter* **5**, 8233–8244 (1993).
- [6] Halperin, B. *The Physics and Chemistry of Oxide Superconductors*, vol. 60 (Springer Proceedings in Physics, 1992).
- [7] Fried, A. D. Relationship of time-reversal symmetry breaking to optical Kerr rotation. *Phys. Rev. B* **90**, 121112 (2014).
- [8] Armitage, N. Constraints on jones transmission matrices from time-reversal invariance and discrete spatial symmetries. *Phys. Rev. B* **90**, 035135 (2014).
- [9] Hosur, P., Kapitulnik, A., Kivelson, S., Orenstein, J. & Raghu, S. Kerr effect as evidence of gyrotropic order in the cuprates - revisited. *Phys. Rev. B* **91**, 039908 (2015).
- [10] Lee, S.-Y., Jeong, T.-Y., Jung, S. & Yee, K.-J. Refractive index dispersion of hexagonal boron nitride in the visible and near-infrared. *Phys. Status Solidi B* **256**, 1800417 (2019).
- [11] Zaitsev, A. M. *Optical properties of diamond: a data handbook* (Springer Science & Business Media, 2013).
- [12] Huang, B. *et al.* Layer-dependent ferromagnetism in a van der Waals crystal down to the monolayer limit. *Nature* **546**, 270–273 (2017).
- [13] Gong, C. *et al.* Discovery of intrinsic ferromagnetism in two-dimensional van der Waals crystals. *Nature* **546**, 265–269 (2017).
- [14] Burch, K. S., Mandrus, D. & Park, J.-G. Magnetism in two-dimensional van der Waals materials. *Nature* **563**, 47–52 (2018).
- [15] Otrokov, M. M. *et al.* Prediction and observation of an antiferromagnetic topological insulator. *Nature* **576**, 416–422 (2019).
- [16] Deng, Y. *et al.* Quantum anomalous Hall effect in intrinsic magnetic topological insulator MnBi_2Te_4 .

- Science* **367**, 895–900 (2020).
- [17] Liu, C. *et al.* Robust axion insulator and Chern insulator phases in a two-dimensional antiferromagnetic topological insulator. *Nature Mater.* **19**, 522–527 (2020).
- [18] Ge, J. *et al.* High-Chern-number and high-temperature quantum Hall effect without Landau levels. *Natl. Sci. Rev.* **7**, 1280–1287 (2020).
- [19] Liu, C. *et al.* Helical Chern insulator phase with broken time-reversal symmetry in MnBi_2Te_4 . *Nature Commun.* **12**, 4647 (2021).
- [20] Deng, H. *et al.* High-temperature quantum anomalous hall regime in a $\text{MnBi}_2\text{Te}_4/\text{Bi}_2\text{Te}_3$ superlattice. *Nature Phys.* **17**, 36–42 (2021).
- [21] Yang, S. *et al.* Odd-even layer-number effect and layer-dependent magnetic phase diagrams in MnBi_2Te_4 . *Phys. Rev. X* **11**, 011003 (2021).
- [22] Ovchinnikov, D. *et al.* Intertwined topological and magnetic orders in atomically thin Chern insulator MnBi_2Te_4 . *Nano Lett.* **21**, 2544–2550 (2021).
- [23] Gao, A. *et al.* Layer Hall effect in a 2d topological axion antiferromagnet. *Nature* **595**, 521–525 (2021).
- [24] Cai, J. *et al.* Electric control of a canted-antiferromagnetic chern insulator. *Nature Commun.* **13**, Article number: 1668 (2022).
- [25] Li, Y. *et al.* Nonlocal transport and one-dimensional conduction in the Axion insulator state of MnBi_2Te_4 . Preprint at <https://arxiv.org/abs/2105.10390> (2021).
- [26] Tai, L. *et al.* Distinguishing two-component anomalous Hall effect from topological Hall effect in magnetic topological insulator MnBi_2Te_4 . Preprint at <https://arxiv.org/abs/2103.09878> (2021).
- [27] Raab, R. E. & De Lange, O. L. *Multipole theory in electromagnetism: classical, quantum, and symmetry aspects, with applications*, vol. 128 (Oxford University Press, Oxford, 2004).
- [28] Agranovich, V. & Yudson, V. On phenomenological electrodynamics of gyrotropic media. *Opt. Commun.* **9**, 58–60 (1973).
- [29] Halperin, B. I. *The Physics and Chemistry of Oxide Superconductors* (Springer Berlin Heidelberg, 1992), 60 edn.
- [30] Hosur, P. *et al.* Kerr effect as evidence of gyrotropic order in the cuprates - revisited. *Phys. Rev. B* **91**, 039908 (2015).
- [31] Manz, S. *et al.* Reversible optical switching of antiferromagnetism in TbMnO_3 . *Nature Photon.* **10**, 653–656 (2016).
- [32] Kharchenko, O., Miloslavskaya, O. & Milner, A. Odd magnetic dichroism of linearly polarized light

- in the antiferromagnetic MnF_2 . *Low temp. Phys.* **31**, 825–830 (2005).
- [33] Liou, Y.-D. *et al.* Deterministic optical control of room temperature multiferroicity in BiFeO_3 thin films. *Nature Mater.* **18**, 580–587 (2019).
- [34] Kašpar, Z. *et al.* Quenching of an antiferromagnet into high resistivity states using electrical or ultrashort optical pulses. *Nature Electron.* **4**, 30–37 (2021).
- [35] Kimel, A. *et al.* Inertia-driven spin switching in antiferromagnets. *Nature Phys.* **5**, 727–731 (2009).
- [36] Reichlova, H. *et al.* Imaging and writing magnetic domains in the non-collinear antiferromagnet Mn_3Sn . *Nature Commun.* **10**, Article number: 5459 (2019).
- [37] Ostler, T. *et al.* Ultrafast heating as a sufficient stimulus for magnetization reversal in a ferrimagnet. *Nature Commun.* **3**, Article number: 666 (2012).
- [38] Higuchi, T. & Kuwata-Gonokami, M. Control of antiferromagnetic domain distribution via polarization-dependent optical annealing. *Nature Commun.* **7**, Article number: 10720 (2016).
- [39] Dannegger, T. *et al.* Ultrafast coherent all-optical switching of an antiferromagnet with the inverse Faraday effect. *Phys. Rev. B* **104**, L060413 (2021).
- [40] Hadni, A. & Thomas, R. Localized irreversible thermal switching in ferroelectric TGS by an argon laser. *Ferroelectrics* **6**, 241–245 (1973).
- [41] Otrokov, M. M. *et al.* Unique thickness-dependent properties of the van der waals interlayer antiferromagnet MnBi_2Te_4 films. *Phys. Rev. Lett.* **122**, 107202 (2019).
- [42] Li, J. *et al.* Intrinsic magnetic topological insulators in van der Waals layered MnBi_2Te_4 -family materials. *Science Advances* **5**, eaaw5685 (2019).
- [43] Liu, Z. & Wang, J. Anisotropic topological magnetoelectric effect in axion insulators. *Phys. Rev. B* **101**, 205130 (2020).
- [44] Zhang, D. *et al.* Topological axion states in the magnetic insulator MnBi_2Te_4 with the quantized magnetoelectric effect. *Phys. Rev. Lett.* **122**, 206401 (2019).
- [45] Zhang, R.-X., Wu, F. & Das Sarma, S. Möbius insulator and higher-order topology in $\text{MnBi}_{2n}\text{Te}_{3n+1}$. *Phys. Rev. Lett.* **124**, 136407 (2020).